8-20-2021

Effects of Structure, Crystallographic Orientation, and Dimensionality on Emergent Properties of Transition Metal Oxide Thin Films

Prahald Siwakoti

EFFECTS OF STRUCTURE, CRYSTALLOGRAPHIC ORIENTATION, AND DIMENSIONALITY ON EMERGENT PROPERTIES OF TRANSITION METAL OXIDE THIN FILMS

A Dissertation

Submitted to the Graduate Faculty of the
Louisiana State University and
Agricultural and Mechanical College
in partial fulfillment of the
requirements for the degree of
Doctor of Philosophy

in

The Department of Physics and Astronomy

by
Prahald Siwakoti
B.Sc., Tribhuvan University, 2009
M.Sc., Tribhuvan University, 2014
December 2021

This thesis is dedicated to My Parents.

Acknowledgments

During my time as a Ph.D. Student at LSU, I had an opportunity to work with and learn from some very supportive, helpful and caring individuals. Having so many mentors and friends have made this part of my journey very enjoyable and I will cherish their memories for the rest of my life.

First and foremost, I would like to express my deepest gratitude to my advisor, Professor Jiandi Zhang for his mentorship, encouragement and support throughout the work of this thesis. His helpful insights and immense knowledge have greatly benefited this work.

I would also like to express my sincere gratitude towards Professor Rongying Jin for sharing the lab and for all the extremely helpful suggestions throughout this work. I would also like to offer special thanks to my former committee member, Professor E Ward Plummer, who, although no longer with us, continues to inspire us all.

I would also like to thank my committee members, Professor Juana Moreno and Professor David Young. Their constructive criticism and helpful suggestions helped shape this work. I would also like to acknowledge Dr. Justin R. Ragains for serving as Dean's representative in my dissertation committee.

I would like to give special thanks to Dr. Mohammad Saghayezhian for being a mentor and a friend. He has been a source of constant support and inspiration to me.
I must thank Dr. Zhen Wang for all the help with transmission electron microscopy experiments. This work would not have been possible without her help. I would also like to acknowledge Dr. Hangwen Guo, Dr. Gaomin Wang for all the help especially during my early days in the lab.

My lab mates, David Howe, Zeeshan Ali, Michael Wu, Mojgan Dehghani deserve special appreciation. I want to thank them for creating a positive and pleasant environment in and around the lab. I have been privileged to have the company of so many friends, outside the lab, during this time. I would like to acknowledge Roshan Nepal, Ramakanta Chapai, Chetan Dhital, Tej Poudel Chhetri, Suman Shrestha, Yifan Yang, Joel Taylor, Scott Mullen, Michael Wu, Smita Speer, Joanna Blawat and many more. I will forever cherish their memories.

Finally, my utmost gratitude to my family for all their love and support. My father, Kamal Prasad Siwakoti my mother, Kalpana Siwakoti have been the rock of my life. I cannot thank them enough for all the troubles they went through for the sake of my education. Last but not the least, my lovely wife Shraddha Sharma. Her endless love, support and encouragement have helped me during these tough times. This work would not have been possible without their help. Therefore, this document is dedicated to them.

Table of Contents

List of Figures

Abstract

$SrRuO_3$ is the only example of ferromagnetic perovskite oxide of a 4d transition metal, wherein the electron - electron correlation is still relevant while the heavier 4d ion (Ru) gives it a larger spin-orbit coupling strength which makes it an interesting material to study.

In this thesis, we present our investigation of the structure and properties of $SrRuO_3$ thin films of varying thickness grown on [001] and [111] crystallographic orientation of the $SrTiO_3$ substrate. For $SrRuO_3$(001), we present microscopically the presence of 90° in-plane rotated structural domains that are identified by the difference in octahedral rotations and tilts pattern. Our study of the structure in ultrathin $SrRuO_3$(001) films show evidence of orthorhombic distortions down to a single unit-cell thickness. In thicker films, orthorhombic relaxation happens in 3-4 layers after which bulk-like structure is stabilized. We have found that unlike the interfaces with $CaRuO_3$ or $La_{2/3}Sr_{1/3}MnO_3$, the TiO_6 octahedra of the $SrTiO_3$ substrate at the interface is undistorted when interfaced with $SrRuO_3$.

Our study of $SrRuO_3$(111) films show a deviation of the low temperature magnetization from the conventional Bloch law, an indication of suppressed spin-wave excitations. Instead a $\sim T^2$ suppression of magnetization corresponding to Stoner excitations is observed suggesting a strong orientation dependence of magnetism. An enhancement in the transition temperature T_C and lower residual resistivity is also observed as compared to the $SrRuO_3$(001) films. Thickness dependent investigation reveal a gradual decay of T_C with thickness in $SrRuO_3$(111) as compared to a rather abrupt loss of ferromagnetism in $SrRuO_3$(001).

We show the feasibility of layered Ruddlesden - Popper (RP) type materials to be used as a substrate for high quality thin film growth. We show the variation of symmetry perpendicular to the cleaving plane in the stacking of these materials can be exploited to induce systematic 2D defects (anti-phase boundaries (APB)) that runs somewhat perpendicular to the film surface. We observe that these APBs can merge when two steps are in close proximity. The ability to create a controllable distribution of 2D defects paves way for future studies to explore new physical phenomena and applications.

Chapter 1. Introduction

In this chapter, we will start with a general introduction to the transition metal oxide (TMO) perovskites. We will discuss the various methods of manipulation of properties of these TMOs when grown as thin films on a compatible substrate. The possibility of misfit strain, octahedral symmetry mismatch, broken symmetry at the interface, crystal orientation, defects etc. as tuning knobs to manipulate properties in TMO perovskites are discussed along with some representative examples. We will also introduce the structure and properties of our choice of material, $SrRuO_3$, in its bulk and thin film form. We will also briefly discuss the thickness dependent properties of ultrathin $SrRuO_3$ films in the [001] direction of $SrTiO_3$ substrate.

1.1. Background : Transition Metal Oxides Perovskites

Perovskite oxides consists of octahedra of anions with cations embedded between them. The ideal ABO_3 perovskite structure is simple cubic and belongs to Pm3m Space Group and is shown in Figure 1.1(a). The A cation, a rare earth, alkali or alkaline earth ion, is in the cavity formed by the O anions of the eight BO_6 octahedra. The B-cation, a transition metal ion, sits at the center of the oxygen octahedra. In the presence of a cubic crystal field, the five d – orbitals of the transition metal ion, which are degenerate in spherical potential, are split into two higher energy e_g ($d_{3z^2-r^2}$, $d_{x^2-y^2}$) orbitals and three lower energy t_{2g} (d_{xy}, t_{zx}, d_{yz}) orbitals as shown schematically in Fig. 1.1(b). The e_g orbitals extend towards the oxygen ions which have a negative charge so that a d – electron in these orbitals has its energy raised by the Coulomb interaction. On the other hand, the t_{2g} orbitals point away from the oxygen ions so that an electron in these orbitals have an

energy which is less affected by these Coulomb interactions. This is shown schematically in Fig. 1.1 (c) and (d). The value of this energy $t_{2g} - e_g$ splitting is about 2 - 3 eV in typical oxides with perovskite structure. However, very few materials adopt the ideal cubic structure, and, in most cases, materials exhibit structural distortions that lower the symmetry from cubic. Manipulation through strain, symmetry, structure distortion, chemical doping, and spin-orbit coupling can further modify these d-bands. In addition, the coupling of these d-bands with the oxygen p-bands, allow freedom to tinker with electron spin-ordering, orbital configuration, and charge-transfer between atoms and interfaces.

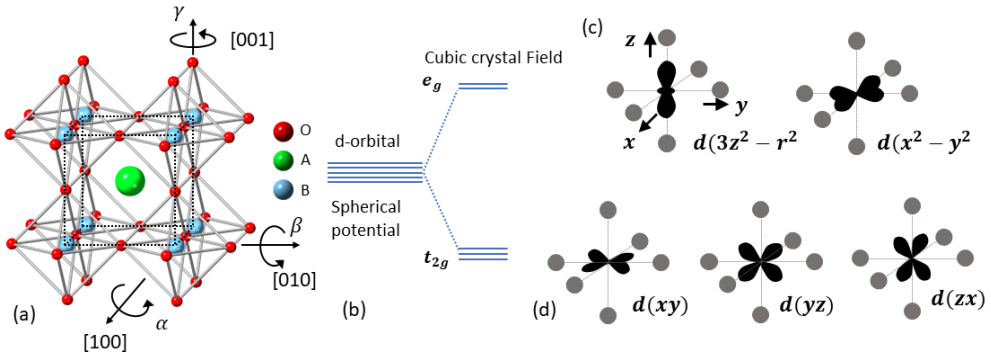

Figure 1.1. a) Crystal structure of a cubic ABO_3 perovskite unit cell. Octahedral rotations about the three orthogonal axes that intersect at the B-site atom center can be used to obtain an arbitrary system of tilt. b) d - orbitals in spherical symmetry splits in the cubic symmetry. The degenerate (c) e_g orbitals as well as (d) three t_{2g} orbitals are shown. The dark circles represent the position of O - ions.

The most common form of symmetry reduction from cubic structure happens through "rotation" or "tilt" of more-or-less rigid octahedra around one or more high symmetry axes. They are described using Glazer notation[1, 2]. As shown in Fig. 1.1(a), octahedral distortions in a perovskite can be described as rotations about the pseudo-cubic [100], [010] and [001], denoted by α, β, and γ respectively. The [100] axis is denoted as axis "a" and [010] is "b" and [001] is "c". The relative magnitude of the tilt is de-

noted by letters a, b, and c. For example, aab means equal rotations about the [100] and [010] axes and a different rotation about the [001]. A superscript is added to each axis, to indicate whether neighboring octahedra rotate in-phase (+) or out-of-phase (-) or if there is no rotation a superscript (0) is used. The octahedral rotations effectively double the pseudo-cubic unit cell, producing a distinct set of half order Bragg diffraction peak depending on the system of tilt. Fig. 1.2 shows a simple example of $a^0a^0c^+$ and $a^0a^0c^-$ tilt system. Because of the rotation around the [001], the lattice parameter along a and b axes increase to $\sqrt{2}$ a_c in both the examples whereas, the unit cell along the c-direction doubles for the tilt system. Allowing for all the possible tilts and rotations of the ABO_3 perovskites, a total of 23 tilt systems can be obtained[1].

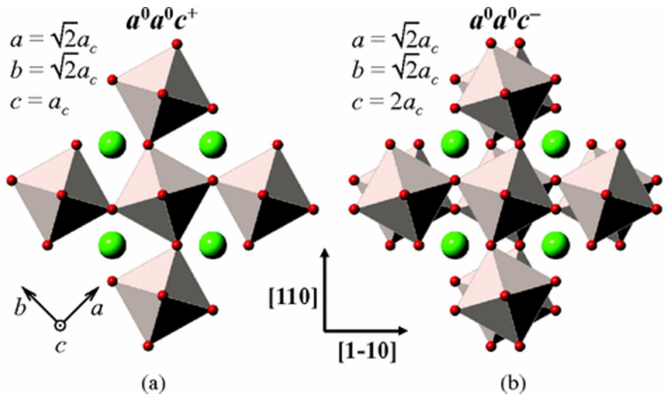

Figure 1.2. a) Schematics of (a) $a^0a^0c^+$ and (b) $a^0a^0c^-$ system of tilt in a perovskite lattice. The c-axis is doubled along the c-direction. The lattice system is tetragonal. Figure taken from [3].

1.2. Epitaxial Thin Film: Tuning Opportunities

Epitaxial thin film growth of perovskite oxides has been very successful in manipulating the properties of the bulk system [4, 5, 6, 7] and in some cases obtaining novel physical properties otherwise non-existent in the bulk [8, 9, 10]. These thin films are usu-

ally grown on appropriate crystal substrates. The lattice mismatch between the substrate and the film creates a strain on the film. The strain relaxation happens through expansion and contraction of the lattice parameter in the perpendicular direction. Thus the strain is an excellent tuning parameter to manipulate properties in the thin film systems. Besides strain, there are quite a few tools at our disposal. Below, we will discuss some of those tools that are of importance to our work.

1.2.1. Symmetry Mismatch

In addition to the usual degree of freedom, such as lattice parameters, the octahedral tilts and rotations are also considered an important degree of freedom. The oxygen octahedral symmetry mismatch at the interface, when two systems with robustly different oxygen octahedral symmetry are brought together, also needs to be accommodated in addition to the misfit strain. This accommodation can happen either through the elongation or compression of the B-O bond which will deform the octahedra, or by rotations of rigid octahedra or both. These accommodation usually happen a few layers near the interface and can significantly affect the functional properties. For example, changes in the B-O bond length affects the magnitude and symmetry of the crystal field splitting, whereas changes in the B-O-B bond angle determines the strength and sign of the magnetic superexchange interactions (in manganite for example)[11, 12]. The ferromagnetism in ruthenates have been found to be very sensitive to the Ru-O-Ru bond angle changes owing to the strong hybridization of Ru 4d and O 2p bands. Therefore, the quantification of these octahedral distortions near the interface, that can effectively change the B-O-B bond geometry, is critical in understanding the resulting novel functionalities and poses an

experimental challenge.

1.2.2. Dimensional Confinement

Besides symmetry mismatch induced changes in properties, dimensional confinement can also be achieved when a layer is inserted between materials to restrict the spatial extent of an order parameter. For instance, an insulating layer can be inserted in between metallic layers in a superlattice to confine the mobile electrons. This kind of geometric confinement can create changes in the electronic structure and the density of states at Fermi energy which will reflect on the physical properties. Two-dimensional confinement can give rise to novel magnetic properties even in the absence of charge transfer. For example, bulk rare earth nickelates exhibit an antiferromagnetic insulating ground state except for $LaNiO_3$ which is paramagnetic metal. A study of $(LaNiO_3)_n/(LaAlO_3)_n$ superlattices showed evidence of AFM state with $T_N = 50$ K for n = 2 [13].

1.2.3. Broken Symmetry at the Interfaces

The interfaces of transition metal oxides spontaneously break the inversion symmetry (I). The broken I symmetry gives rise to an electric field perpendicular to the interface and therefore creating a need to equilibrate the electron chemical potential. A usual consequence of this is the charge transfer and screening of the charges at the interface. Because the charge, spin and orbital degrees of freedom are strongly correlated in TMOs, modulation of charge density often leads to spin and/or orbital polarization. Several other order parameters such as magnetic orderings of various kinds, superconductivity, collective phonon modes, etc. dominate the physics of TM oxides. These ordered states decay smoothly at the interface, thus influencing the materials in proximity. $LaAlO_3/SrTiO_3$ in-

terface is an excellent example to illustrate the symmetry breaking induced ordered states such as 2D electron gas [14], Ferromagnetism [15], Superconductivity [16], and the Rashba effect [17].

1.2.4. (001) vs (111)-oriented Interfaces

Crystallographic orientation of growth is another tuning parameter that is shown to have major consequences to the functional properties of thin films, especially in the ultra-thin regime. Thin film TMO perovskites are routinely grown along the [001] direction of the pseudo-cubic substrate. Epitaxy along uncommon crystallographic directions, such as [110] and [111] directions, is another avenue that shows promise for the near future of oxide interfaces [18]. The crystallographic [111] direction is especially interesting for several reasons. The (111) planes of ABO_3 perovskites consists of alternating planes of AO_3^{n-} and B^{n+} planes, where n = 4 for divalent A-site ion and n = 3 for trivalent A-site ion. These planes are charged alternatively and create an unfavorable situation even for a band insulator like $SrTiO_3$, with ± 4e charged planes. Whereas along (001) – orientation, the stacking is of neutral SrO and TiO_2 planes. This is shown schematically for an ABO_3 in Fig. 1.3 (a) and (b). The charged layers pose a problem near the interfaces and surfaces, where a compensation mechanism becomes necessary in order to lower the energy of the system. Compensation happens through a variety of mechanisms: electronic and/or lattice reconstruction, intermixing, crystallographic faceting, adsorption of external species etc. [19].

Another aspect of the 111 oriented interfaces is the hexagonal (triangular) structural motif. Bilayer stacking along [111] direction creates a new type of lattice. It consists of two triangular planes of Ti site that are shifted in the vertical direction as well as

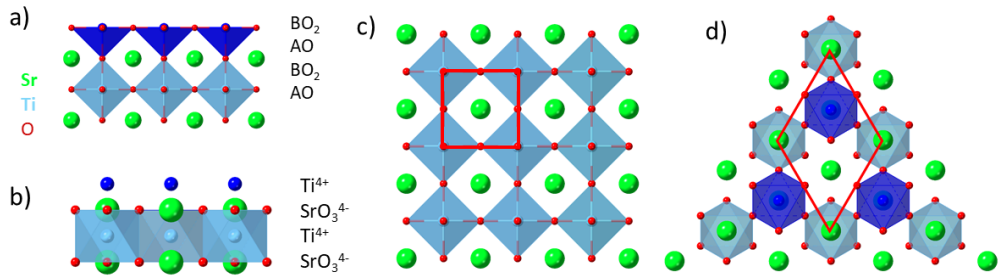

Figure 1.3. a) ABO_3 crystal structure in various crystallographic directions. a) and b) show the stacking in the [001] – orientation and [111] – orientation, respectively. c) Top view of the (001) surface. The surface unit cell is shown in red. d) Top view of a (111) bilayer showing the buckled honeycomb lattice. Different shades of BO_6 octahedra distinguish represent different planes in the vertical direction. The surface unit cell is shown in red.

horizontal direction. This structure resembles that of honeycomb structure of Graphene as shown in Fig. 1.3 (d) and is commonly referred as a buckled honeycomb lattice. The blue and cyan shade of the octahedra represents plane of atoms that are vertically shifted (along [111] – direction). Honeycomb lattices host several fascinating phenomena. Appearance of Dirac points in the band structure is one of the characteristic features. The (111) – oriented interfaces provide an excellent platform to artificially assemble the d-electron system in honeycomb structure which is theoretically predicted to give rise to non-trivial topological phases [20]. The possibility of artificially engineering topological insulators [20, 21, 22] have inspired interest in obtaining reliable growth along these directions. However, very little is known of the thermodynamics of growth on the (111) surface which poses an experimental challenge.

The epitaxial strain in the (111) – plane is considerably different from the epitaxial strain in the (001) – plane and stabilizes different octahedral rotation pattern [23]. As can be seen in Fig. 1.4, the oxygen octahedral rotation and tilt axes are neither parallel nor perpendicular to the strain plane in (111) – oriented interface while two of the three

pseudo-cubic rotation axes are lie in the strain plane for (001) – oriented interface. We can also see that the octahedral connectivity of the two B-site atoms near the interface (one above and another below the interface) is through three oxygen atom that lie at the interface as shown in Fig. 1.4 (a). On the other hand, the octahedral connectivity is through a single oxygen atom at the interface in (001) – oriented interface as shown in Fig. 1.4 (b). Therefore, misfit strain and symmetry mismatch accommodation along [111]-direction have different consequences on the stabilized film structure and properties. For example, it has been shown experimentally that (111) compression in rare earth nickelates ($RNiO_3$) can result in a polar metal [24]. A non-zero moment was measured at the (111) interface of anti-ferromagnetic $LaFeO_3$ without charge transfer [25]. It is becoming increasingly

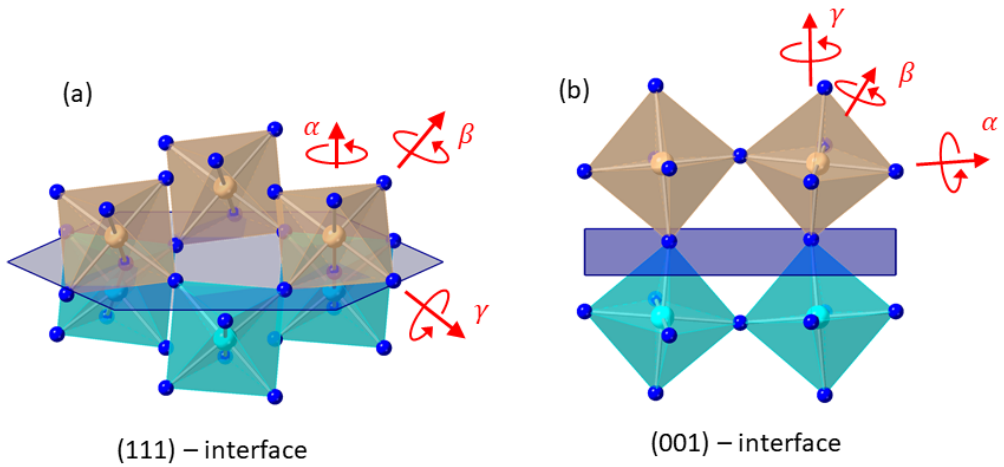

Figure 1.4. Oxygen octahedral connectivity at the interface in (a) (111) plane and (b) (001) plane. The three pseudo-cubic axes of rotations are shown.

clear that the oxygen octahedral rotation at the interface of [111]-oriented heterostructure couples differently compared to the [001] direction and thus can be exploited as a means to manipulate the local symmetry of the interface to promote functional properties [25, 26].

1.2.5. Defects in Complex Oxide thin films

Defects are disruption in the regular arrangement of the atoms in a perfect lattice. In thin film heterostructures, they can be a means of strain relaxation, such as domain walls, misfit dislocations, vacancies (point defects). Defects influence the physical properties of the thin films. They have distinctly different structure and properties and can be used as devices. For example, electronic conduction was observed at perfectly ordered 2D defects in an otherwise insulating material [27, 28, 29]. Defects in solids are classified by their dimensionality, i.e., point defects (zero dimension) and extended defects. Point defects arise because of entropy considerations and thus are unavoidable. In oxide thin films, they are usually in the form of oxygen vacancies. Extended defects often have higher dimensionality (line, surface and volumetric) and exhibit non-equilibrium characteristics [30]. One dimensional defects (line defects) in heteroepitaxial thin films, such as misfit dislocations, arise as a consequence of stress imposed through lattice mismatch and/or processing. The dislocations are caused by a termination of a plane of atoms in a crystal or equivalently by an insertion of an extra plane of atoms. The formation of misfit dislocations at the interface is a common mechanism for relieving misfit strain. Larger lattice mismatch induced strain often leads to the formation of such dislocations in thin films [31]. Various two-dimensional, surface type defects disrupt the long-range stacking sequence. Examples of surface-type defects are grain boundaries, stacking faults, and anti-phase boundaries (APBs). APBs can arise as a consequence of asymmetry in the spatial coordinates. We will discuss in Chapter 5, our method of obtaining a well-defined planar defect (APB) in a thin film heterostructure. Volume defects, such as voids, bubbles and

precipitates can also occur in a crystal and substantially affect the observed properties [30].

A schematic of the various tuning parameters, available with epitaxial thin film engineering, that can be used to manipulate thin film properties and how they disrupt the subtle balance between charge, spin, orbital and lattice to give rise to novel phases is shown in Fig. 1.5.

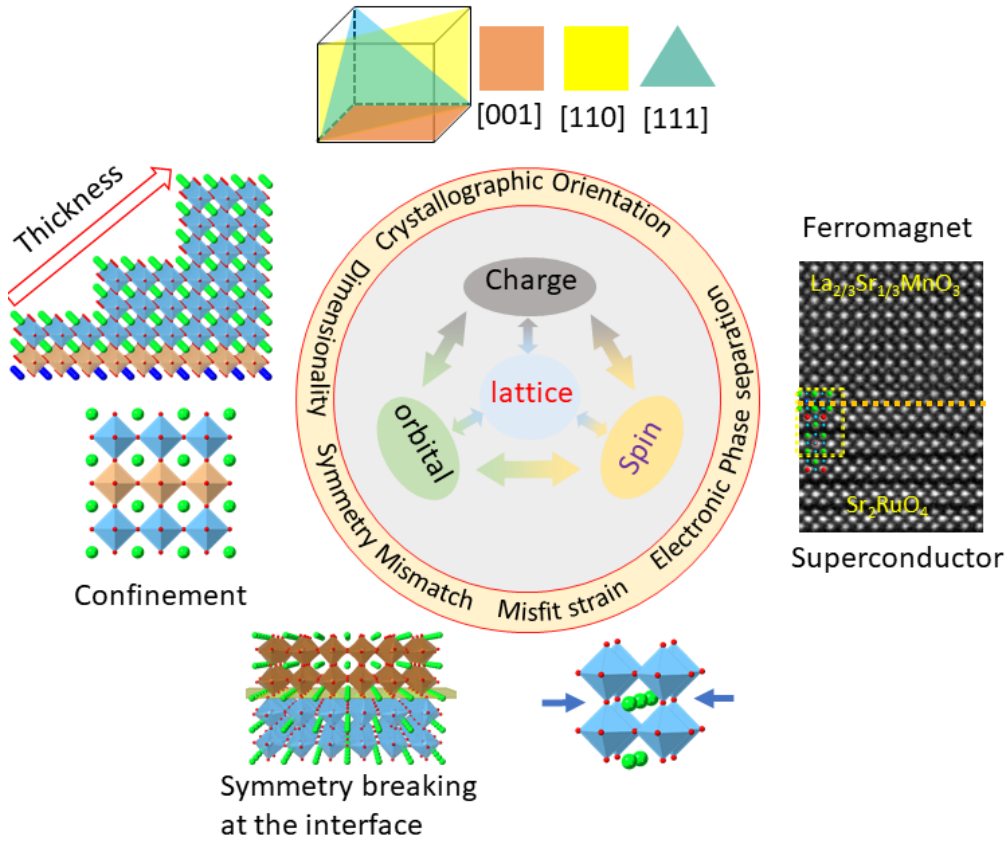

Figure 1.5. Various tuning parameters in epitaxial engineering of material properties.

1.3. $SrRuO_3$ Bulk Properties

After a general introduction of transition metal oxide perovskite, we will now introduce one interesting perovskite, $SrRuO_3$(SRO). As the n=∞ member of the Ruddlesden-Popper (RP) ruthenates $Sr_{n+1}Ru_nO_{3n+1}$, SRO has many physical properties that are

unique among perovskite oxides. SRO, at low temperatures, crystallizes in $GdFeO_3$ like orthorhombic crystal structure of the space group pbnm (No. 62). The orthorhombic lattice parameters are $a_o = 5.567$ Å, $b_o = 5.5304$ Å and $c_o = 7.8446$ Å [32]. Fig. 1.6 shows the structure of orthorhombic SRO alongside a simple cubic structure of $SrTiO_3$. In glazer notation [2], it can be described as $a^+c^-c^-$ system of rotation. To arrive at the orthorhombic SRO starting from a simple cubic structure, like $SrTiO_3$(STO), the octahedra needs to be rotated about all three pseudo-cubic orthogonal axes. Specifically, out-of-phase rotation about the [100] axis and two mutually equivalent in-phase rotations about the other two orthogonal axes would be necessary.

In simple atomic picture, low spin Ru^{4+} in $SrRuO_3$ contains 4 electrons in their d-orbitals. In the octahedral crystal field, the Ru 4d orbitals are split into groups of t_{2g} and e_g orbitals, as discussed in section 1.1. The lower three 4d (t_{2g}) orbitals are filled with four electrons according to Hund's rules. The resulting spin state is S=1. In real material, however, these d-orbitals form bands. Compared to the 3d transition metal oxides (TMO), Ru, in 4d SRO, has a somewhat more extended d orbitals and thus give rise to a moderate value of the screened electron-electron interaction and broader bands. Ru t_{2g} bands have heavier overlap with O 2p thus enhanced t_{2g}- e_g splitting is observed. Hubbard model is usually used to describe a system with correlated electrons and is written as:

$$H = -t\sum_{i,j,\sigma}(d^{\dagger}_{i,\sigma}d_{j,\sigma} + d^{\dagger}_{j,\sigma}d_{i,\sigma}) + U\sum_{i=1}^{N}(n_{i\uparrow}n_{i,\downarrow}) + \mu\sum_{i=1}^{N}(n_{i,\uparrow} + n_{i,\downarrow}) \tag{1.1}$$

where $d^{\dagger}_{i,\sigma}(d_{j,\sigma})$ is the creation (annihilation) operator of an electron at lattice site i and spin σ, n denotes the number operator. t, U and μ represents the hopping parameter, the on-site Coulombic repulsion, and the chemical potential of the system. Within

the Hubbard model, if t >> U then, the electrons in the lattice are free to move from one site to the next. In this situation, the electron conduction band has a larger bandwidth, and the system becomes metallic. On the other hand, if t << U, then there is hardly any overlap in the wavefunctions of electrons on neighboring sites. This opens a gap, called the Hubbard gap between a lower Hubbard band and the upper Hubbard band. SRO is best described by a situation where t $\sim$ U [33]. Since U is not large compared to the bandwidth ($\propto$ t), there is a significant overlap between the two Hubbard band.

SRO is the only 4d or 5d - TMO perovskite ferromagnet. In fact, it has the largest saturation moment to arise from 4d electrons. It also has a very strong magnetic anisotropy in both paramagnetic and ferromagnetic phases.

This anisotropy leads to an Ising-like magnetic phase transition and stripe domain structure with narrow domain walls [34]. SRO is a rare example of 4d itinerant ferromagnet, as evidenced by early band calculations [35, 36] and experimental observations [37], with Curie temperature T_C of 160 K. The ferromagnetism (FM) in this material is of the Stoner type, arising from a high density of states (DOS) at the Fermi level (E_F) due to a nearby van Hove singularity.

Recently reports of finite exchange splitting above T_C in angle resolved photoemission spectroscopy (ARPES) [38] and bulk sensitive optical measurements [39] have been established which points to a more local nature of magnetism in SRO. Magnetization measurements have also shown deviations from the Stoner model of ferromagnetism in the series of perovskite ruthenates, $ARuO_3$ (A = Ca, Sr, Ba) [40]. These results, along with the fact that its isoelectronic neighbor $CaRuO_3$ does not show any magnetic behavior, signifies the inadequacy of our understanding of the fundamental nature of magnetism in this

material.

The resistivity of single crystal SRO [35] and thin films [41] show a cusp in dρ/dT at the ferromagnetic Curie temperature T_C, which is usually attributed to spin disorder scattering [42]. The resistivity rises above T_C almost linearly with temperature up to 1000 K and the extracted mean free path is less than 1 nm above 500 K. This behavior is similar to the resistivity seen in high-T_c superconductors and high-T metallic phase of VO_2 and is a defining property of the so called "bad metals" or correlated electron metals. At low temperatures, the T-dependence of resistivity shows a Fermi-liquid behavior. Near the ferromagnetic transition, critical magnetic fluctuations affect the transport properties considerably.

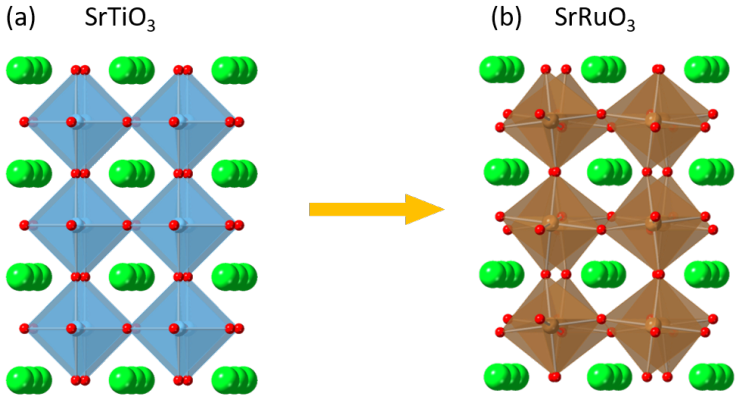

Figure 1.6. a) Simple cubic $SrTiO_3$ structure with no tilts and rotations (b) Orthorhombic $SrRuO_3$ with $a^-a^-c^+$ system of rotations.

1.4. Thin Films $SrRuO_3$

We will start with the discussion of the properties of SRO films grown on the (001) surface of $SrTiO_3$(STO) substrate. For the rest of this thesis, we will denote SRO films grown on STO(001) as SRO(001) and the SRO film grown on STO(111) surface as SRO(111). STO(001) surface exerts compressive strain of about 0.446 % on SRO

films [3]. Due to the compressive strain, SRO exhibit a distorted orthorhombic structure (monoclinic symmetry) when grown on STO(001), with its orthorhombic c axis lying in plane and [110] direction pointing out of plane as shown in Fig. 1.7 [3, 34]. Since a=b in the plane of the substrate, the pseudo-cubic c-axis will be tilted from the [001] axis by an angle $\alpha_p \neq 90°$, while the orthorhombic c-axis of SRO is strained in-plane and is 7.81 Å in length. Films with tetragonal crystal symmetry can be stabilized by growing in

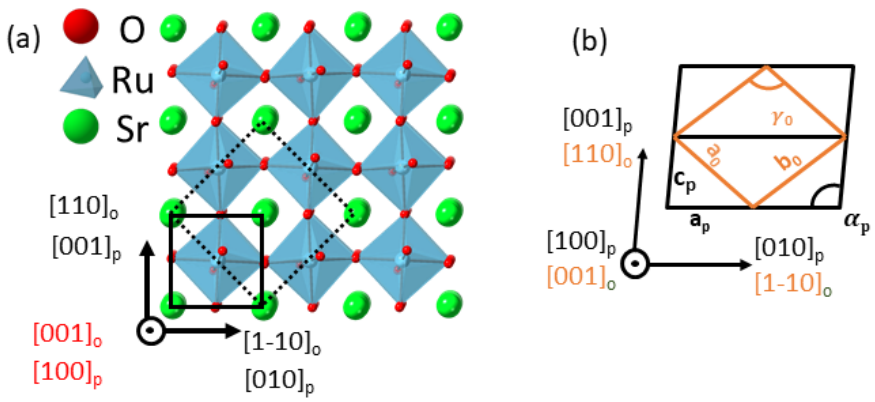

Figure 1.7. (a) A model structure of bulk $SrRuO_3$ showing the pseudo-cubic unit cell (solid square) and orthorhombic unit cell (dashed square). The pseudo-cubic axes are shown. The [100] direction in red is the direction with in-phase rotation of octahedra. b) Orthorhombic film on cubic substrate under compressive strain. Note the 110 orthorhombic axes (denoted with 'o' subscript) is tilted and shows the direction of growth. Pseudo-cubic axes are denoted with 'p' subscript. a_p and c_p are the lattice parameters of STO substrate.

oxygen deficient environment [43, 44]. In addition, the out-of-plane lattice parameter has been shown to be sensitive to Ru-deficiency [45]. These results signify the importance of stoichiometry to determine the symmetry of the lattice and the sensitivity of the structure to the growth environment. The stoichiometric films grown at optimum oxygen are orthorhombic in symmetry. Epitaxial thin films of SRO on STO(001) show a ferromagnetic transition at a lower temperature of $\approx$ 150 K [46] [$\approx$ 160 K in bulk crystals]. SRO shows strong uniaxial magnetic anisotropy because of strong spin-orbit coupling. For thin films,

the easy axis is close to the out-of-plane direction to the film plane in both SRO(001) and SRO(111).

1.5. Thickness – Dependent Properties of $SrRuO_3$(001)

The electronic and magnetic properties in the SRO ultra-thin films are in sharp contrast to the bulk properties. SRO films become non-magnetic and insulating for thickness smaller than 3 u.c. In addition to the loss of ferromagnetism, a metal insulator transition occurs around 3-4 unit-cell which almost coincides with the magnetic dead layer [47, 48, 49], though the critical thickness for the transition varies with growth conditions. It is found that the moderate U in SRO is not enough to localize carriers and induce metal-insulator transition (MIT), therefore a lot of effort has been put to investigate the influences of the extrinsic mechanisms. However, to date there is no consensus on the origin of MIT.

As the thickness is decreased, it is natural to assume the effect of disorder on the transport properties would become overwhelming. Ru vacancies are difficult to observe as they show only subtle differences in the crystallinity of the thin films [45]. PLD grown films are expected to be inherently Ru-deficient because the plasma plume contains high oxygen pressure. Disorder could also be caused by the interfacial intermixture of Ti/Ru ions. Kim *et al* studied $SrTi_{1-x}Ru_xO_3$ for ($0 \leq x \leq 1$) and found six different kinds of electronic structure based on the amount of disorder [50]. Oxygen vacancies have a ubiquitous presence in TMO films and are another source of disorder. Anderson localization due to disordered electric potentials, from these point defects, in the crystal is a possible mechanism to introduce metal-insulator transition in ultra-thin SRO films.

A kink in the dispersion curve in ARPES studies of SRO films has been observed indicative of strong electron-phonon coupling [38]. Negligible thickness dependence of the binding energy of the kink [51] suggests electron-phonon coupling might not be the driving force for MIT as suggested by Shen *et al* [52]. Such a kink is also reported in SRO(111) films, albeit the phonon mode that couples is expected to be different [53].

An insulating antiferromagnetic phase near the interface is also proposed [49, 54] to be responsible for observed MIT. The presence of disorder and/or surface/interface reconstruction is expected to stabilize this anti-ferromagnetic layer. However, there has not been subsequent support for this idea.

Another possible scenario is the confinement of orbitals due to spatial confinement. In bulk $SrRuO_3$, all the t_{2g} orbitals form 2D tight binding bands through hybridization with the O 2p orbitals. As the thickness of SRO in the 001 crystallographic direction is decreased, t_{2g} orbitals like d_{xz} and d_{yz} do not have orbitals to hop in the z-direction due to spatial confinement and therefore 1D-type singularities are induced. For d_{xy} however, the 2D type Van Hove singularity can persist down to a single monolayer. This kind of orbital selective confinement creates changes in the electronic structure causing the DOS at Fermi energy to diminish [48, 55].

1.6. Anomalous Hall Effect

In this section, we will briefly discuss the Anomalous Hall effect in general and some studies in $SrRuO_3$. Hall resistivity in magnetic materials is conventionally written as

$$\rho_{xy} = \rho_{xy}^{OHE} + \rho_{xy}^{AHE} = R_0\mathbf{B} + R_s(\rho)\mathbf{M} \tag{1.2}$$

Where, first term in equation 1.2 is the ordinary Hall effect(OHE) which is proportional to the magnetic field **B** and electron velocity **v** and originates from the Lorentz force, $F = \frac{-e}{\mu_0 c}\mathbf{v} \times \mathbf{B}$. The ordinary Hall coefficient R_0 is unique in the sense that it only depends on the electron density, thus, experimentally, measuring the ordinary Hall coefficient allows extracting the sign and magnitude of carrier density in a material. The second term in equation 1.2 is the anomalous Hall effect (AHE) and is proportional to magnetization **M**. $R_s(\rho)$ is the anomalous Hall Coefficient, which depends on the resistivity as[56]

$$R_s = a\rho_{xx} + b\rho_{xx}^2 \tag{1.3}$$

The first term, which is linear in ρ_{xx}, the longitudinal resistivity, is due to 'skew scattering' and the second term, which is quadratic in ρ_{xx}, is due to 'side jump'. Both the skew scattering and side jump mechanisms are impurity scattering mechanisms modified by spin orbit interaction. Another contribution that is independent of scattering events was proposed by Karpus and Luttinger [57]. They showed that electrons in a solid acquire an additional "anomalous velocity" contribution to their group velocity perpendicular to the applied electric field which contributes to the Hall effects. The sum of the "anomalous velocity" over all occupied bands can be non-zero for ferromagnetic conductors and therefore contributes to Hall conductivity σ_{xy}. The significance of this intrinsic contribution has recently been recognized in terms of the geometric concepts of Berry phase in momentum space [56, 58, 59]. Thus, the non-trivial geometry of the band structure can act as an "effective magnetic field". The anomalous Hall conductivity therefore depend sensitively on the details of the band structure topology.

The Hall resistivity ρ_{xy} in SRO exhibits a non-monotonic temperature dependence

including a change of sign below T_C [60]. Both the Karpus Luttinger (KL) theory and skew scattering theory were insufficient to describe this behavior. This inspired band calculations that fully incorporates the spin orbit interaction. The Berry curvature, obtained from band calculations is shown in Fig. 1.8 a). It shows sharp peak near the Γ-point and sharp features along the $\Gamma - M$ diagonal. The origin of these sharp features is said to be the (near) degeneracy and/or band crossing. Berry curvature is negligible in the rest of the momentum space. The Hall conductivity, σ_{xy}(T) obtained from Band calculations reproduced the non-monotonic magnetization dependence which agreed well with the experimental observation. However, one should keep in mind that the band structure calculations are very sensitive to the input parameters. As shown in Fig. 1.8, the temperature dependence of AHE for a hypothetical cubic structure of SRO was found to be significantly different than the orthorhombic structure in the study of Fang *et al* [61]. This underscores the importance of structural symmetry when analyzing the Hall data.

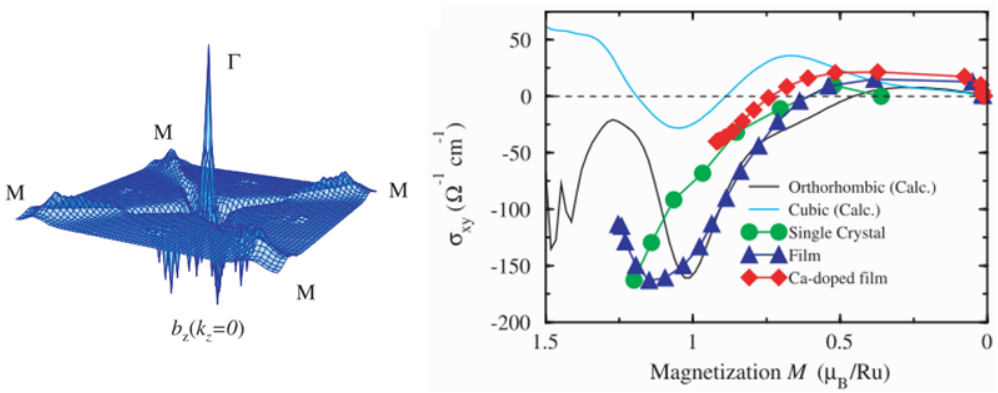

Figure 1.8. Left: The Berry curvature $b_z(k)$ as a function of $k_\perp = (k_x, k_y)$ with the fixed $k_z = 0$. Right: The calculated and experimental magnetization dependence of transverse conductivity in various crystal symmetries. Figure taken from [61].

In addition to the conventional AHE in ferromagnets, additional "hump-like" features in Hall resistivity are reported. These features are often interpreted to be due to a

chiral magnetic phase in the real space formed near the interface. In $SrRuO_3/SrIrO_3$ bilayer on $SrTiO_3(001)$ substrate the "atypical humps" were attributed to the Skyrmion phase driven by the interface Dzyaloshinskii-Moriya (DM) interaction as a consequence of broken inversion symmetry and strong spin-orbit interaction of $SrIrO_3$ [62]. In $SrRuO_3$ film interfaced with ferroelectric $BaTiO_3$ [63], the off-centering Ru site distortions due to the proximity to the BTO lattice is said to have given rise to an emergent DM interaction to stabilize magnetic Skyrmions. However, these "atypical humps" in hall resistivity were observed in single layer SRO film where interfacing with 5d elements or the ferroelectric layer did not seem critical, since Ru already has a sizeable SOI [64, 65]. An alternative interpretation of these atypical humps has been put forward that argues the multiple channels of anomalous Hall effect can give rise to the humps in the resultant Hall resistivity. The electronic conduction band in SRO are strongly responsive to external perturbations and on temperature. The Berry curvature of these topologically non-trivial bands determine the intrinsic contribution to Hall resistivity. Therefore changes to the band topology caused by inhomogeneity due to domains [66], defects such as Ru vacancies [67], or thickness inhomogeneity in ultra-thin films [68] can give rise to multiple AHE channels. These multiple AHE channels then make the "atypical humps" in the Hall resistivity measurements, without the presence of chiral magnetic texture.

Chapter 2. Growth and Characterization of ABO_3 Perovskites

In this chapter we will discuss the process of epitaxial thin film growth and characterization. We will start with our choice of susbtrate surface and their preparation and characterization in sectionn 2.1. We will then review the various tools and techniques used for work in this thesis.

2.1. Surfaces of $SrTiO_3$ Substrate

The first step towards growing high quality epitaxial thin films is choosing substrate surface. As discussed in section 1.2, the tuning of thin film functional properties are done via the choice of the substrate. Epitaxial strain, octahedral symmetry mismatch, polar orientation in high index direction, etc. require a deliberate choice of substrate surface. Here, we will discuss the preparation and characterization of singly terminated (001)- and (111)-surface of STO.

The nominal charges are Sr^{2+}, Ti^{4+} and O^{2-}. The stacking along (001) consists of layers of SrO and TiO_2 as shown in Fig. 1.3. The STO(001) surface can thus have either SrO termination or TiO_2 termination. The TiO_2 terminated surface is of more interest because of the catalytic properties and use of it as substrates in thin films growth. The widely used chemical etching method to obtain a singly terminated surface is based on etching the SrO layer on the mixed terminated surface, which makes the Ti-terminated surfaces easier to prepare.

In the ionic limit, the surface along (001) is non-polar. However, partial covalency of Ti and O bond renders even the (001) surface slightly polar which in turn diverges the surface energy of the bulk truncated surface. Relaxation of Ti and O atoms of the top

layer of TiO_2 terminated stoichiometric (1 × 1) surface that stabilizes the surface energy has been verified experimentally [69, 70, 71, 72].

A STO(001) surface has a square lattice and consists of charge neutral SrO and TiO_2 layers. On the other hand, an ideal Ti terminated (111) STO surface is strongly polar. When viewed in the [111] direction, $SrTiO_3$ consists of alternating Ti^{4+} and SrO_3^{4-} planes. These alternating positively charged and negatively charged planes create a macroscopic dipole perpendicular to the said planes. This perpendicular dipole renders the surface energy infinite and lead to a divergent electrostatic potential. The stability of such a system requires a compensation mechanism. The presence of multivalent transition metal ion (Ti) provides way for electronic reconstruction as one such mechanism. Other mechanisms often discussed are structural reconstruction of the surface, changes in surface stoichiometry, and/or adsorption from the environment.

In oxide film growth, it is often desirable to create a non-reconstructed stoichiometric surface of the substrate to achieve a sharp well-defined interface. The first step to any film growth is the preparation of the substrate surface. Various kinds of surface reconstructions, including the n × n (n=3,4,5,6) as well as other complex reconstructions have been observed in STO(111) surfaces prepared by ion sputtering followed by annealing in ultra-high vacuum . A Ti terminated (1 × 1) STO surface can be prepared following a procedure of etching with buffered hydrofluoric acid solution (BHF) followed by annealing in oxygen at 950°C [73, 74, 75]. We follow a procedure described below for both STO(001) and STO(111) surfaces. The as-received substrates are cleaned with acetone and ethyl alcohol, then sonicated in deionized (DI)-water with a pH of 5.5 at room temperature for 4 minutes. They are then soaked in Buffered HF with the pH of 4.5 for 30 seconds. Once

the chemical etching is done, the samples are then annealed at 930°C for about 150 minutes in oxygen. Fig. 2.1 a) and c) show the scanning tunneling microscopy (STM) image of a STO(001) and STO(111) substrate surface prepared in this fashion. The step heights are shown in the insets and are consistent with that of a singly terminated surface. The STM images are adapted from[76] that followed the same preparation procedure. The low energy electron diffraction (LEED) pattern in Fig. 2.1 b) and (d) shows that the surface is (1×1) non-reconstructed. We found these surfaces are stable for a wide range of temperature.

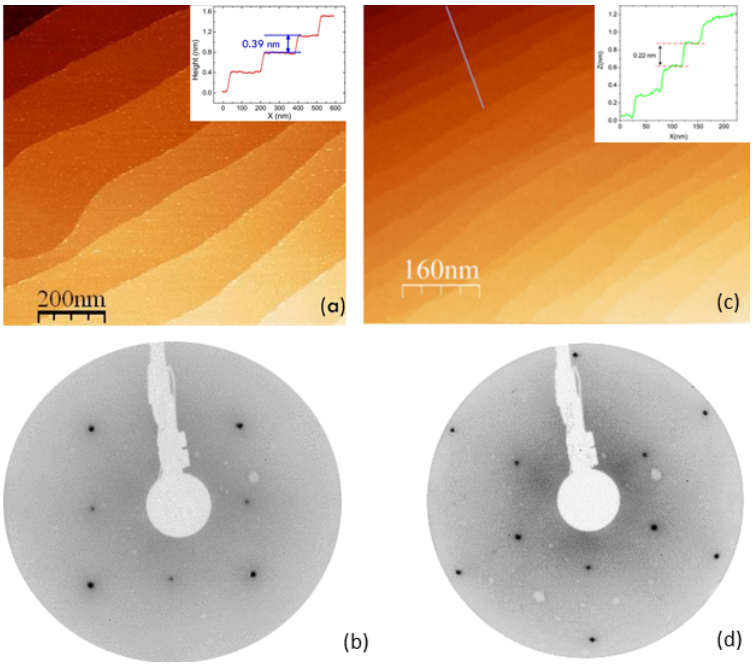

Figure 2.1. a
nd [111] crystallographic directions]a) Adapted from [76], STM image of a treated STO(001) surface. The inset shows a line profile showing steps with unit-cell heights. b) LEED pattern of a treated STO(001) showing a (1×1) structure. c) Adapted from [76], STM image of a treated STO(111) surface. The inset shows a line profile showing steps with unit-cell heights. d) LEED pattern of a treated STO(111) showing a (1×1) structure.

2.2. Epitaxy and Various Growth Modes

Epitaxial thin film growth consists of several processes at the atomic level. These processes can be categorized in the order they happen, i.e., absorption, surface diffusion, nucleation and growth. When an atom impinges on a surface, it interacts with the atoms of the surface. The impinged atom then forms a bond with the surface atom and lowers its energy. This adatom (adsorbed atom) sees a potential energy landscape defined by the atomic structure and chemistry of the surface. The growth modes are defined according to the method of nucleation of the adsorbed atoms on the surface.

2.2.1. Frank-Van der Merwe Growth (Layer by layer growth)

In this mode, the adatoms diffuse along the surface in a random walk process until they finally nucleate. Steps in the surface can act as nucleation sites. In this growth mode, as the name suggests, the second monolayer growth begins after the completion of the first layer. The general criterion for this to happen is

$$\gamma_i + \gamma_f \ \leq \ \gamma_s \tag{2.1}$$

where γ_i, γ_f, and γ_s are the interface, film, and substrate energies, respectively. This growth mode is favored in homoepitaxial growth and heteroepitaxial growth with low misfit. Strong film-substrate bonding (i.e., small γ_i and γ_f while a larger γ_s) favors this growth mode.

2.2.2. Volmer-Weber Growth (Island growth)

In this growth mode, the adatoms collide amongst themselves, form clusters, and then nucleate into stable islands. As the islands grow, they will eventually meet. As the two islands are close enough to be able to interact, they will begin restructuring to mini-

mize the energy in the systems. This is called island coalescence and begin way for nucleation of a new generation of islands. When the criterion 2.1 is not satisfied, i.e.

$$\gamma_i + \gamma_f \geq \gamma_s \tag{2.2}$$

2.2.3. Stranski-Krastanov Growth (Mixed growth)

In this kind of growth mode, the growth mode changes from layer by layer to island mode after one or two monolayers.

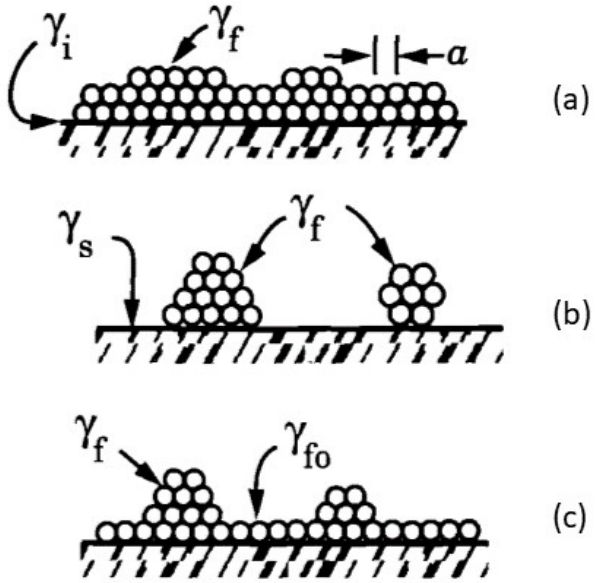

Figure 2.2. Film growth modes (a) Frank-Van der Merwe (layer by layer), (b) Volmer-Weber (island mode), and (c) Stranski-Krastanov (Mixed mode). Figure from [77]

2.3. Pulsed Laser Deposition

Pulsed Laser deposition (PLD) has been used to deposit high quality thin films of materials for over a decade. This technique uses high power laser pulses to ablate materials from the surface. Generally, the range of wavelength for material deposition lies between 200 nm and 400 nm. Most materials exhibit strong absorption in this spectral region. Towards the short wavelength end of this range is favorable because the absorption

coefficient tends to increase and at the same time the penetration depth decreases. So, only a very thin layer of the target can be ablated. Another important factor to consider is the high energy density (≈ 1 J/cm^2) in the relatively wide area (10 mm^2) preferred in the laser deposition of most materials. For these reasons, the laser of choice in PLD growth is the excimer laser. Excimer laser is a gas laser system. Noble gases like krypton do not form chemical compounds. Energy is pumped into the gaseous mixture (Kr, Fluorine) through avalanche electric discharge excitation. These noble gases form temporary bonds with halogens and form excimer molecules. The excimer is a metastable (bound) state whereas the ground state is repulsive (or very weakly bound). Many chemical reactions occur in the formation of excimer molecules. Once the excimer is formed, it will decay via spontaneous emission and collisional deactivation giving the molecule a lifetime of ≈ 2.5 ns. The energy requirement for pulsed laser deposition is several hundred millijoules per pulse which requires an excimer population density on the order of 10^{15}/cm^3, and the formation rate of the excimers should be around 10^{23}/cm^3/s. This creates a strict requirement on the discharge parameters.

The deposition chamber is a very important component of PLD system. An ultra-high vacuum (UHV) chamber with all the essential ports for laser beam, target, and sample manipulation is essential. The UHV is maintained usually with the help of a cascade of diaphragm pumps, turbomolecular pumps and ion-pumps. A schematic of a deposition chamber is shown in Fig. 2.5 (a). Six targets can be mounted on the target carousel at one time. The target rotation with the help of a motor during growth ensures uniform erosion of the target material. Switching between targets is also made possible with the help of gears which makes the superlattices growth possible. The substrates are usually

required to be heated. The heating of the substrates is achieved by applying voltages to resistive heaters (Pt- wires) that are wound around ceramic plate which sits on a holder. The temperature of the substrate is recorded with the help of an infrared pyrometer.

2.4. Reflection High Energy Electron Diffraction (RHEED)

The ablated material is collected on an appropriately placed substrate (inside the UHV chamber, as shown in Fig. 2.5) upon which it condenses, and the thin films grows. The real time growth monitoring is performed with the help of RHEED apparatus (see Fig. 2.3). A high energy (10-50 keV) electron beam is produced and accelerated by the electron gun and is focused onto the sample at a glancing angle with the help of two (magnetic) lenses. The angle is usually limited to 0.5° to 6°. Hence the size of the irradiated area on the sample is usually 1-3 mm along the beam path. These high energy electrons penetrate most materials several hundred nanometers in normal incidence. But at these grazing incidences this penetration depth is greatly reduced to about a few nanometers. Therefore, RHEED is highly surface sensitive. The RHEED pattern is observed on a fluorescent screen which can then be recorded on a CCD camera from outside the chamber. A differential pumping station connected to the RHEED apparatus maintains good vacuum in and around the electron gun and allows the RHEED operation with oxygen environment in the sample space.

Fig. 2.3 (b)shows the relationship between the geometrical construction of the RHEED setup with the reciprocal space. κ_0 is the wavevector of the incident electrons. Since we only consider elastic scattering κ_1 and κ_2 have the same magnitude as κ_0 and therefore their endpoints are on a sphere of radius $|\kappa_0|$. If we assume that the atoms in

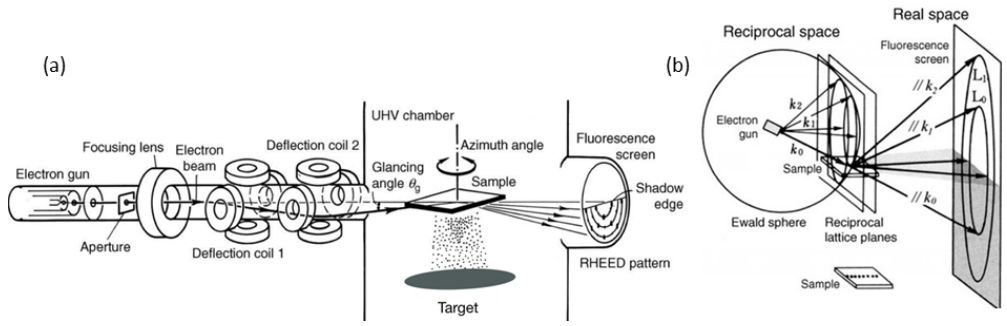

Figure 2.3. (a)Schematics of a RHEED apparatus and (b) Ewald Construction (Figures adapted from [78])

the crystal sample are arranged in a line as shown in the Fig. 2.3(b), the reciprocal lattice planes are perpendicular to the lines and the point of intersection of these planes with the Ewald sphere form a series of circles. Only half of these circles are observed on the RHEED screen. On a real sample (for example a square lattice), the reciprocal lattice is an intersection of two series of perpendicular equidistant planes rotated by 9° to each other. This is a set of rods. And these rods are equidistant and stand perpendicular to the sample surface. Therefore, the intersection between Ewald sphere and these rods are points on the circle. The RHEED diffraction is very sensitive to the surface quality of the sample. Due to imperfection on the surface, the RHEED pattern undergo various modifications. For different non ideal surface scenarios the RHEED pattern undergo distinct changes. A flat single crystalline surface, with minimal defects, give rise to sharp spots. A surface with multiple small domains makes the RHEED diffraction spots streaky, which is common with thin films. However, in case of three-dimensional columnar growth, transmission spots are observed. In PLD of thin films on crystalline substrates, RHEED offers real time monitoring of the thin film growth. The intensity of the specular diffraction spot oscillates in response to the change in roughness of the surface as the growth begins.

These so called "RHEED Oscillations" serve as real time monitoring of the thickness of the film being grown.

2.5. Low Energy Electron Diffraction (LEED)

A low energy electron (typically in the range of 20 to 200 eV) when diffracted from the surface of a sufficiently at crystalline surface gives information about the structure and symmetry of the topmost few layers of the sample. The reason for this is the much smaller penetration depth of the low energy electron. For example, an electron with energy of 100 eV penetrate on the order of 1 nm before being scattered which makes LEED a sensitive technique for surface structure measurement. The LEED instrument consists of an electron gun and a Screen System. The electron gun together with the control unit maintains a very low beam current (approximately 10^{-9} A) necessary for measuring (Intensity vs Beam Energy) I-V beam profiles. A standard screen is shown in Fig. 2.4. It consists of four hemispherical concentric grids and a fluorescent screen each containing a hole at the center through which an electron gun is inserted. The first grid is grounded to ensure a field free region between the sample and the first grid. The second and third grids are called suppressor grids and are kept at small negative potential to allow for a small range of elastically scattered electrons to be transmitted to the screen. The fourth grid is grounded to reduce the field penetration of the screen voltage (which is usually a few kilovolts) to the suppressor grids. The diffraction pattern is displayed on the fluorescent screen. The intensity of each of these diffraction spots can then be analyzed as a function of beam energy to determine the surface structures, among other things. The observed LEED diffraction pattern would be infinitely sharp if the experiment were performed on a

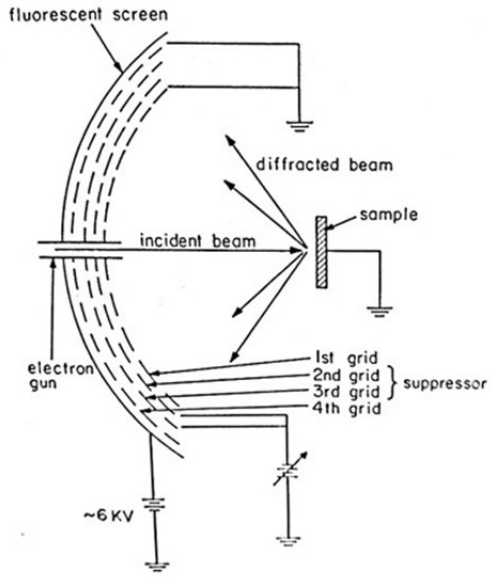

Figure 2.4. Schematics of a LEED display

perfect, rigid, and infinite crystal with a perfect instrument. In practice, these diffraction spots are of finite size due to instrumental resolution and surface imperfections. Oftentimes in a single crystal surface, an additional periodicity larger than that of the primitive unit cell of the bulk termination of the lattice is observed. This could be due to intrinsic reconstruction of the bulk terminated surface, the presence of an ordered atomic overlayer, or the presence of an ordered molecular overlayer. This additional periodicity is observed as "fractional order" diffraction spots.

2.6. Synthesis and Surface Characterization of $SrRuO_3$ Thin Films.

The (001) surface of STO was etched and annealed to obtain a TiO_2 terminated surface according to the method described in section 2.1. A stoichiometric SRO target, kept in an ultra-high vacuum chamber (10^{-9} Torr), was illuminated with a KrF excimer laser ($\lambda = 248$ nm) at a repetition rate of 10 Hz and a laser energy of 350 mJ. The target was rotated with the help of a mechanical carousel to ensure the uniform erosion of the

target material. The oxygen partial pressure of 100 mTorr was obtained with a mixture of 99 % O_2 and 1% O_3 and maintained during growth while the STO substrate temperature was kept at 700 °C with the help of resistive heaters. A surface diffraction pattern with RHEED, was obtained and its intensity monitored during the period of the growth. As the growth proceeds, the intensity oscillates enabling a coverage monitoring of the layers. Fig. 2.5 shows a schematic of a PLD chamber, with all the instruments for growth. Panel

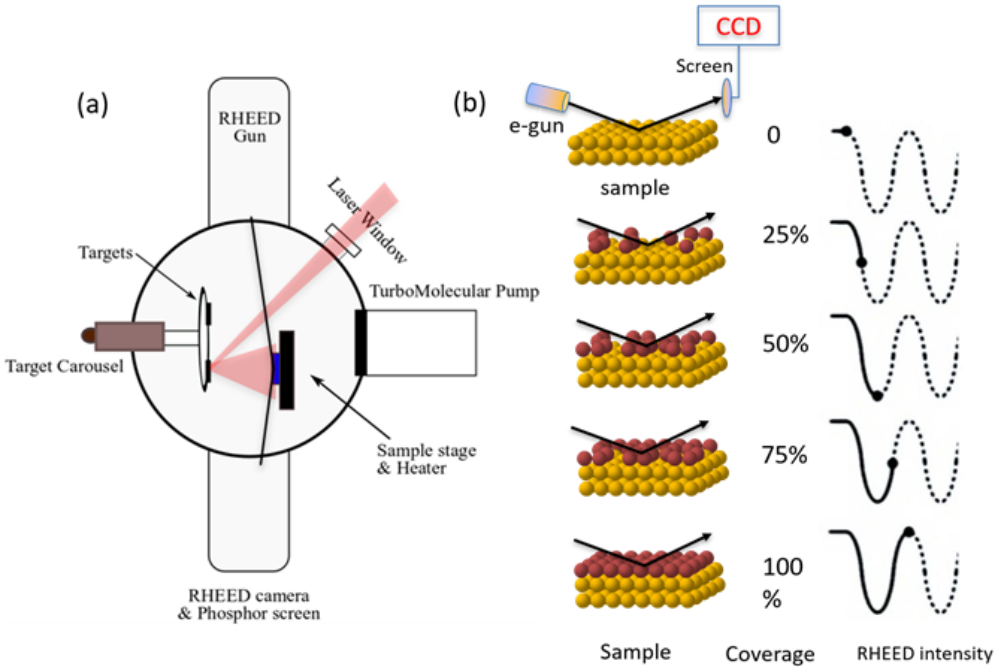

Figure 2.5. (a) Schematics of a PLD chamber. (b) RHEED intensity oscillating as a function of layer coverage.

(b) shows a cartoon picture of how the RHEED intensity oscillations results from the coverage of materials on a surface. As the film coverage begins, the intensity of RHEED diffraction spots start to drop only to regain once the coverage exceeds 50% of the monolayer coverage. The max intensity is achieved when the layer is complete and smooth. Fig. 2.6 shows the actual RHEED intensity oscillations for SRO film growth on a STO(001) substrate. The intensity of RHEED diffraction spot oscillates for a few unit cells of depo-

sition and eventually saturates suggesting a typical change in growth mode [79] of SRO from layer-by-layer mode to step flow mode. Due to the volatile nature of RuO_2, SrO termination is preferred and corresponds to the peak in the RHEED intensity oscillations [80]. The period of the first peak in the RHEED intensity is about 1.5 times the average period of subsequent peaks suggesting that a termination conversion happens during the initial growth of SRO films on TiO_2 terminated substrate surface.

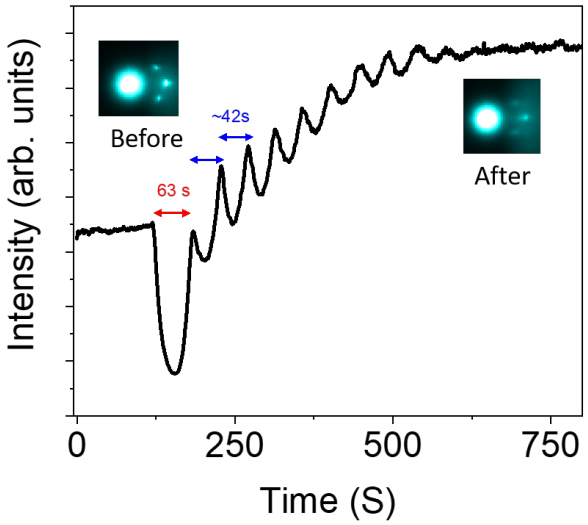

Figure 2.6. (a) Intensity of RHEED specular spot oscillates as the growth progresses as shown. The left inset shows the RHEED image before growth and the right inset shows the RHEED image after growth.

2.7. High Resolution X-ray Diffraction

X-rays when incident on a material, may be scattered elastically by electrons, which is named Thomson scattering. This elastic scattering conserves energy and momentum of the incident X-rays and is used for structural investigations of materials. W. L. Bragg in 1912 described a qualitatively simple method of obtaining the diffraction conditions. He considered diffraction as simultaneous reflections from various lattice planes of

the same family of planes (see Fig. 2.7). If the path difference between the wave reflecting from D and B (2dsinθ) is integer multiple of wavelength (λ), then the two waves combine themselves with positive interference.

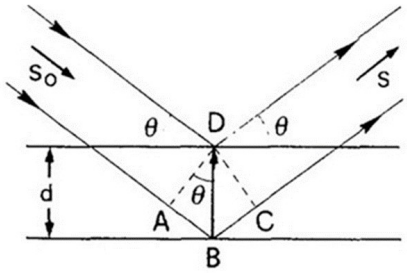

Figure 2.7. Bragg reflection from two lattice planes.

$$2d\sin\theta = n\lambda \tag{2.3}$$

In a crystal lattice, the value of d can be deduced from the crystal symmetry and the crystallographic direction in which the diffraction measurement is performed. For example, in a simple cubic lattice,

$$d = \frac{a}{\sqrt{h^2 + k^2 + l^2}} \tag{2.4}$$

where, a is the lattice constant and (hkl) are the miller indices of the family of planes from which the diffraction occurs. In Laue approach, if the X-ray incoming wave is thought as being a particle, then the problem becomes that of scattering of the particle by some potential V(r), which it experiences when going through the sample. The scattering transition rate is given by

$$\Gamma(\mathbf{k'}, \mathbf{k}) = \frac{2\pi}{\hbar} |\, \langle \mathbf{k'} | V | \mathbf{k} \rangle \,|^2 \, \delta(E_{\mathbf{k}'} - E_{\mathbf{k}}) \tag{2.5}$$

However, if the sample is a periodic crystal, then the matrix element $\langle \mathbf{k'}|V|\mathbf{k}\rangle$ is zero unless **k-k'** is a reciprocal lattice vector. Hence the Laue condition

$$\mathbf{k} - \mathbf{k'} = G \tag{2.6}$$

Equations 2.3 and 2.6 are essentially equivalent. When a crystalline thin film is grown on an atomically at single crystal substrate surface, the crystallinity of the substrate is continued onto the film. This is referred as "epitaxial thin film" growth. These epitaxial thin films exhibit high degree of crystalline perfection. But defects and imperfections are unavoidable. To measure these deviations, a higher instrument resolution (seconds of an arc) is usually required which is achieved by using double crystal diffractometers in the incident and the diffracted beam path. For continuity of structure in heteroepitaxial film growth the strain needs to be incorporated into the layer. This oftentimes happens with changes in the lattice of the film. The strain is measured as the difference in the in-plane lattice constants between the substrates and the bulk material of the film and is called 'mismatch'. The mismatch is usually accommodated by extension or shrinking of the out of plane lattice in strained films.

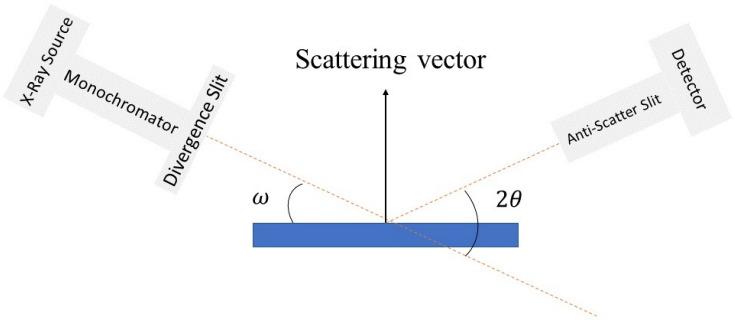

Figure 2.8. X-ray Diffraction Setup.

A typical high-resolution diffraction setup is shown in Fig. 2.8. A crystal of Germa-

nium is used to monochromate and collimated the incident X-ray beam. The crystals are cut along certain directions and sometimes two such crystals are oriented to gain larger monochromaticity. A 4-bounce Ge (220) monochromator has a resolution of 0.0033° and better monochromaticity in that it only lets part of Kα_1. Higher resolution comes with a price in intensity decrease. The intensity diffracted by Ge (220) 4-bounce crystal is almost 1/100 of that using a conventional slit collimation.

There are two types of measurements for thin films, symmetric and asymmetric scans. In symmetric scan, the scattering vector, **K** is fixed along perpendicular to the surface, and only the length of **K** is changed, while in asymmetric scan the scattering vector has an offset from normal to the surface. Symmetric scan is used to measure the lattice constant, crystallinity and phase of the thin film while asymmetric scans are often used to measure mosaicity. Fig. 2.9 shows a typical $2\theta/\omega$ coupled scan about the pseudo-cubic (002) symmetric Bragg peak of SRO film grown of STO(001). The (002) substrate peak and the (002) film peak are labelled. From the shift in the film peak compared to the substrate peak, one can calculate the out of plane lattice parameter of the film. In addition, interference fringes are also present. The fringe separation (β) can be used to estimate the overall film thickness. The fit alongside the experimental data in Fig. 2.9(a) is obtained by using a modified kinematical theory of diffraction, wherein absorption effects are taken into account by introducing an attenuation factor [81].

The out-of-the-plane lattice constant increased to 3.95 Å from the bulk pseudo-cubic value of 3.926 Å. Such a lattice expansion is expected because of the compressive strain from the substrate. Fig. 2.9 (b) shows the Reciprocal Space Map (RSM) about the (-103) asymmetric diffraction peak. The substrate peak and the film (-103) peak are la-

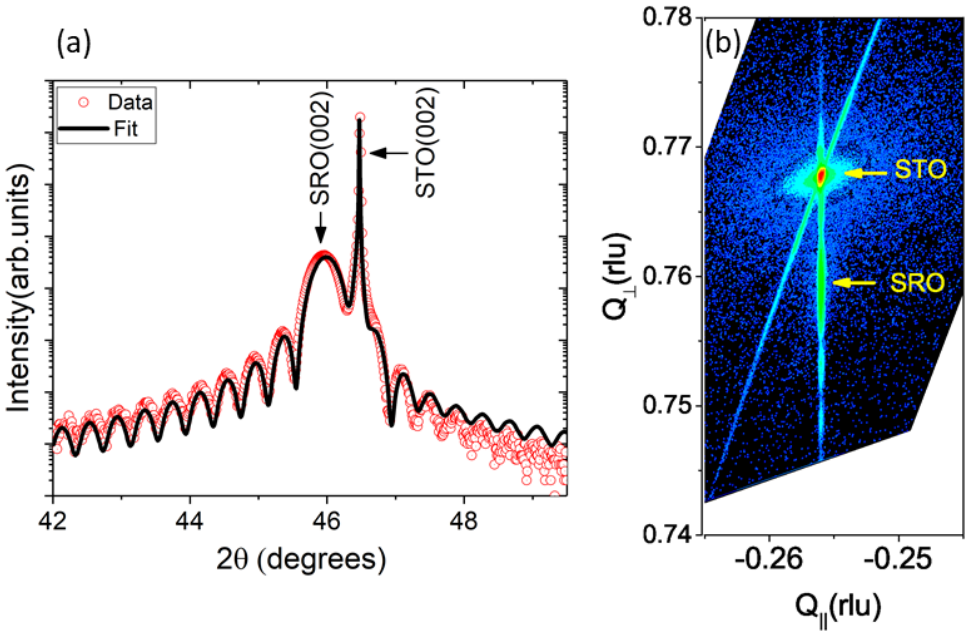

Figure 2.9. ω-2θ scan about the (002) peak of $SrRuO_3$ thin film grown on $SrTiO_3$(001) substrate. The Laue oscillations along with the Bragg peaks are fitted according to [81]. (b) The reciprocal space map (RSM) about the (-103) asymmetric peak of the same sample. The film peak and the substrate peaks are labeled

belled. The vertical $Q_\perp$ axis is parallel to the out-of-plane direction of the film. The horizontal direction, $Q_\parallel$ is the in-plane direction. The film and substrate peaks line up in the perpendicular direction suggesting the film is highly strained in-plane to the substrate.

2.8. Transmission Electron Microscopy

The Transmission Electron Microscope (TEM) operates on the same basic principles as the light microscope but uses electrons instead of light. Because of the smaller wavelength of electrons, the optimal resolution for TEM images is orders of magnitude smaller. Fig. 2.10 shows a schematic of the Scanning Transmission Electron Microscope configuration. A series of lenses focuses a beam of electrons to form a small spot which is then incident on a thin electron-transparent sample. The aim of the lens system is to convert the finite size electron source into an atomic scale probe. The condenser lenses

perform the initial demagnification of the electron source, followed by an objective aperture and objective lens. The objective aperture is in place to reduce the aberration from the larger objective lens. The objective lens performs the larger demagnification and the aberrations in the objective lens can lead to significant blurring of the electron probe. The transmitted electrons are then focused onto a phosphor screen or a CCD camera. The scan coils allow to scan the sample in a raster and a variety of scattered signals are collected as a function of probe position. The transmitted electrons that leave the sample at a relatively low angles with respect to the optic axis are collected in what is commonly referred to as "bright field" (BF) mode while those that leave the sample at relatively higher angles are collected in "annular dark field" (ADF) mode. A spectrum of the electrons that have lost energy as they pass through the sample as a function of the energy lost is referred as "Electron Energy Loss Spectroscopy" (EELS). This provides an opportunity to probe atomic structure, chemistry, and electronic properties in real space with atomic resolution.

2.9. Magneto -Transport Measurements

2.9.1. Magnetic Measurements

The magnetization data are taken using the Reciprocating Sample Option (RSO) in a Quantum Design Magnetic Properties Measurement System. Unlike DC measurements where the sample is moved through the coils in discrete steps the RSO measurements are performed using a servo motor which rapidly oscillates the sample. These measurements have a sensitivity of 5×10^{-9} emu. The MPMS consists of a Temperature control system, a magnet control system (0 to $\pm$ 7 Tesla), a superconducting SQUID detector system, and a

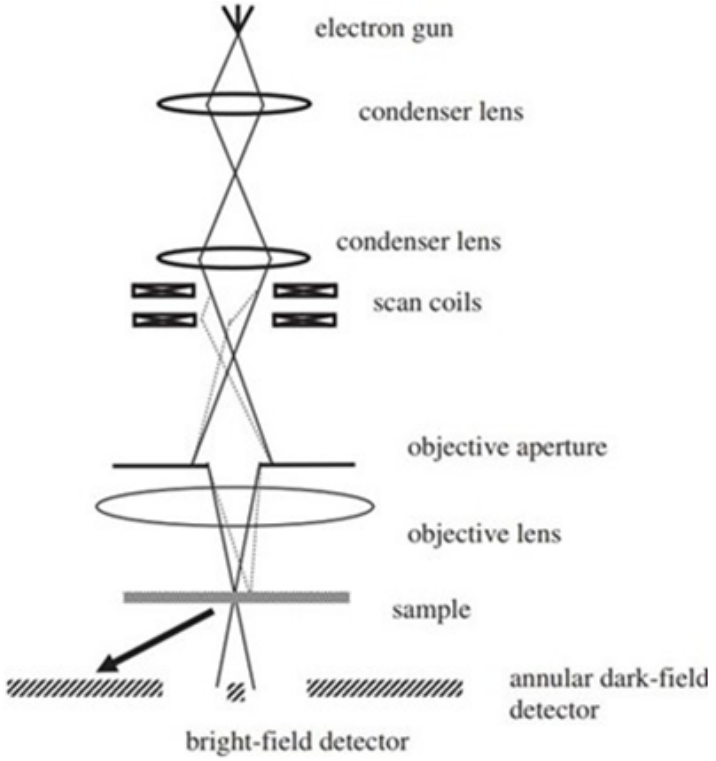

Figure 2.10. A schematics of a scanning transmission electron microscope setup

computer user interface. The sample is mounted on a plastic straw, which is then attached at the end of a sample rod. The sample rod is then inserted into the MPMS sample chamber. A centering scan is then performed to ensure the sample is at the center of the pickup coils. Once the sample is centered magnetization measurements can be started. MPMS is capable of measuring magnetization measurements while varying temperature or magnetic field.

2.9.2. Transport Measurements

The transport properties of the samples are measured with a commercial Physical Property Measurement System (PPMS). The electrical resistivity of the samples is measured using the DC Resistivity option of the PPMS. Four platinum wires are attached to

the samples using silver epoxy or indium shots in the four-probe configuration. The sample is then mounted on the sample puck, which is then inserted into the PPMS sample chamber. During the measurement, the hardware will pass a current through the sample via two leads, using the other two leads to measure the electric potential drop across the sample. The resistance is then calculated by Ohm's law.

Chapter 3. Thin Films $SrRuO_3$ Along the [001] Crystallographic Direction of the $SrTiO_3$ Substrate.

3.1. Introduction

As discussed in Section 1.5, the properties of ultra-thin SRO films show anomalous properties. We also discussed various studies by the scientific community to understand these anomalies. We believe that the loss of ferromagnetism and metallicity in ultra-thin regime are intricately associated with microscopic structural modifications in this thickness regime, which is surprisingly left in a lot of these studies. In this chapter, we will make an effort to study, on the microscopic level, the structure of ultra-thin SRO and it's interface with STO.

The contents of this chapter are arranged as follows. We will discuss the growth with PLD and their structural characterization with X-ray diffraction in section 3.2. With the help of *in situ* electron diffraction (section 3.3) and *ex situ* transmission electron microscopy studies (section 3.4), we present an in-depth structural characterization of $SrRuO_3$(001) ultra-thin films. In section 3.5 we will present our study of the magneto-transport in these films. And finally, we will provide a summary of our results in section 3.6.

3.2. Growth and Structural Characterization with X-ray Diffraction.

Thin films of SRO are grown on Ti terminated STO(001) surface obtained by the method of chemical etching followed by oxygen annealing as described in section 2.1. The growth of these films with PLD follows as described in section 2.6. Fig. 3.1 (a) shows a

Section 3.2 - 3.4 of this chapter is publised on ArXiv as Prahald Siwakoti, Zhen Wang, Mohammad Saghayezhian, David Howe, Zeeshan Ali, Yimei Zhu, and Jiandi Zhang "Abrupt orthorhombic relaxation in compressively strained ultra-thin $SrRuO_3$ films." *arXiv preprint arXiv:2106.10204* (2021)

(2θ-ω) X-ray Diffraction (XRD) scan about the pseudo-cubic (002) Bragg peak of SRO thin film. Laue oscillations are observed, indicating smooth interface and surface. These Laue fringes along with the main reflection peaks can be fitted to estimate the film thickness. The fit alongside the experimental data in Fig. 3.1 (a) is obtained by using a modified kinematical theory of diffraction, wherein absorption effects are taken into account by introducing an attenuation factor[81]. The out-of-the-plane lattice constant increased to 3.955 Å from the bulk pseudo-cubic value of 3.926 Å[32]. Such a lattice expansion is expected because of the compressive strain from the substrate. Fig. 3.1(b-c) show the rocking curve of the substrate and the film, respectively. The full width at half maximum (FWHM) of the film rocking curve (0.014 °) is close to the FWHM of the substrate rocking curve (0.008 °), suggesting that the crystallinity of the thin films is comparable to that of the substrate. Fig. 3.1 (d) shows the Reciprocal Space Map (RSM) about the $(\bar{1}03)$ asymmetric diffraction peak. The substrate peak and the film $(\bar{1}03)$ peak are labelled. The vertical Q_z axis is parallel to the out-of-plane direction of the film. The horizontal direction (Q_x axis) is the in-plane direction. The film and substrate peaks line up in the perpendicular direction suggesting the film is highly strained in-plane to the substrate.

To gain more information about the structural symmetry of SRO films, we obtained RSM around several asymmetric points. RSMs around the $(44\bar{4})$, (444), (260), (620) reflections of a 18 nm thick SRO are shown in Fig. 3.2. All the RSM show that the SRO films are coherently grown on STO substrate. The difference in the $(260)_o$, $(620)_o$, $(444)_o$ reflections positions along the vertical axis indicates that the two orthorhombic axes (a_o and b_o) are not equivalent.

SRO films compressively strained to cubic STO substrate have equal in-plane lat-

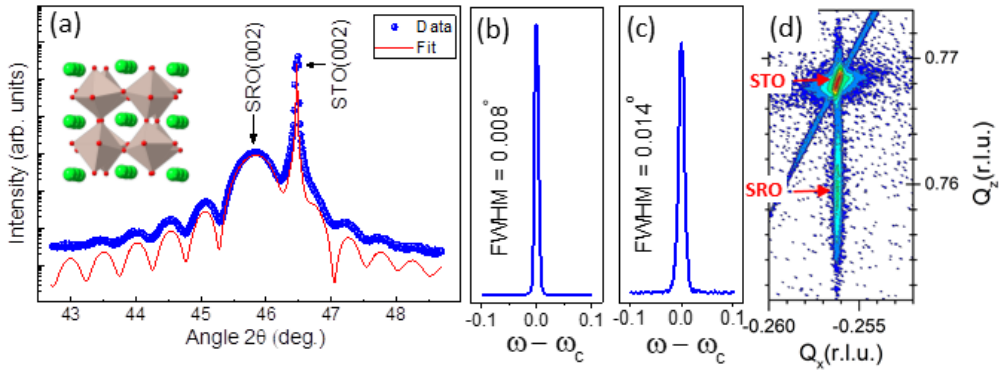

Figure 3.1. (a) $2\theta-\omega$ coupled X-ray diffraction scan of a 47 unit-cell thick SRO(001) film. The Laue oscillations along with the substrate and film peaks are fitted and presented in the red curve. Inset shows a schematic orthorhombic structure of bulk SRO. (b-c) show rocking curves of the substrate and film peak, respectively. d) Reciprocal Space Mapping about the (-103) Bragg diffraction spot. The substrate and the film positions are marked.

tice parameters ($a_p = b_p$). The compressive strain causes an extension in the out-of-plane lattice parameter (c_p). Since the lattice parameters of the orthorhombic SRO are unequal ($a_o \neq b_o$), c_p must be inclined ($\gamma \neq 90$), away from the $[001]_p$ axis as shown in Fig.1.7 (b). According to Glazer notation, the only possible tilt system that satisfies the above condition is $a^+a^-c^-$ (# 9) where two pseudo-cubic axes are inclined to each other and the third axis is perpendicular to both. The orthorhombic lattice parameters of the thin films can be refined using six RSM (hkl) reflections. The results for such refinement are listed in Table 3.1. The value of γ obtained is slightly smaller than 90°, which shows that SRO stabilizes in a distorted orthorhombic structure as discussed in section 1.4. This distortion from orthorhombic structure is to account for the substrate induced mismatch.

Table 3.1. Lattice parameters of $SrRuO_3$ films obtained from RSM analysis

a_o(Å)	b_o(Å)	c_o(Å)	γ(°)
5.57789	5.54105	7.81	89.3

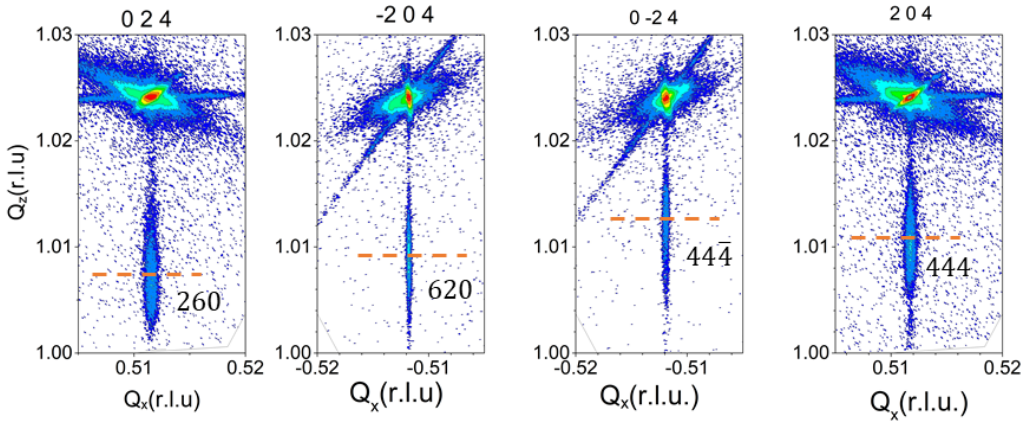

Figure 3.2. Reciprocal lattice maps around (620), (260), (444), and (44$\bar{4}$) Bragg reflections of SRO thin films on STO (001) substrate.

3.3. Surface Characterization with Low Energy Electron Diffraction

Once the growth conditions for high-quality epitaxial thin film of SRO were optimized, we grew the films with different thicknesses, including ones with extremely low thickness, to probe their structure with LEED. The LEED pattern of a bulk truncated (001) surface of STO substrate is shown in Fig. 3.3 (a). The dashed red square is the p(1×1) unit-cell. Fig. 3.3 (b) displays the LEED pattern of a 5 u.c. SRO film grown at an oxygen partial pressure P_O = 60 mTorr, at a beam energy of 74 eV. In addition to the integer spots, the unit cell for which are denoted by the dashed red square, we also observe the spots corresponding to the $(\sqrt{2} \times \sqrt{2})$R45° unit cell as shown by the solid blue square. Subsequent annealing at 630°C and P_O = 100 mTorr for 30 minutes [Fig. 3.3 (c)] did not remove the $(\sqrt{2} \times \sqrt{2})$R45° spots as the first order spots at (±1/2,±1/2) are clearly observed, though the background of the LEED pattern is slightly enhanced. The intensities of the fractional spots are comparable with that of the integer spots, suggesting that the observed $(\sqrt{2} \times \sqrt{2})$R45° pattern is due to lattice distortion result of whole film rather than a surface reconstruction. More annealing at the same temperature but higher oxygen

partial pressure (P_O = 150 mTorr for 30 more minutes) [Fig. 3.3 (d)] did not change the $(\sqrt{2} \times \sqrt{2})$R45° LEED pattern, however, an increased background was observed, indicating an enhancement of surface disorder, likely due to extra disordered oxygen adatoms. However, upon subsequent vacuum annealing for 30 minutes, the background decreased, and the high-order fractional spots became more apparent, as shown in Fig. 3.3 (e). Vacuum annealing removes the surface disorder such that the pattern in Fig. 3.3 (e) resembles the pattern of as-grown film in Fig. 3.3 (b). Surprisingly, the LEED pattern of a 1 u.c. SRO film displayed in Fig. 3.3 (f) has the same symmetry as the 5 u.c. film, though high-order fractional spots are relative weak. This clearly indicates that a distortion from cubic perovskite structure begins with a monolayer of SRO film.

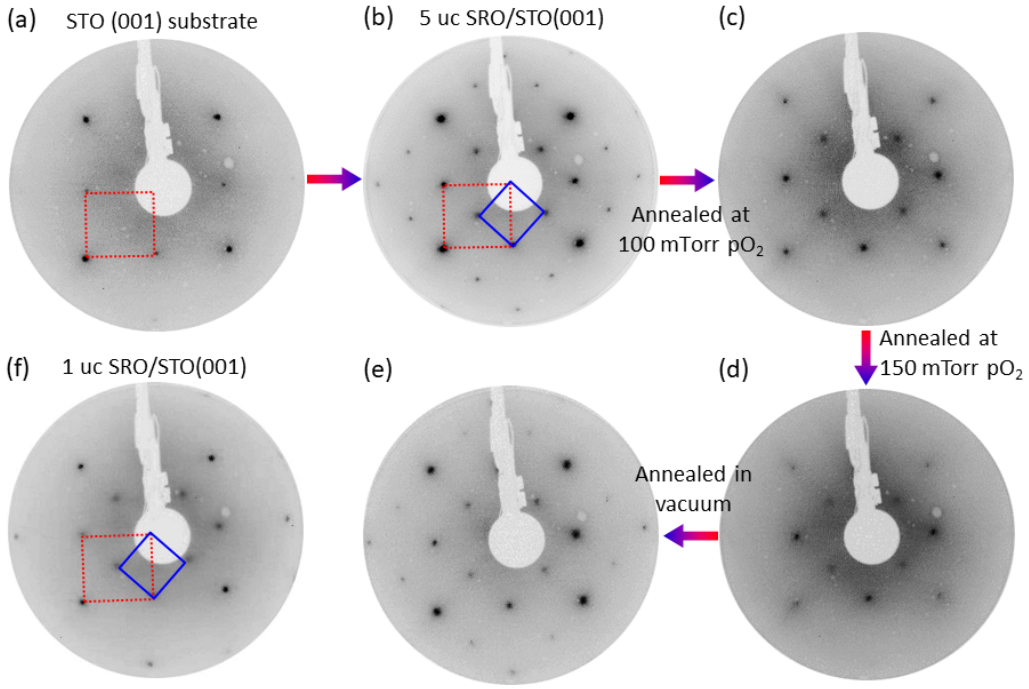

Figure 3.3. LEED images taken with a beam energy of 74 eV of (a) (1×1) Bulk truncated STO (001) surface overlapped with a red square for surface unit cell. (b) A 5 u.c. SRO film on STO (001) showing $(\sqrt{2} \times \sqrt{2})$R45° reconstructed unit cell (blue square) with respect to the substrate one. (c - e) The same sample under various annealing conditions. (f) A 1 u.c. SRO(001) film. All the LEED images are taken at room temperature.

We consider the possibility of ordered oxygen vacancies or overlayer at the surface that could give rise to the $(\sqrt{2} \times \sqrt{2})$R45° pattern next. For oxygen vacancies to create a $(\sqrt{2} \times \sqrt{2})$R45° pattern, half the oxygen atoms of the top SrO layer need to be removed. Vacancies are generally not expected owing to the ionic character of SrO bonds. DFT studies[82] have predicted a rather high energy cost ($\sim$ 7.98 eV) of forming a single oxygen vacancy. Sr vacancies were also found to be equally energetically costly (7.19 eV/vacancy). A single oxygen adatom was found to adsorb favorably on a SrO terminated surface midway between the SrO oxygen atoms similar to that observed on the surface of manganites[83]. However, such scenario is in contradiction of our experimental observation. We did not observe any change in LEED pattern by vacuum annealing at 630°C for 30 minutes (as shown in Fig. 3.3(e)) but rather an improved intensity due to decreasing background. Oxygen adatom-induced additional reconstructions have been reported in the literature for thicker SRO films. Shin *et al* [84] reported a (2×2) surface structure doubling with LEED and local domains of (1×2) and (2×1) symmetry with Scanning tunneling microscopy (STM). However, it is worth mentioning that their samples were larger than 10 u.c. in thickness and were post annealed at very high oxygen pressure ($P_O = 1$ Torr) for 90 minutes at 450°C. The robustness of these $(\sqrt{2} \times \sqrt{2})$R45° spots under vacuum as well as oxygen annealing suggest that these are not likely a result of ordered oxygen vacancies and/or over-layers.

For ultra-thin films SRO, we observe $(\sqrt{2} \times \sqrt{2})$R45° reconstruction only, similar to the surfaces of layered Sr-Ru oxides, Sr_2RuO_4[85] and $Sr_3Ru_2O_7$[86]. However, for thicker films, we observe a (1×2) overlayer structure in addition to the usual $(\sqrt{2} \times \sqrt{2})$R45° reconstructed surface as shown in Fig. 3.4 (c) for a 45 u.c. SRO(001) film. The (1×2) struc-

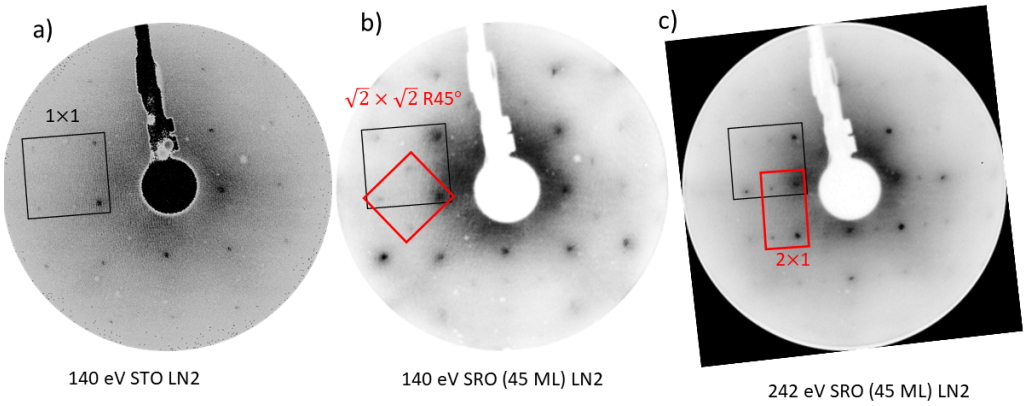

Figure 3.4. LEED image of a) STO surface at beam energy of 140 eV b) 45 u.c. SRO film at 140 eV showing $(\sqrt{2} \times \sqrt{2})$R45° reconstruction and c) 45 u.c. film at 242 eV showing a (2×1) overlayer.

ture is most likely due to adsorbed oxygen overlayer at the surface. We believe that the surface becomes more disordered with thicker coverages.

With the assumption of a pristine and stoichiometric thin film, we arrive at structural models for the surface with various configurations of tilts and rotations, as shown in Fig. 3.5. To describe the orthorhombic distortions from cubic structure, we define RuO_6 "rotation" as the rotation of the octahedra about the axis along the surface normal ([001] direction of the substrate) and "tilt" as the RuO_6 rotation about an axis in the film plane, either [100] and/or [010] direction of the substrate, as shown in Fig. 3.5 (a). If the film grows on the cubic substrate without any tilt and rotation [Fig. 3.5 (b)], the diffraction pattern would be expected to be p(1×1) as shown in Fig. 3.5 (c). Rotational distortion of RuO_6 without tilt [see Fig. 3.5 (d)] reduces the symmetry and gives rise to the $(\sqrt{2} \times \sqrt{2})$R45° pattern as shown in Fig. 3.5 (e). Forbidden fractional spots along two perpendicular directions, shown with dotted glide lines, is caused by the preserved glide symmetry. If there are both tilts and rotations of the octahedra, as in Fig. 3.5 (f), then one

or the other glide symmetry should be broken, and the corresponding simulated diffraction pattern is given in Fig. 3.5 (g). Domains with differently oriented tilts and rotations break both the glide symmetries and hence no missing fractional spots would occur. In our LEED results from Fig. 3.3, we did not observe any missing spots to indicate the presence of glide symmetry. One explanation for the absence of glide line can be the presence of structural domains where both octahedral tilt and rotation exist in each domain. Our STEM study, as will be discussed in section 3.4 , confirms the presence of structural domains. The question remains whether the octahedral distortions are just on the single layer at the surface that minimizes the surface energy or extends throughout the thickness as a means of octahedral mismatch accommodation.

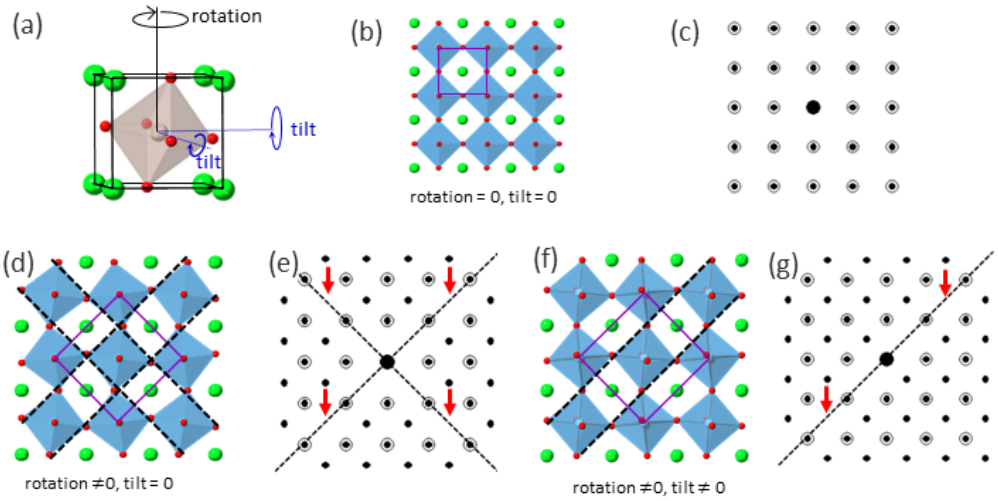

Figure 3.5. Simulated LEED diffraction patterns for different surface symmetry. (a) A schematic showing RuO_6 tilt and rotations. (b-c) top view of a square lattice with no RuO_6 rotation or tilt and the corresponding diffraction pattern. The integer spots due to a square lattice are shown as a dot with a concentric circle. (d-e) square lattice where RuO_6 octahedra are rotated but not tilted and the corresponding diffraction pattern. Fractional spots are shown as solid dots. Glide lines are shown with dashed lines. Arrows indicate the position of missing fractional spots. (f-g) Lattice with both RuO_6 tilts and rotation as well as the corresponding diffraction pattern. Only one glide line survives as shown with dashed lines.

3.4. Atomic Scale Structural Characterization with Scanning Transmission Electron Microscopy

To accomplish a rigorous structural analysis of SRO(001) thin film, we performed STEM experiments to probe the atomically resolved structure. For this purpose, we choose a thicker film (22 u.c.) and cap it with STO at the top to protect the surface. Two STEM imaging modes are commonly used. High-Angle Annular Dark-Field (HAADF) imaging is more sensitive to heavy elements, and Annular Bright Field (ABF) imaging enables us to see light elements such as oxygen. Fig. 3.6 (a-b) show HAADF- and ABF-STEM images taken along [100] direction of the cubic STO, respectively. HAADF images make the quantitative analysis of the lattice parameters possible. ABF images are used to resolve the oxygen positions, which can then be used to quantify the spatially resolved oxygen octahedral distortions. Fig. 3.6 (d-e) show the in-plane and out-of-plane lattice parameters measured from the HAADF image, respectively. The in-plane lattice parameter is equal to that of the STO bulk, while the out-of-plane lattice parameter is slightly larger than the bulk SRO value of 3.926 Å, accommodating the compressive strain from the substrate.

Fig. 3.6 (f) shows the layer-by-layer octahedral tilt evolution of the SRO films extracted from the oxygen atom displacement in the ABF image. The octahedral tilt is defined as the Ru-O-Ru bond angle (θ), as shown in Fig. 3.6 (c). The angle (θ) varies with thickness across the film. The substrate is cubic and has no octahedral tilts, $\theta = 180°$. There is an intermediate region near the interface of 4-5 u.c. shown shaded in yellow in Fig. 3.6 (f), where the tilts are suppressed before the film is completely relaxed to $\sim$168°. It is worth noting that the tilt begins with the first u.c. of RuO_6 octahedra. This is con-

sistent with the observed $(\sqrt{2} \times \sqrt{2})$R45° LEED pattern from a single u.c. SRO film [Fig. 3.3 (f)] where the in-plane rotational distortion was confirmed.

The LEED observation is complementary to the STEM imaging. The in-plane rotation (about the $(001)_p$ axes) of octahedral, which results in the displacements of neighboring oxygen atoms along the beam direction, cannot be resolved with STEM. We also observed a reduced tilt of a few layers octahedra at the top of the SRO film where we have capped with STO, to protect the surface. The capping with STO also suppresses the tilt distortions in agreement with earlier studies[87]. One interesting thing is to see how the lattice distortions evolve across the interface, given by a mismatch in structural symmetry between films and substrates. Both bulk SRO and $CaRuO_3$ (CRO) are orthorhombic, but CRO has larger lattice distortion and is less conductive. When interfaced with STO, they exhibit different effect on the interface structural distortions.

Fig. 3.6(g) shows the oxygen octahedral tilts near the interface of SRO and CRO with STO. Both films take about the same thickness (4-5 u.c.) from the interface to fully relax to the bulk orthorhombic structure, regardless that SRO is ∼0.5% under compressive strain while CRO is ∼0.6% under tensile strain. In SRO/STO, TiO_6 octahedra near the interface of the STO substrate are undistorted by maintaining a Ti-O-Ti bond angle of 180°. The accommodation of the interfacial rotation mismatch happens only in the RuO_6 octahedra of the film. In contrast, for CRO/STO, the accommodation involves tilting of the TiO_6 octahedra in the top few layers of the substrate. Similar tilting of the TiO_6 octahedra[88] as well as interfaced induced polarization of STO[89] were observed when interfaced with LSMO thin films. This shows that the octahedra in SRO are more amenable to tilt and rotational distortions than CRO and LSMO, thus exhibiting an

abrupt structural relaxation across the interface with no effect on the substrate. It is likely because SRO is less distorted in lattice and more itinerant in electronic structure than CRO, though further study is need.

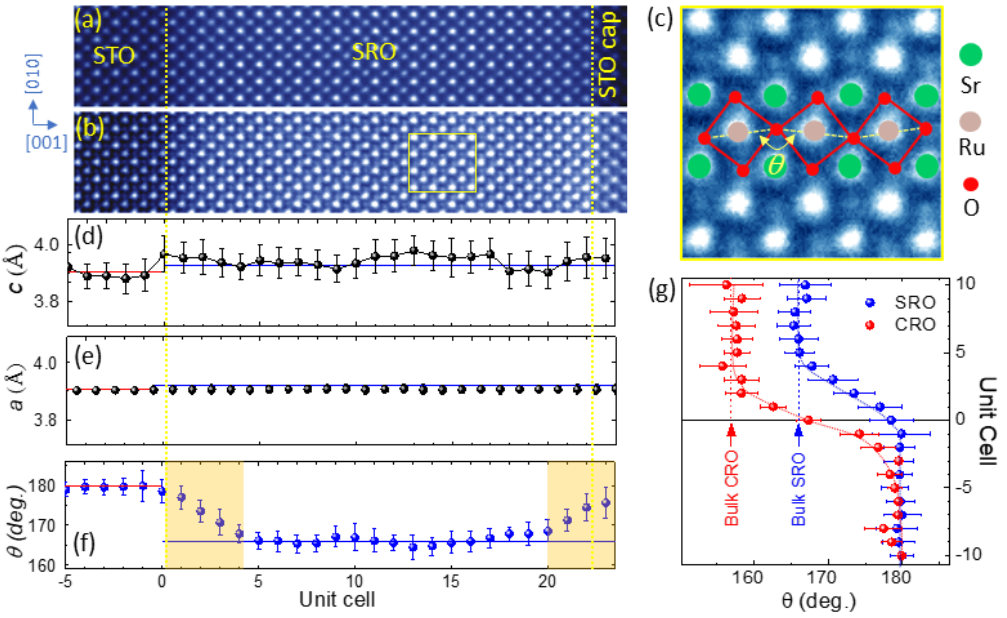

Figure 3.6. Quantitative analysis of a 22 u.c. SRO film with STEM. (a) HAADF and (b) ABF images taken along the [100] direction of the substrate. (c) A zoom-in of a region of ABF image in (b) overlapped with schematic octahedral rotations. (d) The out-of-plane (OOP) and (e) in-plane (IP) lattice parameters extracted from the HAADF images plotted as a function of thickness. Both the substrate STO-film interface and the capping STO-film interface are shown as orange dashed lines. Red and blue lines mark the pseudo-cubic lattice parameters of the corresponding bulk structures, respectively. (f) The oxygen octahedral tilt angles extracted from the ABF image in (b) is plotted vs. film thickness. The Ru-O-Ru bond angle of 180° for STO (red line) and 166° for bulk orthorhombic SRO (blue line) as well as the emphasized interface regions (shaded) are marked. (g) A comparison of octahedron tilts near interface of SRO/STO and CRO/STO.

SRO films are orthorhombic in symmetry and when compressively strained to cubic STO substrate follow the tilt pattern of $a^+a^-c^-$ (# 9), where two pseudo-cubic axes are inclined to each other and the third axis is perpendicular to both. Therefore, we can expect four 90° rotated domains shown in Fig. 3.7 (a). We define the four domains as A, B, A' and B'. Domains A and A' as well as domains B and B' are indistinguishable

in STEM images. These domains are distinguished by the direction of the in-phase rotation axis (shown in red arrow) of the octahedra with respect to the cubic axes of the substrate. Domains A and A' have the in-phase rotation axis along the [100] of the substrate while domains B and B' have the in-phase rotation axis along the [010] direction. STEM images taken along the [100] direction show two structural domains (A/A' vs. B/B'). In addition to the structure shown in Fig. 3.6, we also observed another region with a different structural symmetry. The two structures are clearly distinguishable by comparing the Fast Fourier Transform (FFT) results of the ABF images. Fig. 3.7 (b) shows the FFT of the ABF image of the structural domain shown in Fig. 4.3 and the simulated diffraction pattern obtained using orthorhombic SRO ($a^+a^-c^-$ model structure) with the in-phase rotation axis as the beam direction. Simply based on the pattern symmetry without detailed quantitative analysis of octahedral rotations, the simulated pattern agrees well with the observed FFT image. We therefore identify this structure to be that of the domain A (and/or A') shown in Fig. 3.7 (a). The in-phase rotation axis is shown in red and is along the [100] direction of the STO substrate.

The experimentally observed FFT pattern shown in Fig. 3.7 (c) (left) for the second structural domain has a different symmetry, as compared with the FFT pattern for domain (A/A') shown in Fig. 3.7 (b). The experimental FFT matches the simulated diffraction pattern of the 90° rotated structure of the previously described $a^+a^-c^-$ model structure, which is shown in the right panel of Fig. 3.7 (c) with additional (1×2) diffraction spots (red circled). This structural domain is thus identified as domain B (B') as shown in Fig. 3.7 (a). In principle, LEED could display such a (1×2) diffraction pattern if electron mean free path was long enough to reach the second unit cell from the surface

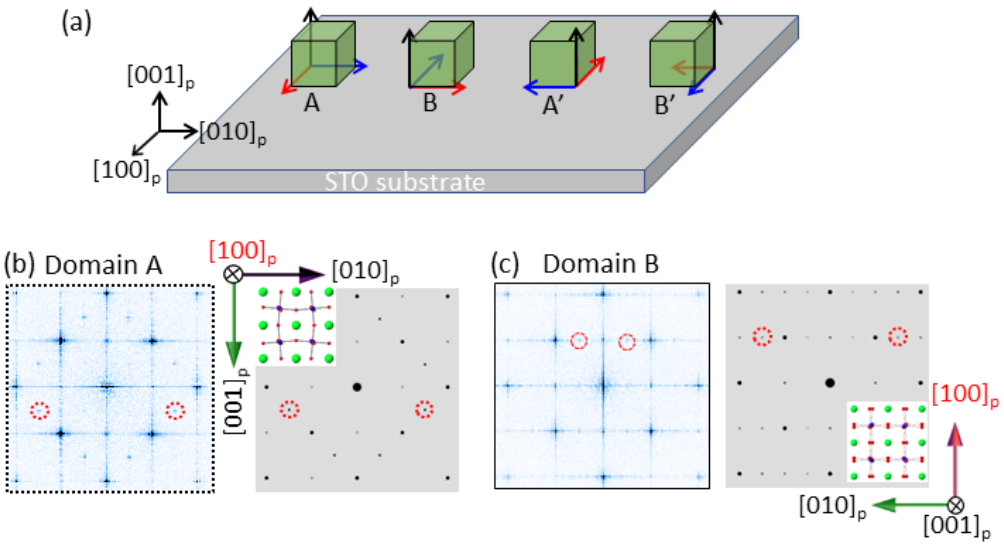

Figure 3.7. (a) Four 90-degree rotated domains are expected as shown. Red arrow points to the direction of in-phase rotation of the neighboring octahedra in Glazer notation. Two distinctly different domains are observed in STEM taken along [100] beam direction. (b) FFT of domain A and simulated diffraction obtained with the beam direction the same as the direction of in-phase rotation of the model structure (inset). (c) FFT of domain B and simulated diffraction with the beam direction perpendicular to the in-phase rotation axis.

to provide the information. Nevertheless, two types of structural domains observed in the TEM are identified as the two 90° rotated structural domains of the $a^+a^-c^-$ structure of SRO.

3.5. Magneto-transport Properties in $SrRuO_3$ Thin Films.

The resistivity of 21 u.c. film shows metallic behavior in the whole temperature range (see Fig. 3.8 (a)). The value of residual resistivity ration (RRR), which is defined as the ratio of resistivity at 300 K to the resistivity at 2 K, is ~ 5.3. The resistivity shows a kink in the vicinity of transition temperature. A sharp peak is observed in the derivative ($d\rho/dT$) as shown in the inset in Fig. 3.8 (a). Fig. 3.8 (b) shows the magnetoresistance (MR) behavior at 2 K. The MR is defined as $((R(H) - R(0))/R(0)) \times 100\%$. The magnetic field was applied perpendicular to the sample, while the current was applied

in-plane. The magnetoresistance hysteresis shows butterfly loop characteristic of ferromagnets. Magnetoresistance in SRO is believed to contributed mostly by the domain wall resistance[90]. And naturally the hysteresis in MR can be thought of as caused by domain wall pinning. Fig. 3.8 (c) shows the anomalous Hall resistivity of the SRO film measured at 2K. Both MR and Anomalous Hall resistivity show signs of a second magnetic phase. These two phases possibly have different coercivity behavior indicating a presence of two spin-polarized conduction channels.

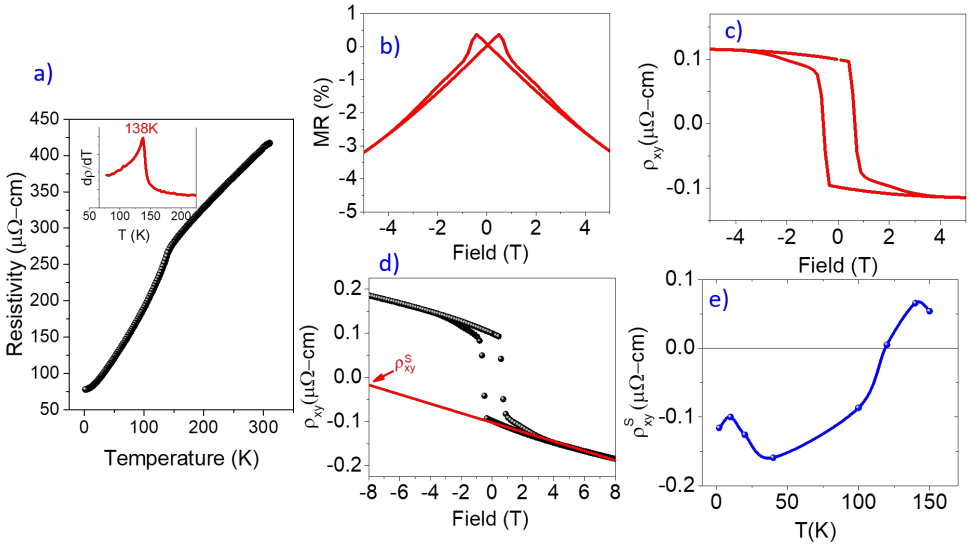

Figure 3.8. Magneto-transport of 21 u.c. SRO film. a) Resistivity behavior with temperature. The inset shows the derivative dρ/dT. B) MR at 2 K and c) Anomalous Hall resistivity at 2K. d) Total Hall resistivity (including the ordinary component). Saturation resistivity is defined as the intercept of high field line (extrapolated). And e) The saturation resistivity evolves with temperature to show non-monotonic temperature dependence and a sign inversion.

Fig. 3.8 (d) shows a typical Hall resistivity data at 2 K that contains both ordinary and anomalous contribution with different Hall constants.

$$\rho_{xy} = \mu_0 \left(R_0 \mathbf{H} + R_{AH}(\rho) \mathbf{M} \right) \tag{3.1}$$

The saturation Hall resistivity is defined by the extrapolation of linear high field data to

the zero field. In such, ρ_{xy}^{S}, is given by the product of the anomalous Hall constant and the saturation magnetization M_S.

$$\rho_{xy}^{S} = \mu_0 R_{AH} \mathbf{M}_S \tag{3.2}$$

Since the M_S is saturated at high fields, the saturation resistivity gives the behavior to AHE. Shown in Fig.3.8 (e) is a typical temperature evolution of AHE, as indicated by the temperature evolution of ρ_{xy}^{S}. It shows non-monotonic temperature dependence and a sign inversion around 120 K. At higher temperature, the AHE decreases in magnitude and becomes positive. Fig. 3.9 (a) shows this behavior of the data more clearly. The AHE behavior can be simulated with two AHE components as shown in Fig. 3.9 (b). The curves in black and red are individual components modelled by $R_{xy,1}^{H} \tanh \omega_1 (B - B_{c,1}) + R_{xy,1}^{H} \tanh \omega_2 (B - B_{c,2})$ such that the resultant simulated graph shown in blue qualitatively match the observed Hall resistivity behavior. $\omega_{1,2}$ are parameters related to the slope at B_c. We observe that the temperature dependence of the hall behavior can be qualitatively reproduced by considering two spin-conduction channels in our system. This shows that even in a single layer of thin film, the structural inhomogeneity (i.e. presence of multiple strucutral domain boundaries) could provide pinning sites and thus give rise to a larger coercivity contribution to the AHE. The two channels evolve as a function of temperature and eventually switches direction. These two channels have different coercivities, however their temperature evolution is somewhat similar in that they switch sign around the same temperature consistent with the behavior of single SRO layer. Fig. 3.9 (b) at 120 K shows two distinct loops consisting of four different magnetic and resistive states.

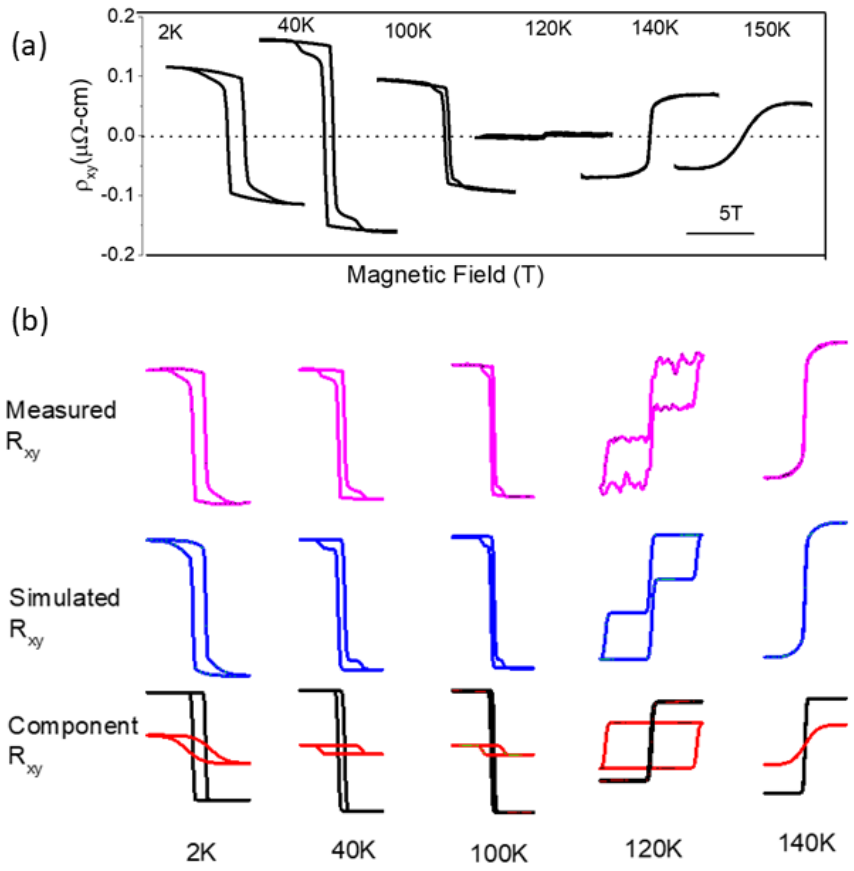

Figure 3.9. Temperature dependent behavior of AHE. (a) Raw AH resistivity sweeps for various tempertures of 21 u.c. SRO(001)film. (b) Two component fitting of the AHE. Top row shows measured AH resistance while the middle and bottom rows show simulated AHE behavior. In the bottom row attempt is made to make a qualitative description of how two channel components could add up to the total Hall effect we measure in materials.

Extraordinaly Hall balance (EHB) is a device created by stacking two different ferromagnetic layers separated by a non-magnetic layer creating a memory device with four states[91]. SRO ultrathin films bilayer separated with STO spacer was recently used to realize an EHB device[92]. Upon close inspection of our 120K Hall data, we observe four distinct resistive states due to the superposition of a larger coercive and a smaller coercive region of ferromagnetism as shown in Fig. 3.10. This is the requirement for realizing such a device. While these states are separated by a very small resistivity difference for any

device application, we can confirm the presence of multiple hysteretic components in our samples. We attribute this extra conduction channel to the structural inhomogeneity asso-

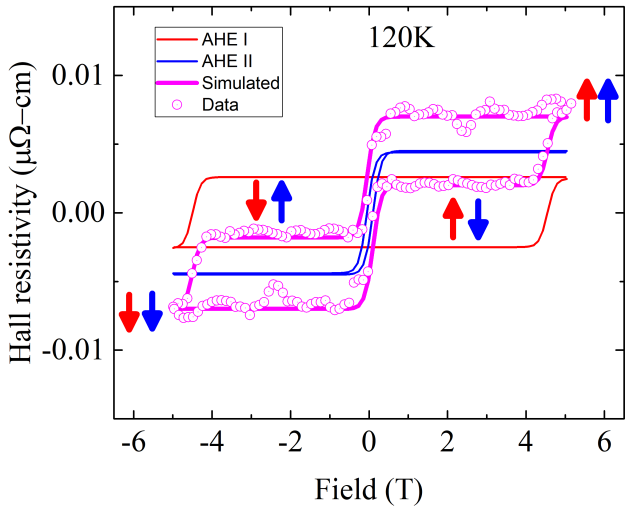

Figure 3.10. Hall resistivity sweeps vs the applied field at 120K for 21 u.c. SRO(001) film. Four distinct states, corresponding to the four magnetization configurations of the layers, can be observed.

ciated with the presence of multiple in-plane rotated structural domains. However, further analysis of this behavior is required. Here, we report the possibility of such a device in a single layer SRO film capped with a STO layer.

3.6. Summary

In summary, the presence of 90° in-plane rotated structural domains is established. We demonstrate that these domains are present in ultra-thin films as well. Both rotational and tilt distortions appear in ultrathin SRO(001) films (1 u.c. thickness) even when grown on a cubic perovskite substrate like STO. Such distortions reduce the symmetry of the surface and thus give rise to fractional diffraction spots in the $(\sqrt{2} \times \sqrt{2})$R45° LEED pattern. On the other hand, the octahedral rotational and tilt distortions in SRO thin films do not affect the interface layer structure of the STO substrate side, in contrast to CRO

and LSMO thin films.

The presence of crystallographic domains along with these octahedral distortions in ultra-thin films are important to understand the different transport and magnetic properties, such as the thickness dependent metal-insulator transition and the loss of ferromagnetism.

Both magnetoresistance and anomalous Hall studies showed sign of a second phase, with variations in coercivity suggesting multiple conduction channels. The temperature dependence of AHE can be simulated with a two component model with different coercivities and temperature dependence. Four magnetic and/or resistive states are present at 120K for 21 u.c. SRO(001) films, a requirement of an EHB device. We show that such a device could be realized with a single layer SRO film.

Chapter 4. The Effect of Crystallographic Orientation and Dimensional Confinement on the Properties of Strontium Ruthenate Thin Films

4.1. Introduction

In this chapter, we will perform comparative studies of structure and magneto-transport properties of ultrathin SRO films grown on [001] and [111] crystallographic orientation. High-index growth direction, particularly [111] direction shows a lot of promise for the future of oxide interfaces, for reasons discussed in Section 1.2.4.

Here, we will begin with the growth of high quality single crystalline SRO thin films on the (111) surface of the STO substrate and discuss their macroscopic structural characterization with XRD and STEM in section 4.2. An atomically resolved microscopic characterization of these films is performed with STEM and the details of the structural evolution with thickness layer is presented in section 4.3. A comparative study of crystalline symmetry dependent change in magnetic and transport properties of the SRO(111) film with respect to the SRO(001) films is presented in section 4.4. This study is done in relatively larger thickness ∼10 nm samples. Thickness-dependent structural and magneto-transport studies of ultrathin SRO films in [111] and [001] crystallographic directions are presented in section 4.5.1 and section 4.5.2 respectively. And finally in section 4.5.3 we will discuss the implications of the changing local symmetry (substrate orientation) and the dimensional confinement (reduced thickness) in the magnetic and transport behavior of SRO films.

4.2. Initial Growth and Structural Characterization of $SrRuO_3$(111) Films

The growth of SRO thin films along [111] crystallographic direction of STO has been getting moderate attention in the recent years[93, 94, 95, 96] driven by the theoretical prediction of stabilizing novel topological phases in bilayers [20, 21, 97]. The trigonal crystal field of the [111] direction, along with the sizable spin-orbit coupling is expected to open topologically protected energy gaps in an otherwise topologically trivial band structure. In addition, the electronic correlation inherent in SRO is further expected to enrich the topological properties.

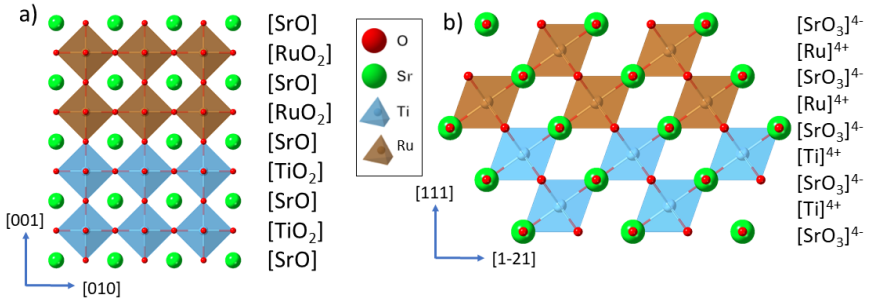

Figure 4.1. (a) Layer stacking of SRO on top of STO along the [001] direction. Neutral SrO and TiO_2 stack to form a stable surface. (b) Layer stacking of SRO on STO along the [111] direction showing charged planes.

Fig. 4.1 shows the layer stacking of the SRO film grown on top of STO substrate along both [001] and [111] directions. In SRO, the nominal valence of Ru is +4. Along [001] direction, the charge neutral SrO and RuO_2 planes stack on top of each other giving rise to a charge neutral surface. Along (111) crystallographic orientation, the stacking is of SrO_3^{4-} and Ru^{4+} layers. Each layer has an uncompensated charge of 4+ and 4-. The substrate, STO along [111] has similar stacking of layers with uncompensated charges of 4+ and 4-. Therefore, at the interface, there is no discontinuity of charges. However, the charge imbalance travels to the surface as shown in Fig. 4.1(b). This creates a surface that

is highly polar and unstable.

On the experimental side, the thermodynamics of growth along [111] direction is not well understood. The polar surface makes growth on this surface less favorable. A decreased growth rate and a tendency towards three dimensional island growth mode, caused possibly by a difference in the surface energy, has been reported for the SRO(111) thin films[98]. As we will see below, this surface polarity affects the thermodynamics of the initial growth in a unique way.

The thin film growth was achieved with Pulsed Laser Deposition (PLD). A Ti^{4+} terminated STO(111) substrate, prepared as described in section 2.1, was kept inside the high vacuum growth chamber. The base pressure of the chamber was kept at 1×10^{-8} Torr. The substrate was heated to 730°C with the help of resistive heaters. 100 mTorr partial pressure of Oxygen was maintained with a mixture of 99% O_2 and 1% O_3. A stoichiometric $SrRuO_3$ ceramic target was then ablated with a KrF Excimer laser (λ= 248 nm) with fluence 2 J/cm^2 and a frequency of 8 Hz. The growth process was monitored with a RHEED setup. The differential pumping station enables the operation of the RHEED gun at such high oxygen environment of the chamber. After growth, the films were cooled down slowly at 10 °C/min to room temperature while maintaining the oxygen pressure in the chamber.

Fig. 4.2 (a) shows the RHEED intensity monitoring of the initial growth of SRO films on STO(111) surface. The growth rate is 0.026 unit-cells/s, as obtained from the intensity oscillations of RHEED diffraction spots. Three different growth-mode regimes are observed . The initial growth regime denoted as regime I lasts upto $\approx$ 3 unit-cells. 2D layer-by-layer intensity oscillations are observed. For the next $\approx$ 8 unit-cells, regime II,

there is an intensity drop and the loss of RHEED oscillations. This regime is governed by a 3D island mode growth and the reduction of intensity suggests a roughening behavior. Such roughening behavior can be associated with the polar nature of the surface along the (111) planes. When an ionic material is grown on a polar surface, in the insulating regime (below 8 unit – cells), the electric potential increases[99]. The first three unit – cell film bears the increase in potential and shows a layer-by-layer growth before the roughness begins. This kind of uncompensated polarity in ultra – thin limit has been predicted in MgO and ZnO (111) ultra – thin films[100]. Roughening of the surface can suppress this increased potential which is observed in thickness larger than 3 unit – cells in regime II. As the coverage in increased, the film growth enters regime III, wherein the intensity is recovered. The 3D island mode is transformed to a 2D layer by layer mode after the $\sim$11 unit – cells film coverage. As we will see in section 4.5.2 and section 4.5.1, there is a thickness dependent metal insulator transition around 8 – 9 unit – cells. This nearly coincides with the transition from regime II to regime III. As the films become more metallic, the free charge carriers compensate for the electric field. Therefore, the roughness decreases and layer-by-layer growth resumes. A very similar behavior has been reported by Chang *et al*[101]. The RHEED diffraction pattern along the $[11\bar{2}]$ azimuth of the STO(111) substrate before growth, immediately after SRO growth at 730°C, and after cooling down to room temperature (RT) are shown in the inset of Fig. 4.2(a). The RHEED pattern after growth shows 1/3 and 2/3 fractional spots as indicated with red arrows. This is most likely a result of a $(\sqrt{3} \times \sqrt{3})$R30° surface reconstruction. We could not rotate the sample 90° to examine the $[10\bar{1}]$ azimuth because of experimental restriction. This reconstruction however goes away once the sample is cooled down at the high 100 mTorr P_O. Further in-

vestigation into the nature and cause of this reconstruction is necessary.

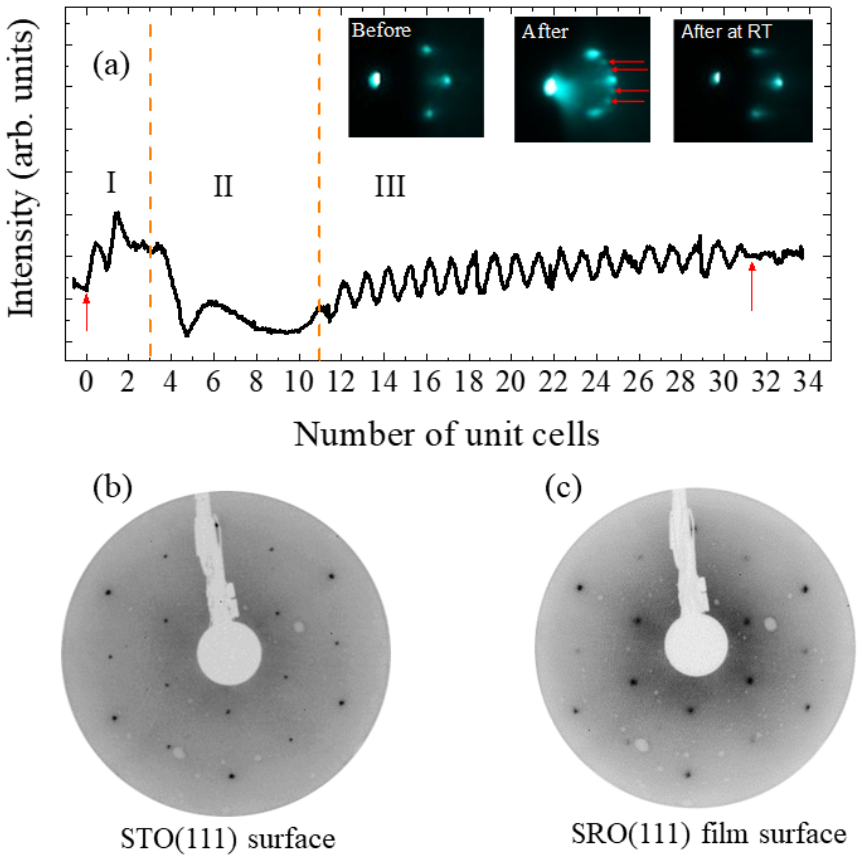

Figure 4.2. (a) Real time RHEED intensity oscillations during the growth of a 30 unit-cell SRO(111) film. RHEED diffraction pattern along the $[11\bar{2}]$ azimuth from the STO(111) surface before growth, immediately after the SRO film growth at 730°C, and from the SRO film cooled down to room temperature are shown in the inset in that order. (b) The LEED pattern of the substrate at 84 eV beam energy and (c) of the film taken at 78 eV beam energy show unreconstructed (1×1) pattern.

Fig. 4.2 (b-c) shows the LEED diffraction pattern of the bare STO(111) surface and a 30 unit-cell thick SRO(111) film. The STO(111) surface shows an unreconstructed (1×1) pattern of the triangular unit cell. A 30 unit-cell SRO(111) film grown at the above-mentioned optimal conditions also show a (1×1) unreconstructed unit cell. LEED investigation of lower thickness films, in the regimes I, II, are not attempted and could be interesting to explore in the future.

High resolution X-ray diffraction measurements were performed on a 56 unit–cell thick SRO(111) film for macroscopic structural characterization. Fig. 4.3 (a) shows $\omega - 2\theta$ coupled scan about the (111) peak of STO substrate. The substrate Bragg peak as well as the Laue fringes are observed. The film peak is slightly to the lower angle (2θ) side of the substrate peak and is overshadowed by the large STO(111) Bragg peak. The film contribution to the data can be fitted with to the intensity dependence of Laue's oscillations,

$$I(Q) = \frac{\sin^2(\frac{1}{2}QNc)}{\sin^2(\frac{1}{2}Qc)} \tag{4.1}$$

where, N is the number of unit-cells along the growth direction and Q is the reciprocal lattice vector, given by $4\pi \sin(\omega)/\lambda$, where ω is the angle of the incident x-rays with respect to the diffracting planes. c is the c-axis parameter. Both N and c can be estimated from the fit. The substrate peak is fitted to a pseudo-Voigt peak centered at the Bragg peak of the substrate. Both the substrate peak and the film contribution are shown in black dotted lines in Fig. 4.3 (a). The red solid line represents the sum of the contributions from the substrate and SRO film. N = 56 unit-cells and $c = 2.27$ Å were obtained from the fit. The c-axis parameter obtained is almost the same as the bulk value of SRO. We failed to see the lattice expansion of SRO film along the [111] direction due to compressive strain from the substrate with this procedure. Our assumption that the substrate and film contributions are additive might be to blame for such discrepancy[102]. We could not make independent accurate determination of the c-axis parameter from the film Bragg peak of the film as it is buried in the shoulder of the substrate peak. For a detailed lattice parameter calculation, we will rely on the atomically resolved structural characterization with scanning transmission electron microscopy (STEM) and is discussed in section 4.3 below.

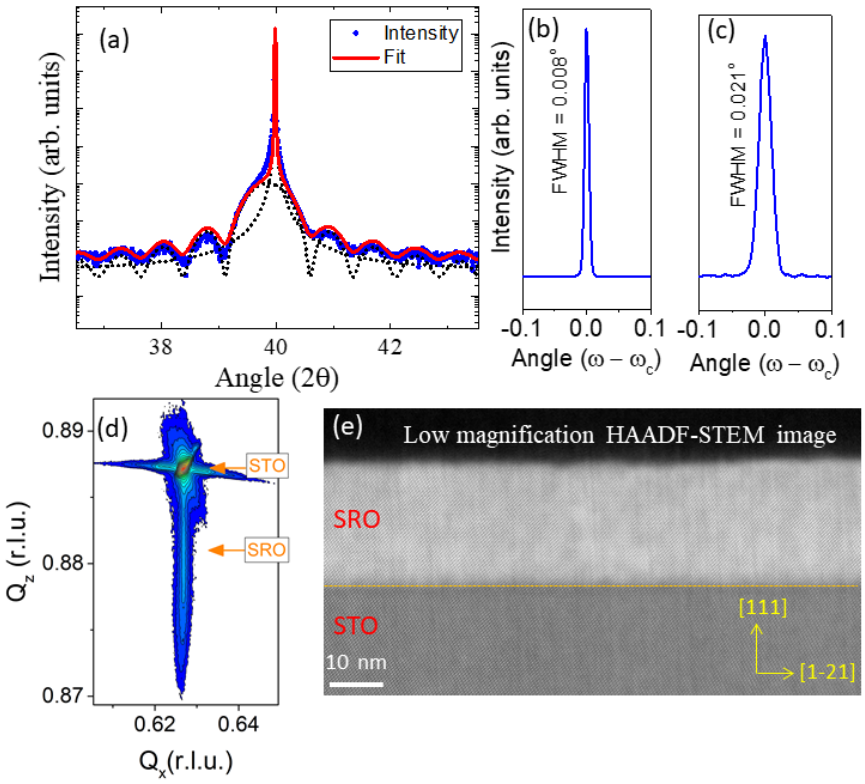

Figure 4.3. (a) ω - 2θ coupled X-ray diffraction scan of a ∼56 unit-cell thick SRO(111) film. The points are experimental data. The solid line is the result of fit by adding the film and substrate contributions. The substrate and film contributions are shown as dotted lines. (b) and (c) show rocking curves of the substrate and film peak, respectively. (d) Reciprocal Space Mapping about the (330) Bragg diffraction spot. The substrate and the film positions are marked. (e) A low resolution HAADF-STEM image of the 55 unit-cell SRO(111) film with beam in the [1-10] pseudo-cubic direction. The interface is indicated by the orange dashed line.

The rocking curves of the substrate and the film peak are shown in Fig. 4.3 (b) and (c). The Full-Width-at-Half-Maximum (FWHM) of the rocking curve of the substrate is $\sim 0.008°$ and that of the film peak is $\sim 0.02°$. In general, dislocations, mosaicity and curvature broadens the rocking curve of a thin film. The very narrow FWHM of these films is indication of the high degree of crystallinity. Reciprocal space map about the (330) asymmetric Bragg reflection peak, shown in Fig. 4.3 (d), shows that the film is strained in-plane to the substrate. Our XRD characterization establishes that the SRO(111) films

have high quality and are strained to the substrate for the whole thickness.

Fig. 4.3 (e) shows a low magnification HAADF-STEM image of a 55 unit-cell thick SRO(111) film taken in the [1-10] direction. There are no obvious structural defects like anti-phase or grain boundaries in the $\sim$ 100 nm thickness of a region of the sample, in sharp contrast to the multiple structural domain in the SRO(001) films discussed in Chapter 3. The interface is indicated with a yellow dashed line. We also can verify from the image that the STO substrate is Ti-terminated, and film growth begins with a SrO_3 layer.

In summary, we have optimized the growth of SRO(111) films with the structural quality in-par with those of SRO(001) films as evident from our XRD analysis. We observed that the polar (111) surface of STO affects the thermodynamics of growth in a unique way. The growth mode changes with the changing metallicity of our samples. Large scale STEM investigation reveal an apparent single domain structure without any obvious presence of 2D defects. A more detailed discussion of the atomically resolved microscopic structure is presented in the next section.

4.3. Atomically Resolved Structural Investigation with Scanning Transmission Electron Microscopy

The biaxial strain plane is at a completely different direction in the crystal when the films are grown in [111] direction (refer to Section 1.2.4). The nature of the strain relaxation, therefore, is expected to be different as well. Since the strain mismatch is minimal for SRO films grown on STO, we expect the effect of strain to be not too drastic. However, the deviation in rotations and tilts of the octahedra to accommodate the symmetry mismatch near the interface will be affected by the unique oxygen connectivity at the (111) interface. These modifications to the octahedral symmetry are expected to affect

the properties of ultrathin films. In this Section, we will present our investigation of the microscopic structure of the SRO(111) thin films. We have studied the atomically resolved structure near the interface using scanning transmission electron microscopy (STEM). By using a combination of high resolution HAADF and ABF imaging of the structure, we can monitor the oxygen octahedral symmetry variation across the thickness of the film.

A high-resolution HAADF STEM of a region of the sample taken along [1-10] direction is shown in Fig. 4.4. Cursory inspection of a high resolution HAADF image re-

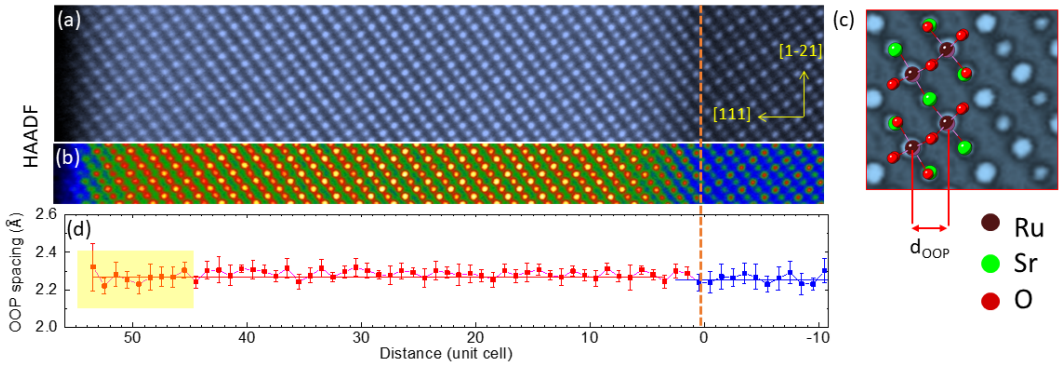

Figure 4.4. p
seudo-cubic direction](a) A high resolution HAADF-STEM image of the 55 uc SRO(111) film with beam in the [1$\bar{1}$0] pseudo-cubic direction. The interface is shown as an orange dashed line. (b) A different color contrast of the image in a.) reveals that the Ru – site intensity is reduced near the interface. (c) A zoom in of a region of the film. Overlapped is a model structure showing the structure and (d) The out of plane lattice spacing, d_{oop}, extracted from the HAADF image is plotted across the thickness of the sample.

veals the high quality of our thin films. We can quickly confirm the thickness estimation from STEM imaging is in agreement with XRD estimation from Section 4.2. The substrate termination is Ti, and the growth of the film begins with a SrO_3 layer. This is better observed by comparing the intensities across the thickness as visualized in Fig. 4.4 (b). The higher intensity on the SRO film side is that of Ru while it is that of Ti in the substrate side as the HAADF intensity is proportional to the atomic number. We also see

that the Ru-site intensity is slightly reduced near the interface, which is suggestive of some intermixture near the interface. We also observe a reduction in intensity near the surface. The volatile nature of Ru could be responsible. Fig. 4.4 (c) shows a zoom-in of the image. We can identify the atoms from the intensity comparison and superimpose a model structure as shown in Fig. 4.4 (c). The lattice parameter along the out-of-plane direction ([111] direction), d_{oop}, can be obtained from such an image and is plotted as a function of layer thickness in Fig. 4.4 (d). The bulk lattice parameter of STO and SRO are shown as blue and red solid lines respectively for comparison. The d_{oop} is extended compared to the bulk value for the most part, except for a region near the surface, shown shaded in yellow. The suppression of d_{oop} near the surface with reduced Ru intensity at the polar (111) surface suggests Ru vacancies could be a mechanism for surface energy minimization. The presence of Ru-vacancies are expected to increase the formal valence of Ru and thus decrease the ionic size. This will lead to a shorter Ru-O bond length and subsequently a smaller d_{oop}. This is in contrast to what we found the the Ru-vacancies at the interface of $SrRuO_3/Sr_2RuO_4$ in Section 5.4.

To quantify the oxygen octahedral rotations as a function of layer thickness, we performed STEM measurements in the $[11\bar{2}]$ direction. The relative position of the oxygen atoms can be resolved by ABF imaging in this direction. Fig. 4.5 (a) and (b) show the HAADF and ABF image in this direction. Fig. 4.5 (c) shows a zoomed-in Section of the ABF image and a model orthorhombic structure is superposed. We can identify the oxygen atom displacements and quantify them from the ABF images. Such oxygen displacements, δ_O, oscillate for orthorhombic crystal structure which is what we observe in Fig. 4.5 (d). 3-4 layers near the interface, shown shaded in yellow, have suppressed oxygen

octahedral distortions while the rest of the film is relaxed to values very close to the bulk crystal. The bulk lattice parameters of SRO and STO are shown as dashed lines. Such regions of intermediate Ru-O-Ru bond angles are required for geometrical continuity of the structure between two systems with different octahedral symmetry. We also observed 4-5 layers with intermediate structure near the interface in SRO(001) films as discussed in Section 3.4. No significant affect of the (111) interface in this near-interface structure is observed.

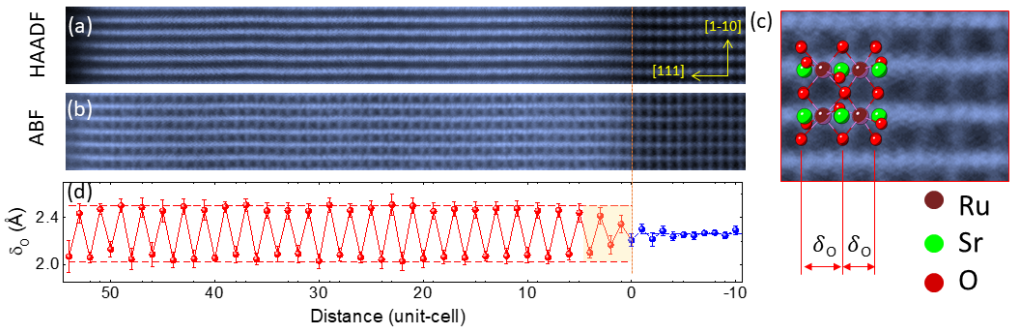

Figure 4.5. (a) HAADF and (b) ABF image of the 55 uc SRO(111) film with beam in the [11$\bar{2}$] pseudo-cubic direction. The interface is shown as an orange dashed line (c) A zoom in of a region of the film of the ABF image showing the oxygen atom positions. Overlapped is a model structure showing the structure. The relative oxygen atom displacements as shown are measured and plotted as a function of layer thickness in (d). The bulk parameters are shown as dashed lines.

In summary, we have established the high quality of SRO(111) film with a sharp interface from STEM measurements. The film is strained to the substrate in-plane while the out-of-plane lattice is extended in accordance with the compressive strain from the substrate. STEM also reveals bulk-like values for the out-of-plane lattice parameter for a few layers near the surface, where we observed reduced Ru-site intensity. The larger occurrence of localized Ru-vacancies at the interface and surfaces can be a significant source of discrepancy in properties especially in the ultrathin films. This warrants a thickness de-

pendent structure property investigation of SRO films. We will attempt a thickness dependent structure study coupled with the magnetic and transport properties measurements in Sections 4.5.1 and 4.5.2. The oxygen octahedral rotations of the film are bulk-like, except for 2-3 layers near the interface, where we observed reduced rotations. No obvious deviations of the TiO_6 octahedra on the substrate side is observed.

4.4. Symmetry Dependent Changes in Magnetic and Transport Behavior of $SrRuO_3$ Films

As we have discussed in Section 1.1, in a localized picture, the strong crystal field at the octahedral site splits the Ru 4d bands of the Ru^{4+} ions into the e_g and t_{2g} levels, leading to a low spin configuration with S =1. The orbital moments are quenched according to theoretical studies[103, 104, 105] as well as x-ray magnetic circular dichroism (XMCD) study[106]. Studies of magnetic properties of 111 oriented SRO films have produced conflicting results. Grutter et al observed magnetization values in the range of (2.22 – 3.4) μ_B/Ru ion. They suggested the enhancement of the Ru moment is due to the stabilization of the high-spin configuration of Ru^{4+} ion in the trigonal lattice[93, 107]. Surprisingly, they also reported an unquenched orbital moment of 0.32 μ_B/Ru ion in their XMCD study. More recent studies have failed to reproduce and/or support the observation[94, 108]. A recent XMCD spectroscopy study found that the orbital moments are almost quenched and the spin moment close to the value expected for the low spin state[109]. Here, we will discuss the magnetic and transport properties of two representative thin films. We will choose a 25 u.c. SRO(001) film, and a 50 u.c. SRO(111). As will see, two unit-cells of SRO(111), i.e. two Ru layers, are required to regain the in-plane Ru-O-Ru connectivity which is lost for a single layer SRO(111) (see Section 4.5.3). For

this reason, double thickness in layers of SRO(111) is taken for comparison of properties. Fig. 4.6 shows a plot of reduced magnetization (M(T)/M(5K)) vs reduced temperature (T/T_C) for the two samples. The SRO films were first cooled down in a magnetic field of 1 Tesla, applied perpendicular the the film plane. The magnetization measurements were performed while warming up in the presence of a magnetic field of 20 Oe. Very different low temperature behaviors can be quickly noticed. Magnetic excitations are thermally induced as the temperature is increased from T = 0. Both collective spin-wave excitations and single particle (Stoner) excitations can cause the suppression of magnetization. The thermal suppression of magnetization due to Bloch law is given by $M(T)/M_0 = 1 - AT^{3/2}$. The coefficient, $A = 0.059/S(k_B/2JS)^{3/2}$ for a simple cubic magnetic lattice, where S is the total spin of Ru^{4+} (S=1), and J is the exchange energy. SRO(001) in Fig. 4.6 and inset (a) shows the low temperature fit with Bloch law. Very good agreement with the Bloch $T^{3/2}$ law is obtained. The estimated exchange energy of ~ 15 k_BK obtained is smaller than the reported value of 26.33 k_BK for thicker ($\sim$ 1000 Å of Klein *et al* [110]. Our attempt to fit the low temperature magnetization of SRO(111) samples did not produce acceptable results. However, when fitted to a T^2 behavior in Fig. 4.6 (see also inset (b)) produces a reasonable agreement. The presence of the T^2 term for SRO films was discussed by Klein *et al* in thin films SRO(001) but only as a correction to the dominant $T^{1.5}$ Bloch law behavior. In single crystals, a similar T^2 behavior is observed when measured with field along the easy axis, i.e. along the $[110]_o$ of the orthorhombic unit cell [111]. A significantly suppressed spin-wave excitations in SRO(111) films along the direction perpendicular to the plane causes the T^2 dependence in M(T) at low temperatures in SRO(111) films.

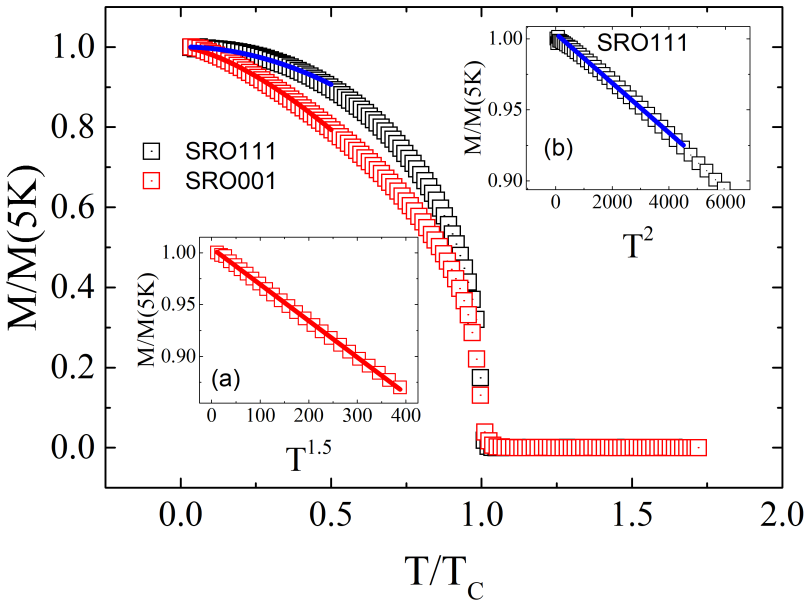

Figure 4.6. The reduced magnetization (M(T)/M(5K)) of a 25 u.c. SRO(001) film and a 50 u.c. SRO(111) film as a function of reduced temperature (T/T_C). The low temperature data are fitted to $T^{1.5}$ for SRO(001) while those of SRO(111) are fitted to T^2. Inset: (a) The linear behavior with M vs $T^{1.5}$ for SRO(001) and (b) M vs T^2 for SRO(111).

We now proceed to analyze the critical behavior near T_C in these two samples. Fig. 4.7 (a) and (b) show the Magnetization measurements of the (001) and (111) oriented SRO films. The magnetic field was applied perpendicular to the plane of the film. The easy axis in both 001 and 111 oriented films is generally reported to be in the out-of-plane direction of the film[93, 94, 110]. A slight tilt away from the perpendicular direction of the easy axis is expected for both the films. With the assumption that the magnetic anisotropy affects the two film directions in a similar fashion, we try to understand the magnetization data. The behavior near the transition temperature is fitted to the scaling law, $M = a(T_C - T)^{\beta}$, where M is the spontaneous magnetization and β is the critical exponent associated with the spin dimensionality. The parameter, a is related to the magnetic susceptibility. The value of $\beta = 0.358$ is obtained for SRO(001) films whereas, a

value of $\beta = 0.325$ is obtained for SRO(111) films. The theoretical value of β for an Ising – type ferromagnet is 0.326, while that for a Heisenberg-type ferromagnet is 0.36[112]. Our fit suggests that the spin-dimensionality of SRO(001) films is consistent with Heisenberg – type ferromagnet, whereas that of SRO(111) films is reduced and consistent with Ising – type ferromagnet. In addition to the reduction in the spin-dimensionality, we also observed an enhancement in Curie temperature for the SRO(111) films in agreement with previous reports[93, 94, 96]. An enhancement of about 6 K is observed.

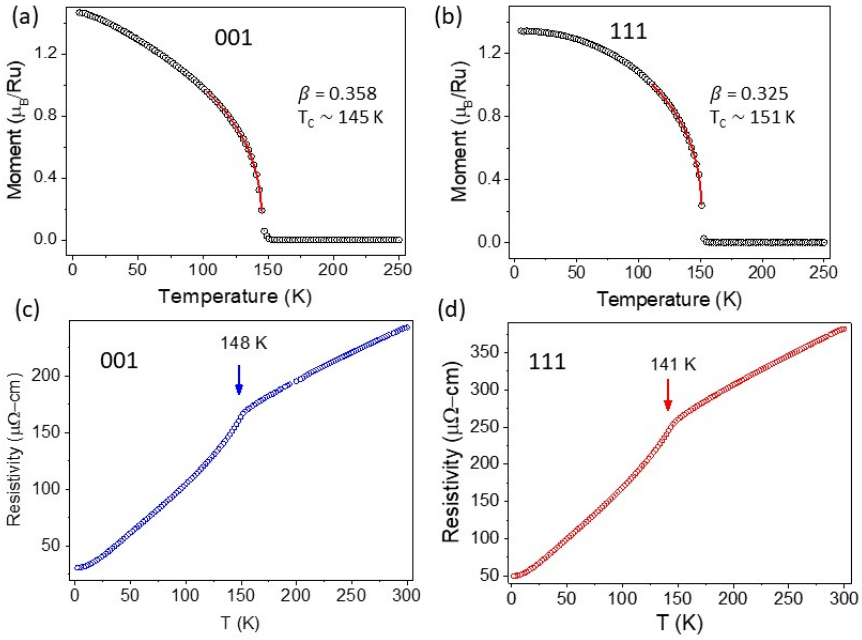

Figure 4.7. a
nd [111] directions]Temperature dependence of magnetization of (a) 25 u.c. SRO(001) film and (b) 50 u.c. SRO(111) film measured while warming in 20 Oe field applied perpendicular to the sample. The data is fitted with $M = a(T_C - T)^{\beta}$. The fit is shown in red. The temperature dependence of resistivity of (c) 25 u.c. SRO(001) film and (d) 50 u.c. SRO(111) film. The arrows point to the position of the peak in dρ/dT near the transition temperature.

The temperature dependence of resistivity of the SRO(001) and SRO(111) films, measured with a standard four probe method, are plotted in Fig. 4.7 (c) and (d) respec-

tively. The characteristics of the resistivity behavior of SRO is the anomaly near T_C due to a drop in resistivity below T_C. We observe a "kink" in resistivity in both SRO(001) and SRO(111) films. The position of this anomaly is identified from the peak in the derivative curve, $d\rho/dT$ and is shown with arrows. While the position of such anomaly is slightly below the T_C obtained from MT, the enhancement of about 6 K in the SRO(111) is observed here as well. SRO(111) films show smaller residual resistivity overall, $\rho_0 \approx 31\ \mu\Omega - cm$ as compared to the SRO(001) films with $\rho_0 \approx 50\ \mu\Omega - cm$. Both films show a residual resistivity ratio (RRR), defined as the ratio of resistivity at 300 K to the resistivity at 2K (ρ_{300K}/ρ_{2K}), of about 7.7. The lower RRR value has been linked to non-stoichiometry related to the Ru vacancies[45]. Very similar RRR is obtained in the two films, which suggests similar level of disorder of the two films. We will now proceed to analyze the low temperature resistivity behavior of both these films.

Temperature dependence of resistivity is usually expressed in the form of

$$\rho = \rho_0 + A_\alpha T^\alpha \tag{4.2}$$

The value of the exponent, α provides insight into the dominant scattering mechanism. Plotting ρ vs T^α for trial values of α to produce a linear behavior is often unreliable. Rather plotting $\mathrm{d}\rho/\mathrm{d}T^n$ with trial values of α until the data appears constant is considered less subjective[113]. Fig. 4.8 (a-b) show temperature dependence of $d\rho/dT$ for SRO(001) and SRO(111) respectively. The peak in $d\rho/dT$ is a general feature of metallic ferromagnets. The low temperature part of $d\rho/dT$ vs T, T $\leq$20 K, can be well fitted with a straight line passing through origin with a positive slope, characteristics of a Fermi-liquid ($\rho \sim \mathrm{T}^2$) behavior for both SRO(001) and SRO(111) films. This temperature is

defined as the Fermi-Liquid temperature, $T_F \approx 20$ K for further discussion of these two samples. In the temperature range, 35 K $\leq$ T $\leq$ 75 K, $d\rho/dT$ shows a linear behavior with a vanishing slope in both SRO(001) and SRO(111)films. Various trials of $d\rho/dT^{\alpha}$, with trial values of α, show that $\alpha = 1$ produces the most horizontal (constant i.e. $\not\propto$ T) data in the temperature range. This suggests that the resistivity scales linearly in the said temperature range in both SRO(001) and SRO(111) films. Herranz et al[114] have shown that below T_C, the resistivity scales linearly on the samples with least disorder whereas, it becomes increasingly non-linear for increasing disorder. Various values of α have been reported that range between 1 and 2, and is also suggested to be a signature of non-Fermi liquid behavior of SRO[35, 115]. We will discuss the temperature dependence of resistivity, in the 35 K $\leq$ T $\leq$ 75 K temperature range, for a series of various thickness SRO(111) samples in Section 4.5.1.

Fig. 4.8 (c-d) shows field dependent behavior of magnetoresistance at various temperature of SRO(001) and SRO(111) films, respectively. At high temperature (T=50K) , both SRO(001) and SRO(111) show a linear negative magnetoresistance. This negative MR is because of the suppression of spin-dependent scattering due to the application of field. A butterfly hysteresis loop is also observed in both these samples. The overall magnitude of the magnetoresistance is higher for SRO(001) films, while the positive MR segment near zero field (the wing of the butterfly) is higher for SRO(111) films. The peak in the MR hysteresis corresponds to the coercive field, H_C and the point of overlap between the forward and backward sweeps of the field corresponds to the saturation field, H_S. However, this definition can be misleading because SRO(111) at lower temperatures, below T_F, has another large positive contribution.

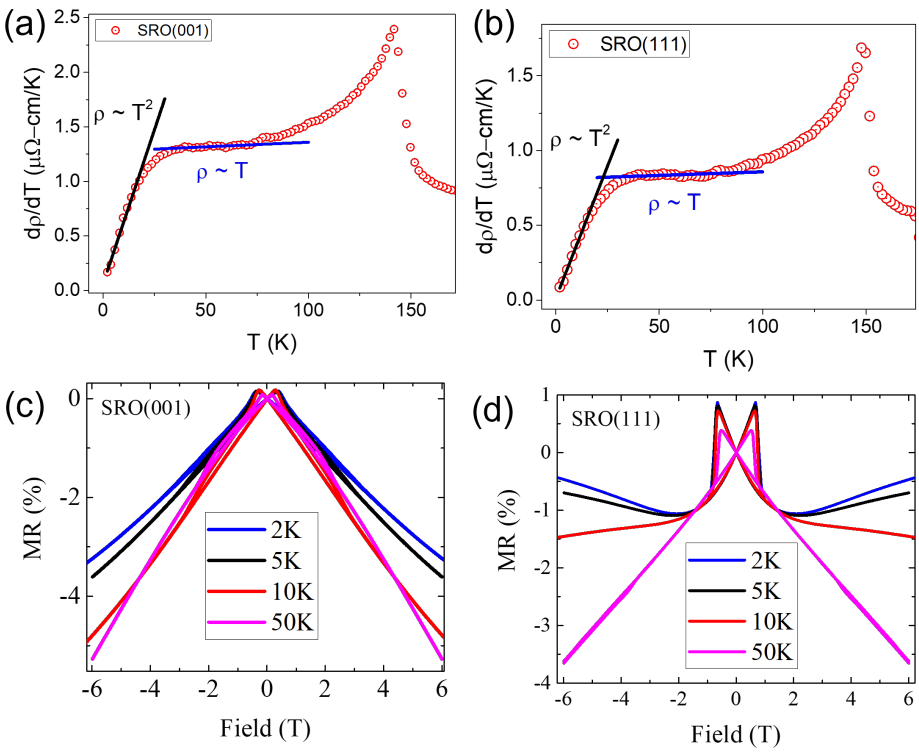

Figure 4.8. $d\rho/dT$ as a function of temperature shows a peak around T_C. The Fermi-liquid, $\rho \sim T^2$, behavior at T $\leq$ 20 K and $\rho \sim$ T, behavior in the range 35 K $\leq$ T $\leq$ 75 K is shown by fitting for (a)SRO(001) film and (b)SRO(111) film. Magnetic field dependence of magnetoresistance (MR) for various temperatures for (c) SRO (001) and (d) SRO(111) film are shown.

5 K MR data shows the upturn around 2.26 T field and moves to lower field (2.1 T) for 2K data. The high field linear positive MR for T $\leq$ 5 K showed no sign of saturation up to the fields measured (10 T).Such a positive contribution to transverse magnetoresistance was first reported by Izumi *et al*[60]. It was argued that the Lorentz force contribution to the magnetoresistance is not enough to account for such a large increase in resistance. Linear positive MR has also been reported recently in much thicker ($\geq$ 63 nm) SRO(001) films with a much larger RRR ($\sim$ 83) along with other properties such as light cyclotron mass from quantum oscillations, high quantum mobility [28]. These features along with the anisotropic nature of magnetoresistance, i.e. negative magnetoresis-

tance when the applied field, B is parallel to the current, has been interpreted as signatures of Weyl fermions in SRO. Here, we observe such a linear positive MR in the SRO (111) films with a much lower RRR (∼7) and a much smaller thickness (∼12 nm) on PLD grown films. No such positive MR is observed in the low T regime in SRO(001) films.

To summarize, we observed an enhancement of T_C on SRO films grown along [111] direction of the STO substrate in both magnetization and transport measurements. The thermal suppression of magnetization at low temperatures in SRO(001) is dominated by spin-wave excitations while that of SRO(111) is dominated by Stoner excitations. From our fitting of critical behavior near T_C, we observed a reduction in the critical parameter β, which is a signature of reduction of spin-dimensionality in SRO(111). And finally, a linear positive MR at low temperatures in SRO(111) is observed which did not show any saturation upto 10 T.

4.5. Substrate Orientation Dependence on the Properties of Ultrathin $SrRuO_3$ Films

To explore the effect of dimensionality in the [111] orientation of the substrate, we performed a thickness dependent study of SRO(111) films. As we have discussed in Section 1.2.4, the trigonal crystal field of (111) surface is expected to affect the electronic properties of SRO in a unique way. We expect the effect to be pronounced in reduced dimensions.

4.5.1. Thickness dependent properties of $SrRuO_3$(111) films

We grew a series of SRO(111) samples with thickness (6 - 18 u.c.) with the purpose of studying a thickness dependent structure and property evolution. All the samples were capped with 2 u.c. of crystalline STO to protect the surface for *ex-situ* mea-

surements. Below we will explore the magnetic and magneto-transport properties of these films.

Thickness dependent magnetic properties of $SrRuO_3$(111) films

Fig. 4.9 (a) shows temperature dependent change in magnetization, M(T) plot of various thickness SRO(111) samples. A typical ferromagnetic to paramagnetic transition is observed across the transition temperature (T_C) which varies significantly with thickness. We saw that at sufficiently small thicknesses (< 6 u.c.), ferromagnetism is suppressed. 6 u.c. film is at the verge of being magnetic. It shows a finite moment in M(T) measurement and also a tiny hysteretic loop in field dependent magnetization measurement (M-H) as can be seen in Fig. 4.9 (b).

We also saw a significant increase in saturation moment (M_S) in SRO(111) films with decreasing thickness, especially below 10 u.c. We see that the M_S exceeds the low spin limit of 2 μ_B/Ru as well. This behavior needs a more careful examination. The FM signal gradually decreases with decreasing thickness and the M-H data is usually buried under a large diamagnetic signal from the substrate that varies linearly with magnetic field. We obtain the M(H) by subtracting the a linear fit from the high field portion of the data. The error becomes larger when the signal to subtract becomes increasingly smaller compared to the background from the substrate, which makes the M_S value for the lowest thickness less reliable. A more accurate way to measure M_S would be to measure M-T with increasing magnetic field until the maximum moment at low temperature saturates. Therefore, we will not comment on the magnitude of M_S obtained for the ultrathin samples.

The transition temperature, T_C was estimated from the position of the dip in $d\left(\frac{M(T)}{M(5K)}\right)/dT$ curve as shown in Fig. 4.9 (c). The peak positions, T_C are indiced in the plot with dot symbol. Fig. 4.9 (d) shows thickness evolution of the transition temperature. There is a steep rise starting at 8 u.c. followed by a rather slow rise to saturation. The largest thickness of the samples measured was 56 u.c. which had a T_C of about 152 K.

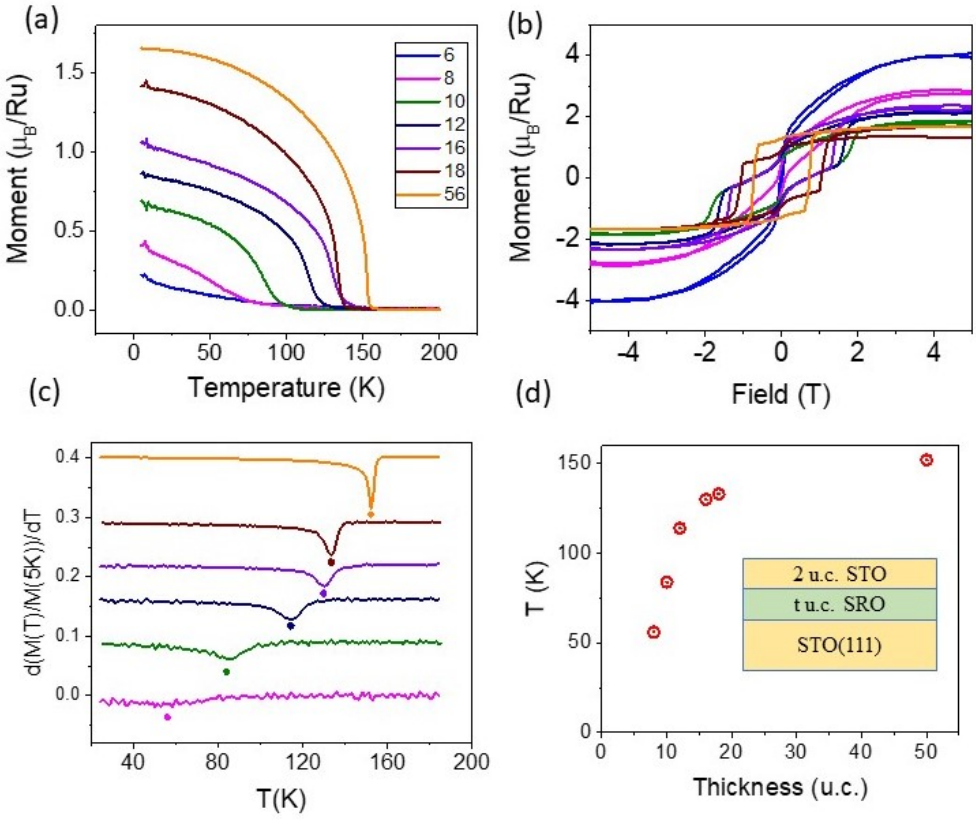

Figure 4.9. (a) Temperature dependence of magnetization of SRO(111) films. (b) Field dependent MH loops at 5K. (c) $d\left(\frac{M(T)}{M(5K)}\right)/dT$ plotted as a function of temperature. The peak positions are denoted by solid dots. and (d) T_C obtained from peaks in the curves in (c) are plotted with thickness.

Thickness dependent magneto-transport properties of $SrRuO_3$(111) films

Fig. 4.10 summarizes our thickness dependent transport measurements of SRO(111) films. The resistivities are plotted on the y-axis in log scale for accommodation of all the data and clearer comparison. We observe a thickness dependent metal-insulator

transition (MIT)that occur at 8 u.c. thickness, which shows metallic behavior at room temperature. As the temperature is lowered, an upturn appears around $T_{min} \sim 168$ K, after which the resistivity, increases fast. Samples above 8 u.c. thickness show metallic behavior, while the low temperature upturn, T_{min} moves to lower temperature with increasing thickness. Samples larger than 8 u.c. in thickness also show an anomaly near the ferromagnetic transition, which is better observed in $d\rho/dT$ and are shown in Fig. 4.10 (b) for all thickness samples. The position of the peak in $d\rho/dT$ are indicated by arrows and correspond to the ferromagnetic transition temperature. With increasing thickness, we observe an increase in metallicity as well as the peak in $d\rho/dT$ moves towards higher temperature, signaling and increment in ferromagnetic transition temperature, T_C. Fig. 4.10 (c) shows the resistivity data for various thickness normalized to their resistivity at 300 K. The low temperature resistivity behavior of various thickness films shows a few differences. The residual resistivity of the samples increases with decreasing thickness. The residual resistivity ratio (RRR) follows a monotonic thickness dependence and is shown in the inset in Fig. 4.10 (c). At the extremely low thickness regime, the residual resistance measurement is complicated by the presence of T_{min}. We will discuss the characteristics of insulating samples and those on the verge of being insulating in next Section.

Thickness dependent low temperature dependence of resistivity in SRO(111) films

The resistivity is usually described by the power law (4.2), $\rho = \rho_0 + A_\alpha T^\alpha$. In this Section, we will try to analyze the correct exponent α for the various thickness SRO(111) samples. To do so, we employ the "no fit" method. The derivative of resistivity $d\rho/dT^\alpha$ is plotted vs T, in the temperature range of 30K - 80K, where α is varied until the data

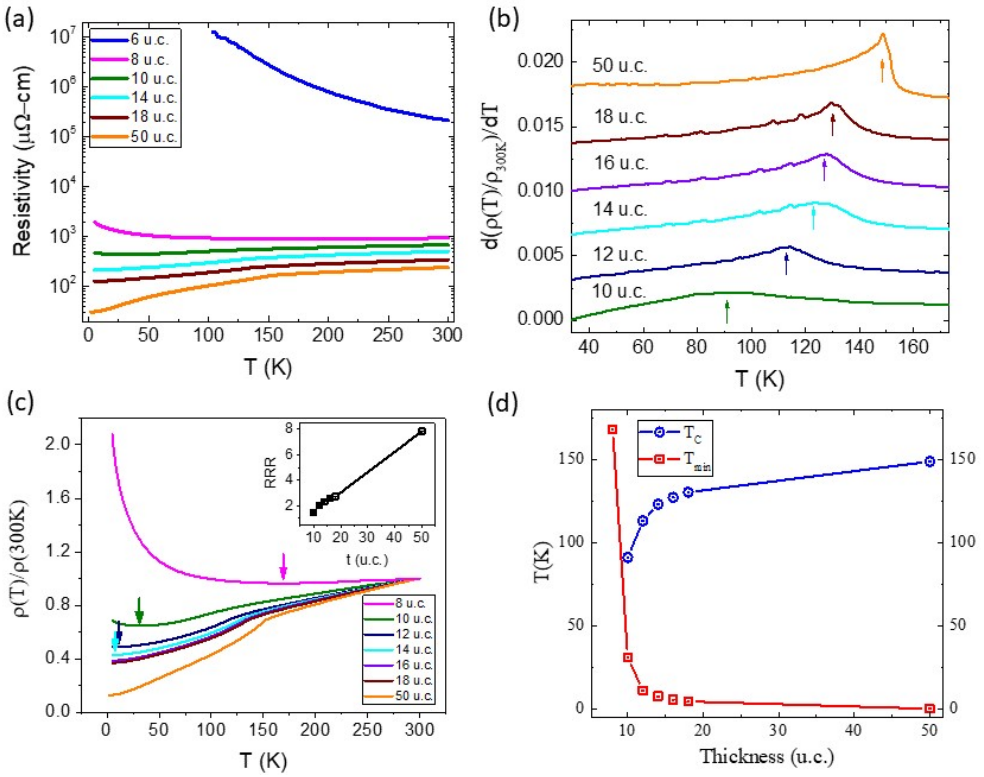

Figure 4.10. (a) Temperature dependence of resistivity of SRO(111) films. (b) $d\left(\frac{\rho(T)}{\rho(300K)}\right)/dT$ plotted as a function of temperature. The peaks positions are identified by the arrow. (c) $\rho(T)/\rho(300K)$ plotted as a function of temperature shows an increase of residual resistivity ratio (RRR) of the films with thickness. The upturn at low temperatures are denoted by arrows. The inset shows the RRR of samples plotted with thickness. (d) T_C obtained from peaks in the curves in (b) and the position of T_{min} are plotted as a function of thickness of SRO(111) films.

appears constant. A $T^{1.5}$ dependence of resistivity has been reported for SRO films and is oftern interpreted as a signature of non-Fermi liquid behavior. Such a plot is shown for a few representative thickness in Fig. 4.11. The red data plot corresponds to value of α that agrees best. The temperature range in which the the data agrees with the value of α is shown by red arrows. As we see from the plot, the value of α obtained increases with decreasing thickness.

In Fig. 4.12, we plot the α values of the SRO(111) films vs the corresponding value of T_{min}. We can clearly see that α increases with increasing values of T_{min}. The larger

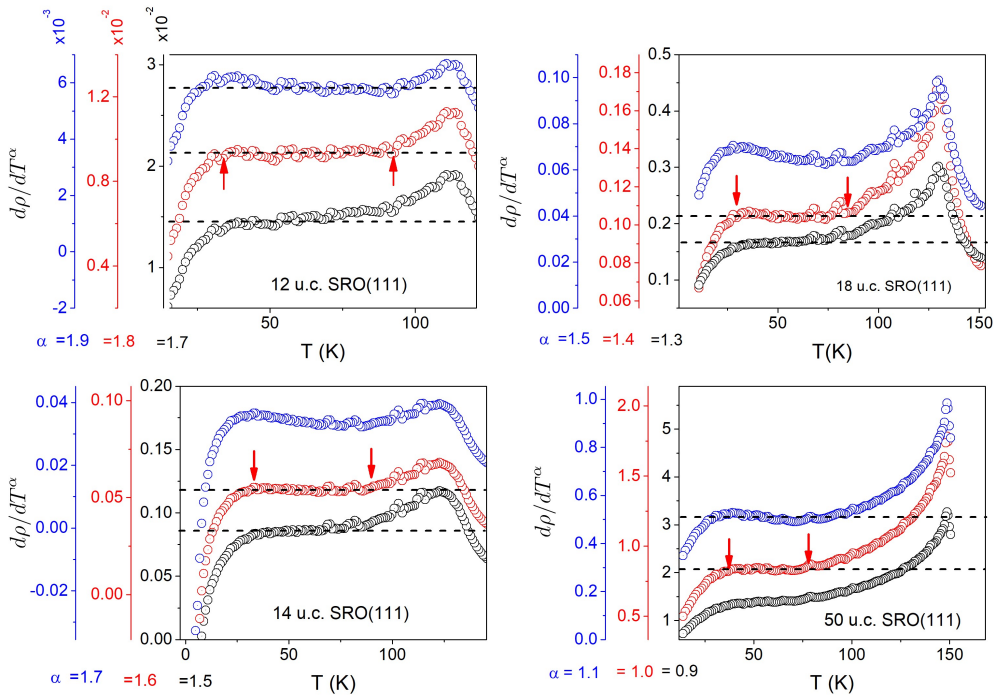

Figure 4.11. dρ/dT$^{\alpha}$ vs T of 12 u.c., 14 u.c., 18 u.c., and 50 u.c. SRO(111) films plotted for various trial values of α. The most horizontal looking plot is shown in red and the arrows indicate the temperature region in which dρ/dT$^{\alpha}$ is horizontal.

values of T_{min} are indication of higher disorder in SRO. So, the value of α scales almost linearly with disorder and approaches $\alpha \rightarrow 1$ for the samples with lowest disorder. A very similar linear trend of the exponent α with disorder was observed in SRO(001) samples, wherein disorder was introduced with Ar^{+} ion bombardment[114]. We thus see that disorder in ultrathin SRO(111) films affect the resistivity behavior at low temperatures in a fundamental way in these films.

In the next discussion, we will divide the samples into three categories and discuss them separately. The lowest thickness sample, 6 u.c. SRO(111) is insulating in the temperature range of (5K - 300K) measured. The samples in the thickness range 8 - 14 u.c show low temperature correction to resistivity, apparent with an upturn in resistivity. Samples with thickness 16 u.c. and above are metallic in the studied temperature range.

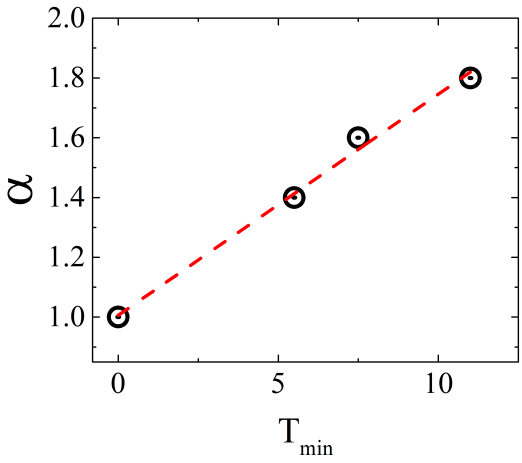

Figure 4.12. Correlation between the position of the resistivity upturn, T_{min} and the value of the exponent, α. The dashed line is a quide to the eye.

Transport in the Insulating Regime

The resistance of the lowest thickness sample, 6 u.c. SRO(111) were measured in the temperature range (107 K – 300 K). The low temperature resistance could not be measured because of the high resistance and the instrument limitations.

Insulating behavior in the strongly localized systems can be described in the variable range hopping (VRH) model. The temperature dependence of conductivity in this model is described as[116]

$$\sigma = \sigma_0 \, exp\left[-\left(\frac{T_0}{T}\right)^{\nu}\right] \tag{4.3}$$

where T_0 depends on the density of localized states at the Fermi level and the falloff rate of the wave functions associated with these states, σ is the conductance, the exponent ν=1/(d+1), for d-dimensional system. In this regime, the electrons hop between localized states at low temperatures.

We attempted to fit, in the 6 u.c. insulating SRO(111) sample, $\ln\sigma \propto 1/T^{\nu}$ for ν = 1,2,3,4 etc. $\nu = 1$ represents the thermally activated hopping conduction. $\nu = 1/3$ is

the Mott's VRH in two dimensions. In this scenario, at low temperatures electrons fall into potential well due to disorder and they move to adjacent wells by tunneling[117]. Coulomb interactions between hopping sites are ignored, thus creating a constant density of states near the Fermi level. When the coulomb interactions are taken into considerations, the carriers near the Fermi level will reorganize to minimize the total energy. Efros and Shklovskii showed that this will lead to suppression of density of states near Fermi energy and $\nu = 1/2$ is more appropriate in all dimensions[118]. Fig. 4.13 shows

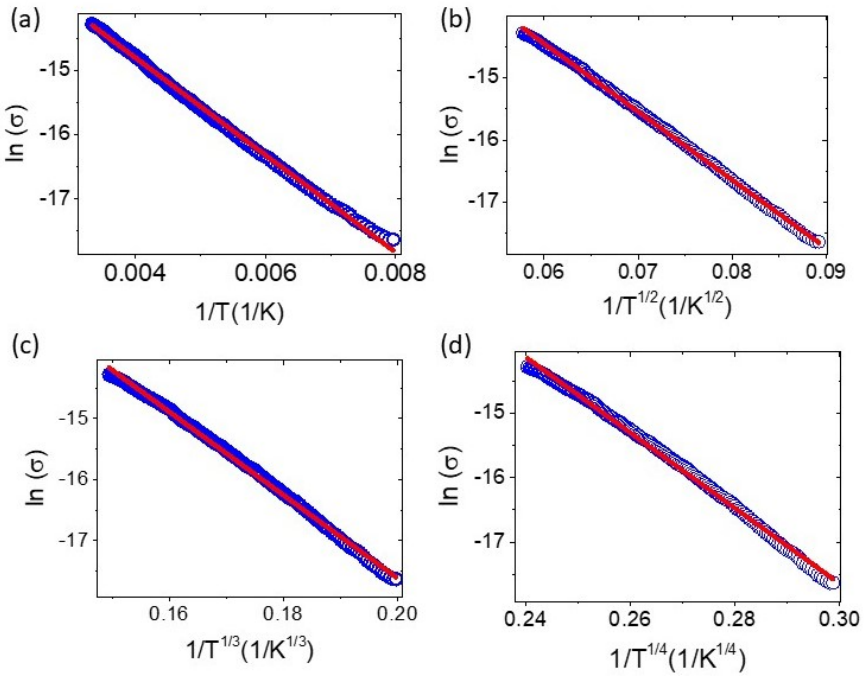

Figure 4.13. (a) Fitting of the conductivity of the 6 u.c. SRO(111) film with different test models. (a) The thermal activation model $\ln \sigma \sim \frac{1}{T}$. (b) the Efros and Shklovskii 2D VRH $\ln \sigma \sim \frac{1}{T^{1/2}}$ (c) the 2D VRH model $\ln \sigma \sim \frac{1}{T^{1/3}}$ and (d) the 3D VRH model $\ln \sigma \sim \frac{1}{T^{1/4}}$

the plot of $\ln \sigma$ vs $T^{-\nu}$ plots with various values of ν. The Arrhenius plot in Fig. 4.13 (a) begins to show some curvature at the lowest temperatures (∼110K) which signals a possibly larger deviation at even lower temperatures. Table 4.1 shows the residual sum of squares and the R-square values for the various values of ν. ν=1/2 shows the best fit with

largest R-Square values and lowest Residual sum of squares. This implies the Efros and Shklovskii (ES) type variable range hopping as the mechanism for the insulating behavior. This would imply a dimensional crossover from a 3D metallic conductivity to a 2D variable range hopping insulating phase. However, due to limited temperature range of the data, it is difficult to make accurate determination of the exact nature of this insulating phase, since the VRH is expected to be more prominent at lower temperatures. A good fit at higher temperatures for 2D VRH indicates towards the possibility that VRH could be the main mechanism throughout the temperature regime. The VRH at high temperatures is still possible due to polaron assisted hopping[119].

Table 4.1. Fitting parameter for the 6 u.c. SRO(111)

ν	Residual Sum of Squares	R-Square
1	0.2147	0.99868
1/2	0.1284	0.99921
1/3	0.33347	0.99794
1/4	0.47965	0.99704

Transport in the Intermediate thickness regime

For samples with thickness larger than 6 u.c., we observe a temperature dependent metal to insulator transition. The position of this transition, denoted as Tmin, is a function of thickness. With increasing thickness, T_{min} moves to lower temperature until it vanishes up to the lowest temperature measured. This behavior is indication of a weak localization (WL) induced reduction of conductance at lower temperature. In a disordered electronic system, the motion of electrons is diffusive rather than ballistic. Diffusive motion is controlled by random walk due to scattering from impurities. Weak localization effects are originated by the constructive interference of the backscattered carrier wavefunctions

from a random distribution of scattering centers. The relevant length scales in WL are the Fermi wavelength (λ_F), and the inelastic mean free path (l_i). In order for the constructive interference to occur, the wave coherence needs to be maintained for long distances. During the inelastic scattering, in the form of electron-electron, electron-phonon, or electron-magnon interactions, the wave coherence is lost. Therefore, WL effects only appear in low temperatures in order for the inelastic mean free path to be long enough. As the temperature is lowered below T_{min}, the WL effects are reinforced which leads to an enhancement of resistivity. Above T_{min}, the wave coherence is lost, and the normal metallic behavior is established. In lower dimensions, it is much more likely to find self-intersecting paths compared to the higher dimensional case, thus, the weak localization effect is stronger in 1D and 2D. In two dimensions, the temperature dependence of conductivity due to weak localization is given by[120],

$$\sigma = \sigma_0 + p\frac{e^2}{\pi h}\ln\frac{T}{T_0} \tag{4.4}$$

where, σ_0 is the Drude conductivity and p, the temperature exponent of the inelastic scattering length, $l_i \sim T^{-\frac{p}{2}}$. If the main inelastic relaxation mechanism is due to electron-electron scattering, $p = 1$. If the main relaxation mechanism is due to inelastic electron-phonon scattering, $p = 3$ and $p = 1/2$ for contributions from spin-waves in 2D[121].

Fig. 4.14 shows the sheet conductance in the units of $\left(\frac{e^2}{\pi h}\right)$ plotted as a function of ln(T). In the 2D weak localization picture, we expect a linear behavior at low temperatures. The 10 u.c. SRO(111) sample shows a linear behavior in the temperature range (5 K – 22 K). The slope of the linear fit gives the value of p - parameter ≈ 1.49. The 12 u.c. sample does not have enough data at the lower temperature side to warrant a linear

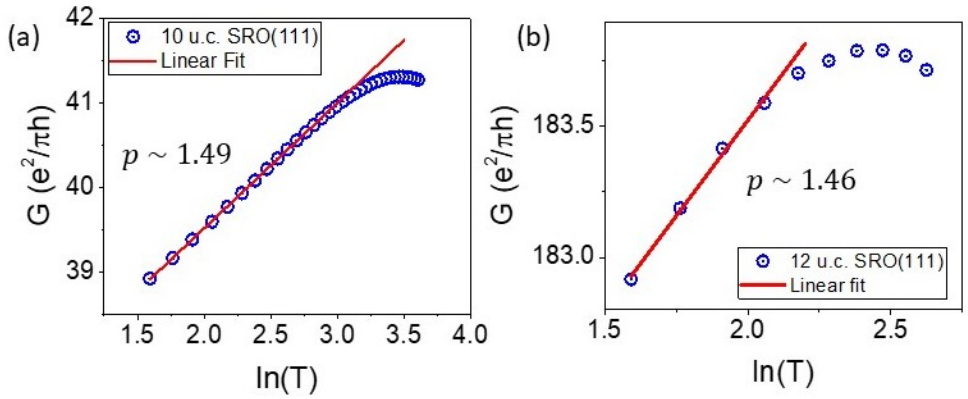

Figure 4.14. Dimensionless sheet conductance plotted as function of ln(T) along with attempted linear fit at lower temperatures for (a) 10 u.c. SRO(111) (b) 12 u.c. SRO(111) films.

behavior. However, it most likely is linear at lower temperatures. A linear fit in the somewhat linear region at the lowest temperature produced a p - value of 1.46 in agreement with the 10 u.c. data.

The 10 u.c. SRO(111) sample is ideal to study the WL effects in SRO, since it has a nice upturn in resistivity at $T_{min} \sim 32$ K. This allows us to collect enough data below the T_{min} to analyze the behavior. The p-value of ~ 1.5 makes it difficult to assign a main scattering mechanism. A p-value of 1 is reported for SRO(111) samples [3]. Our results vary significantly.

Thickness dependent Magnetoresistance

The magnetoresistance is defined as

$$MR(\%) = \frac{\Delta R}{R(0)} \times 100\% = \frac{R(H) - R(0)}{R(0)} \times 100\% \tag{4.5}$$

Where, R(H) and R(0) are the resistance values measured with and without the applied magnetic field, respectively. Fig. 4.15 (a-c) show the magnetoresistance vs applied field at various temperatures for 8 u.c., 10 u.c., and 18 u.c. respectively. A butterfly shaped

hysteresis loop is observed when the temperature is below the ferromagnetic transition temperature of each thickness films. The butterfly loop follows the hysteretic behavior of ferromagnetism in this sample. The negative magnetoresistance is understood as the reduction of magnetic scattering due to the spin alignment from the applied field.

In general, the MR decreases with increasing thickness of the films from the lowest thickness (8 u.c.) as well as with increasing temperature. This is reminiscent of the weak localized systems. For smaller thickness, increased number of point defects, which serve as domain pinning sites, spread the switching field resulting in larger MR. Furthermore, the density of localized electrons is also higher. Upon application of magnetic field, these localized states can become delocalized, and this enhance conductivity. At higher temperatures, thermal de-trapping of the localized states gives rise to enhanced conductivity and thus smaller MR.

We also measured the field dependent changes in sheet resistance. Fig. 4.15 (d) shows the temperature evolution of magnetoresistance (MR) at 7T field of samples with varying thicknesses. The MR(7T) is defined as $\frac{R(7T)-R(0)}{R(0)} \times 100\%$. The MR peaks above 8 uc show a peak around the T_C. Here, we can identify two contributions to the magnetoresistance. For samples larger than 14 u.c. thick, the MR variation is only observed near the FM transition. For 10 - 14 u.c. samples, an increase in negative MR is observed both around T_C and at very low temperatures where quantum corrections to the resistivity are important. The negative MR is consistent with the weak localization picture. For 8 u.c. sample, the MR due to weak localization dominates and the obscures the MR due to spin fluctuations around T_C. We can however still observe a broader dip near the $\sim$75 K. The low temperature magnetoresistance behavior of ultrathin SRO($\leq$ 14 u.c.) manifests

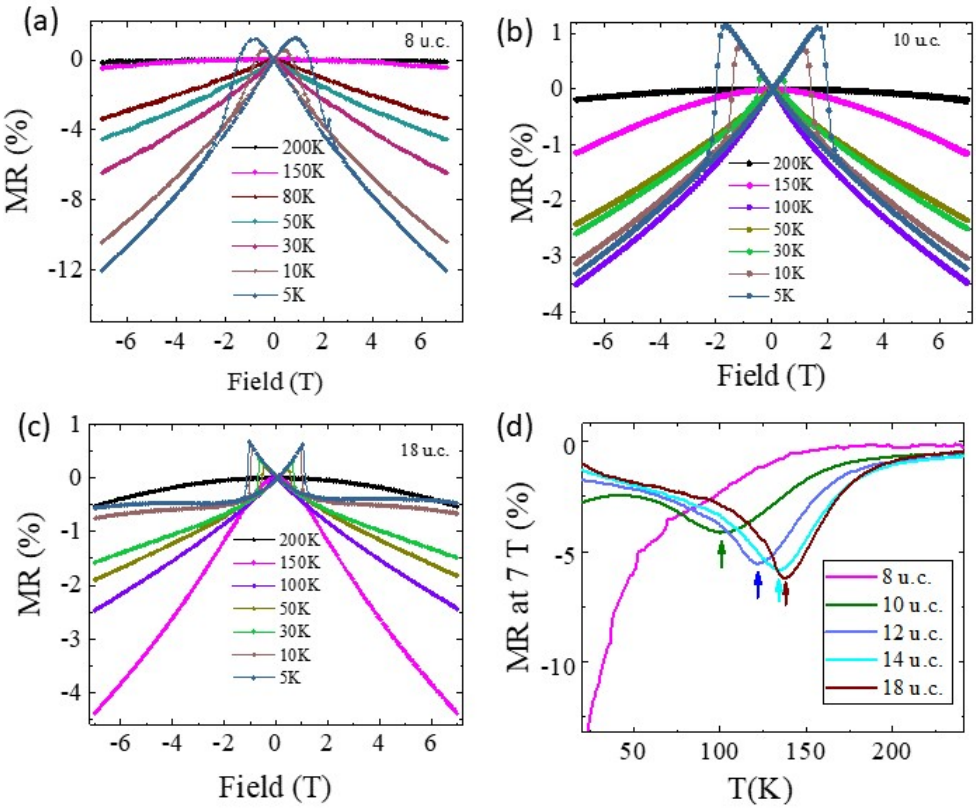

Figure 4.15. (a-c) Variation of magnetoresistance (MR) vs applied field (H) at different temperatures for SRO(111) films of thicknesses 8 u.c., 10 u.c., and 18 u.c. (d)Temperature dependence of MR(7 T) = $\frac{R(7T)-R(0)}{R(0)} \times 100\%$ of SRO(111) films for films of different thickness.

quantum corrections due to weak localization. We do not observe the linear positive MR, observed in 50 u.c. SRO(111) film (see Fig. 4.8), in our thinner samples. However, MR at lower temperatures (5K and 10K) in the 18 u.c. sample, shown in Fig. 4.15 (c), shows some upward curvature at higher fields. This is reminiscent of the linear positive MR behavior.

Summary

In our thickness dependent study of SRO(111) films, we found the magnetic dead layer to be 5 u.c. The 6 u.c. SRO(111) showed a clear ferromagnetic to paramagnetic transition. The transition temperature, T_C, in these samples moves towards higher tem-

perature for samples of increasing thicknesses. We also observed a thickness dependent metal-insulator transition (MIT) in these films. However, the onset of ferromagnetism (6 u.c.) precedes the onset of metallicity, which happens only for 8 u.c. samples. The transport behavior of the insulating yet ferromagnetic samples suggest variable range hopping type of conducting behavior.

The 8 u.c. samples show a temperature dependent MIT as well, defined by a T_{min}. This characteristic temperature, T_{min} gradually moves towards lower temperature with increasing sample thickness. We describe these low temperature resistivity anomalies in extremely thin limits as quantum corrections due to weak localization and are intricately associated with disorder. The p - value of weak localization $\sim$1.5 was obtained for the 10 u.c. SRO(111), which falls closer to electron-electron scattering induced weak localization ($p = 1$ is expected) than the electron-phonon scattering induced weak localization ($p = 3$ is expected). This is contradictory as increased disorder in ultrathin limit is associated with increased electron-phonon scattering at least in SRO(001) films[114] However, ARPES studies on SRO(001) thin films observed a kink in the band dispersion, associated with electron-phonon coupling, which shows negligible thickness dependence[51] suggesting no change in the electron-phonon coupling with disorder. Therefore, electron-phonon scattering may not be the dominant scattering in SRO transport. We also observed that the low temperature (30K - 80K) resistivity behavior is fundamentally affected by the amount of disorder in SRO(111) ultrathin films with the exponent α in $\rho \sim T^{\alpha}$, increasing monotonically with decreasing thickness (increasing disorder).

Two sources of magnetoresistance are identified in our measurements with field applied perpendicular to the sample plane. In addition to the usual hysteretic butterfly MR

loop, at the lowest thickness (8 u.c.), the MR contribution is overwhelmed by the contribution from the weak localization. Both these sources provide a negative contribution and hence are added for samples smaller than 14 u.c. in thickness. For larger thicknesses, this contribution decreases sharply as the weak localization diminishes.

4.5.2. Thickness dependent properties of $SrRuO_3$(001) films

We studied thickness dependent magnetic and transport studies on a series of SRO(001) ultrathin films of varying thicknesses. SRO films of various thicknesses were grown on STO(001) surface. All the films were capped with 2 u.c. of crystalline STO. The capping is done in order to protect the surface.

Thickness dependent magnetic properties of $SrRuO_3$(001) films

A thickness dependent ferromagnetic to paramagnetic transition is observed at 3 u.c. thickness consistent with previous studies. The 3 u.c. SRO(001) shows a clear onset of ferromagnetism. A very similar thickness dependent trend to that of SRO(111) is observed and is summarized in Fig. 4.16. The FM transition temperature, T_C was estimated from the position of the dip in $d\left(\frac{M(T)}{M(5K)}\right)/dT$ curve as shown in Fig. 4.16 (b). The T_C are denoted in the plot with arrows. Fig. 4.16 (d) shows thickness evolution of the transition temperature. The onset of FM at 3 u.c. ($T_C \simeq 110K$) is rather sudden as compared to the SRO(111) samples (see Fig. 4.9). The T_C for the largest thickness of the samples measured (25 u.c.) was about 145 K.

Thickness dependent magneto-transport properties of $SrRuO_3$(001) films

Fig. 4.17 shows the summary of thickness dependent transport properties measurement in SRO(001) films. The films show metallic behavior above a critial thickness of 4

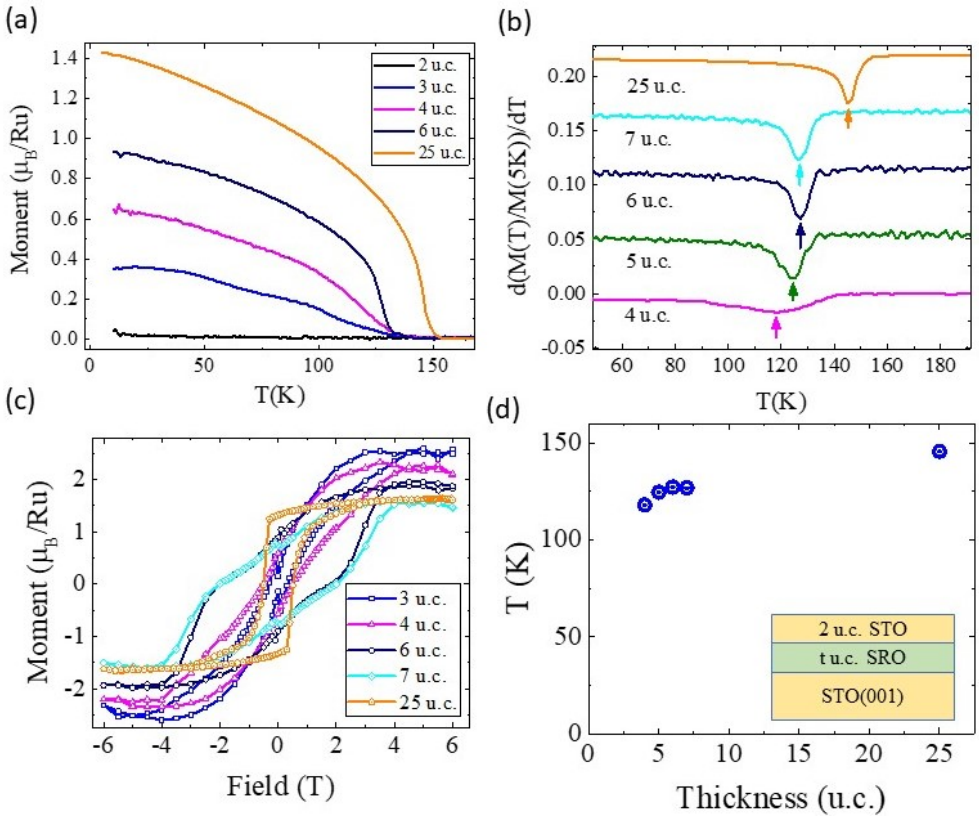

Figure 4.16. (a) Temperature dependence of magnetization of SRO(001) films. (b) $d\left(\frac{M(T)}{M(5K)}\right)/dT$ plotted as a function of temperature. The peaks positions are indicated with arrows. (c) Field dependent MH loops at 5K for various thickness films and (d) T_C obtained from peaks in the curves in (b) are plotted as a function of thickness.

u.c. and are shown in Fig. 4.17 (a). The resistivity is plotted in the log scale on the y-axis. As the thickness is increased, the resistivity decreases monotonously consistent with the previous reports. As we discussed in Section 4.5.1, the position of discontinuity in the dρ/dT corresponds to the FM transition and is plotted in Fig. 4.17 (b). The peak positions are indicated with arrows. Fig 4.17 (c) shows a plot of $\rho(T)$ normalized to the value of resistivity at 300K of various thickness films. For samples in the lower thickness limits, we observe a resistivity minima, T_{min}, that moves towards higher temperatures for decreasing thickness. The position of this minima, along with the T_C obtained from the peaks in dρ/dT are plotted in Fig. 4.17 (d).

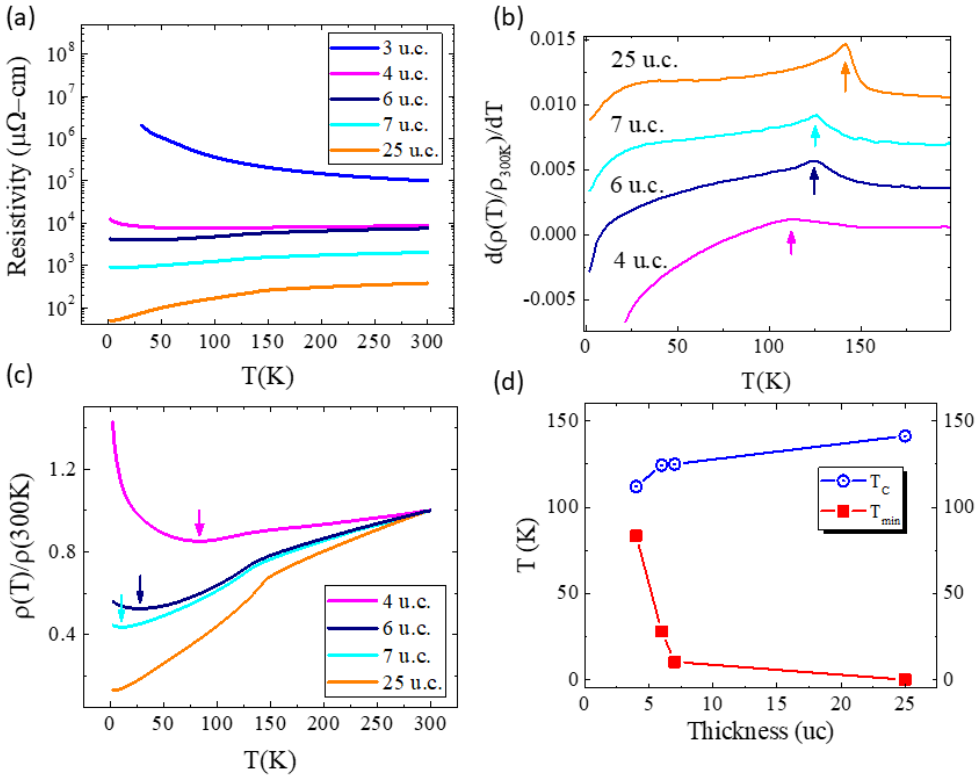

Figure 4.17. (a) Temperature dependence of resistivity of SRO(001) films. (b) $d\left(\frac{\rho(T)}{\rho(300K)}\right)/dT$ plotted as a function of temperature. The peaks positions are identified by the arrow. (c) $\rho(T)/\rho(300K)$ plotted as a function of temperature shows an increase of residual resistivity ratio (RRR) of the films with thickness. The upturns at low temperatures are denoted by arrows. And (d) T_C obtained from peaks in the curves in (b) and T_{min} obtained from (c) are plotted as a function of thickness of SRO(001) films.

Insulating regime and the quantum correction to resistivity

In this Section, we will try to understand the nature of the insulating phase in SRO(001) samples. The lowest thickness sample, i.e. 3 u.c. SRO(001) shown in Fig. 4.17, could not be measured to the lower temperature because of the very large resistance. We have observed that capping with a thicker layer of crystalline STO enhances the transport properties by reducing the measured resistance. Fig. 4.18 (a) shows sheet resistance of two 3 u.c. SRO(001) samples, one with a 2 u.c. STO cap, another with a 10 u.c. STO cap. The sample with heavier capping showed much lower sheet resistance and even shows

metallic behavior at higher temperatures. Therefore, we grew a 2 u.c. SRO(001) sample, and capped it with 10 u.c. of STO. Temperature dependence of resistivity is plotted in Fig. 4.18 (b). It shows insulating behavior in the entire temperature range (10K - 200K). Let us recall equation (4.3) used to describe insulators exhibiting the variable range hopping type conduction.

$$\begin{aligned}
\sigma &= \sigma_0 \, exp\left[-\left(\frac{T_0}{T}\right)^{\nu}\right] \\
\ln\sigma &= \ln\sigma_0 - \left(\frac{T_0}{T}\right)^{\nu} \\
\frac{\partial \ln\sigma}{\partial \ln T} &= \nu\left(\frac{T_0}{T}\right)^{\nu} \\
\ln\left[\frac{\partial \ln\sigma}{\partial \ln T}\right] &= \alpha - \nu \ln T
\end{aligned} \tag{4.6}$$

A plot of $\ln\left[\frac{\partial \ln\sigma}{\partial \ln T}\right]$ vs $\ln T$ should exhibit a linear behavior. The slope of the straight line would give the value of parameter ν that signifies the nature of the hopping. Such a plot for the 2 uc SRO(001) capped with 10 u.c. STO, shown in Fig. 4.18 (c), exhibits linear behavior in the temperature range of 15K - 55K. A linear fit produces a slope of $\sim -\frac{1}{2}$. From equation (4.6), the magnitude of the slope represents the value of ν in equation (4.3). We thus obtain $\nu \sim 1/2$, which is the prediction of E & S variable range hopping conduction. There is a clear discrepancy in the data below 15K. The nature of this discrepancy is not known. However, it could be because of the sheet resistance measured being too close to the measurement limit of our device. We will focus our analysis in the temperature range 15K - 55K. Fig. 4.18 (d) shows a plot of $\ln\sigma$ vs $\frac{1}{T^{1/2}}$. A linear fit in the specified temperature is observed. We therefore conclude that in the insulating regime of SRO(001) ultrathin films, the coulomb correlations between electrons affect the hopping

conduction.

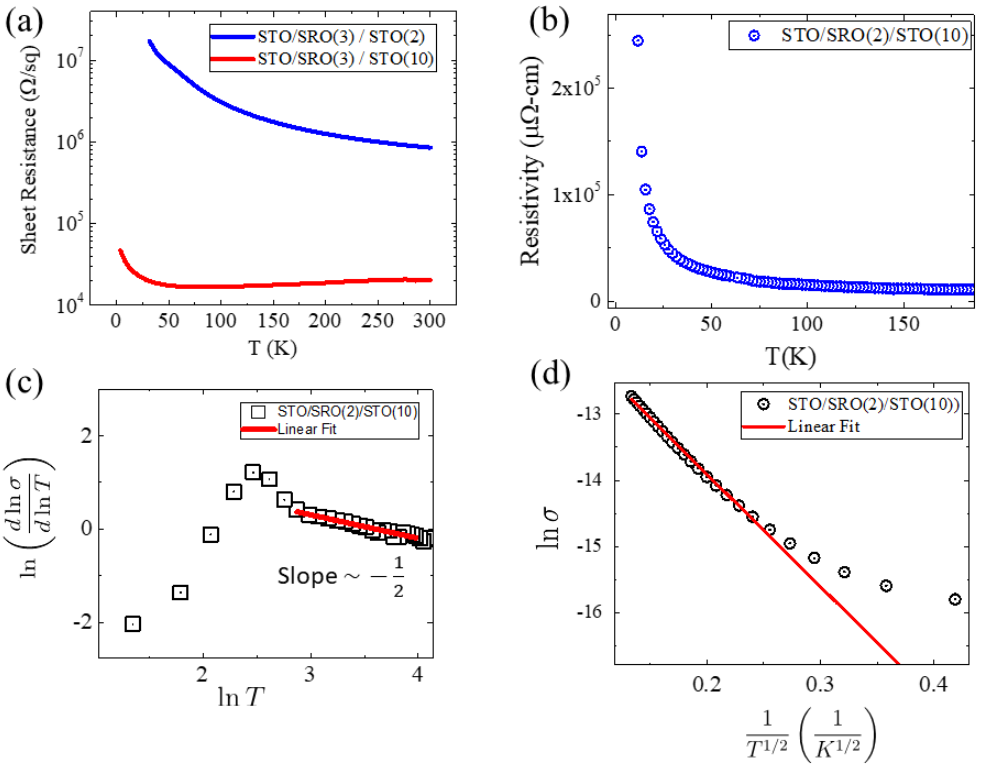

Figure 4.18. (a) Temperature dependence of sheet resistance of a 3 u.c. SRO(001) film capped with 2 u.c. and 10 u.c. of STO (b) Resistivity of 2 u.c. SRO(001) film capped with 10 u.c. of STO as a function of temperature. (c) $\ln\left(\frac{d\ln\sigma}{d\ln T}\right)$ plotted as a function of $\ln T$. A portion of the graph is fitted to a straight line, shown in red and (d) $\ln\sigma$ vs $\frac{1}{T^{1/2}}$ along with a linear fit is shown.

5 - 6 unit cell thickness show a T_{min} similar to the SRO(111) samples discussed in Section 4.5.1. This low temperature increase in resistivity can be understood as a quantum correction to resistivity due to weak localization. Fig. 4.19 shows a plot of dimensionless sheet conductance with ln T. A linear behavior at the lowest temperatures is observed in agreement with weak localization behavior. However, the p - value obtained is an order of magnitude smaller (~ 0.1 for 6 u.c. SRO(001)) than those of SRO(111) films of similar thickness.

This is a surprising result. We do not yet have an explanation for this behavior.

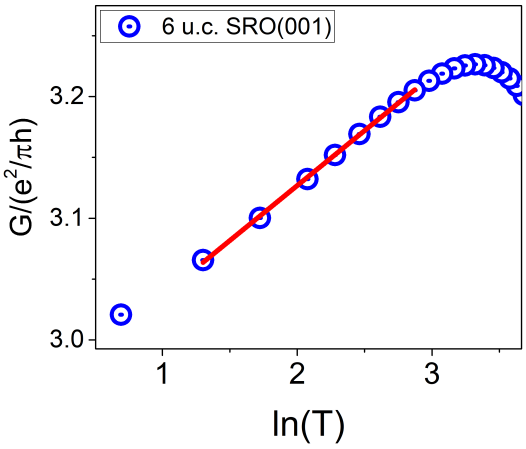

Figure 4.19. Dimensionless sheet conductance plotted as function of ln(T) along with linear fit at lower temperatures for 6 u.c. SRO(001)film.

However, we have generally observed a larger resistivity in our SRO(001) films (compare Fig. 4.10 with Fig. 4.17).

To gain more information about the structure in these ultrathin films, we performed STEM studies on a 5 u.c. SRO(001) film capped with 10 u.c. of STO. A low magnification STEM HAADF image is shown in Fig. 4.20 (a). There are discontinuous regions in our sample. One such discontinuity is indicated by red arrow. Fig. 4.20 (b) shows a magnified region near the discontinuity, which reveals that the discontinuity occurs near the step edge. This means the discontinuity runs along the step edge of our substrate. SRO does not grow in regions near some step edge, while the STO cap fills the discontinuity gap as well. These kinds of trenches in SRO films have been reported before[122]. It was found that SrO termination can self assemble near the step edge forming an array of half unit-cell deep trenches. This is followed by a preferential nucleation of SRO on TiO_2 terminated terraces, making the trenches deeper as growth progresses. The SrO self assembly is likely a result of Sr segregation due to annealing prior growth. If

this is a universal feature in our samples, we expect it to significantly affect the transport behavior.

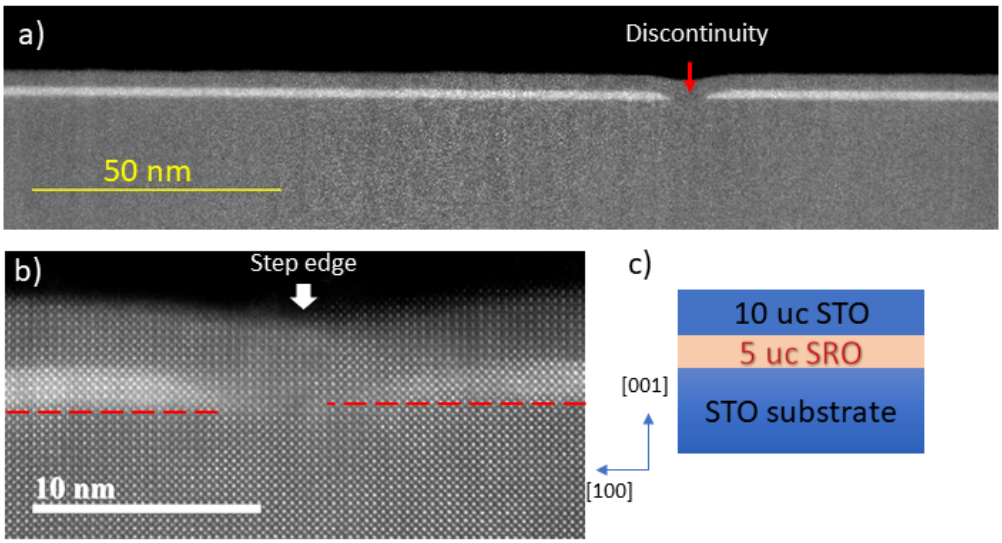

Figure 4.20. a) Low magnification STEM HAADF image of 5 u.c. SRO capped with 10 u.c. of STO film. The films shows discontinuities, labeled with red arrow. b) Zooming into one such discontinuity reveal that they occur near the step edge of the substrate. Schematic of the SRO film.

Thickness dependent Magentoresistance

Magnetoresistance in SRO(001) follow a very similar thickness dependence behavior to that of SRO(111) films. A butterfly loop is observed at temperatures below T_C for samples $\geq$ 4 u.c. in thickness. The hysteresis of the butterfly loop follows the ferromagnetic hysteresis behavior, i.e. increasing coercivities and larger saturation fields with decreasing sample thickness as can be observed from Fig. 4.21 (a-b). For samples with thickness in the range of (4-7) u.c., there are two contribution to MR. One at low temperatures where weak localization is present, and another near the ferromagnetic transition temperature where the MR is due to suppression of spin fluctuation. This is apparent upon inspection of Fig. 4.21 (c).

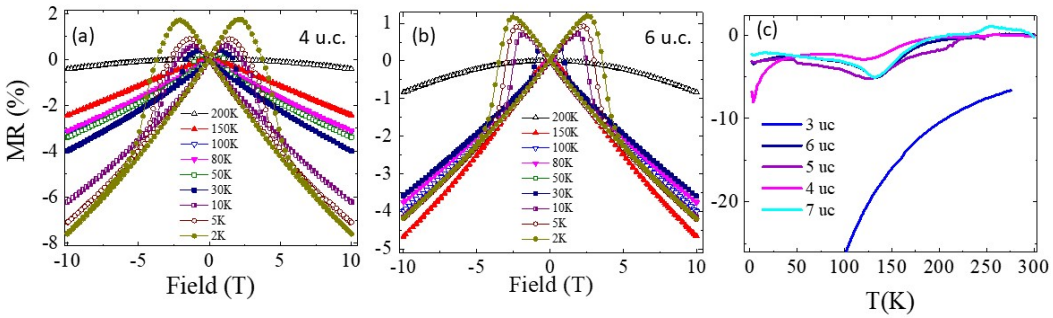

Figure 4.21. (a-b) Magnetoresistance (MR) vs applied field (H) at different temperatures for SRO(111) films of thicknesses 4 u.c., and 6 u.c. (d)Temperature dependence of MR(7 T) $= \frac{R(7T)-R(0)}{R(0)} \times 100\%$ of SRO(001) films for films of different thicknesses.

Summary

To summarize, a very similar thickness dependent magnetization and transport trend to those of SRO(111) samples is observed in SRO(001) films. A common observation is that the transport properties in SRO(001) are inferior to those of SRO(111) in the ultrathin regime. A larger residual resistivity, smaller RRR in similar thickness samples are observed. In the following Section, we will attempt to summarize the thickness dependent properties of SRO films in both these crystallographic orientation and discuss our results.

4.5.3. Summary and Discussion

In this Section, we will summarize our results of the thickness dependent studies in both SRO(001) (Section 4.5.2) and SRO(111) (Section 4.5.1) films. To do so, we recall our discussion of the structural differences in the two directions from Section 1.2.4. Fig. 4.22 (a - b) show the side view and top view structure of the single layer ABO_3 oxide structure along the two crystallographic directions, [001] and [111] respectively. A few key differences in the [111] directions are apparent when looking at the top view of a single layer. First the Ru-Ru distance in the plane is extended to $a\sqrt{2}$, as shown in Fig 4.22 (b) and

second, the Ru-O-Ru connectivity is lost in the single layer along [111] direction. This Ru-O-Ru connectivity is recovered in bilayers along [111] direction as shown in Fig. 4.22 (c). The Ru-O-Ru connectivity is extremely important in $SrRuO_3$ since there is a strong Ru 4d - O 2p hybridization that along with the strong spin-orbit coupling strength drives the properties.

For the sake of comparing the properties in samples in these two crystallographic directions, we define an effective unit-cell, t_{eff}, to be equivalent to a bilayer in [111] direction and a single layer in [001] direction. We will now plot the various magnetic and transport measurements with respect to this effective thickness, t_{eff} and compare the properties of SRO films growth in the two crystallographic directions.

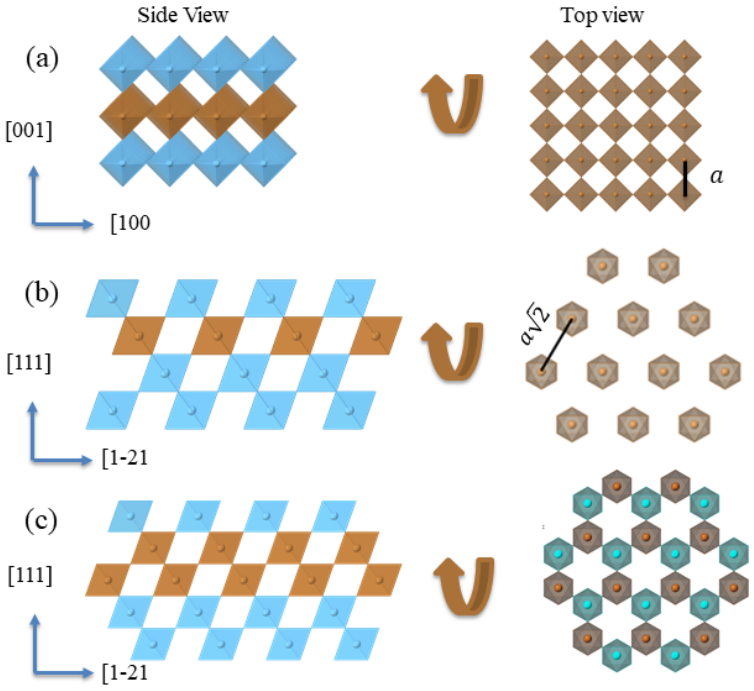

Figure 4.22. a
nd [111] crystallographic direction]Top and side view of the a single layer crystal structure in the (a) [001] and (b) [111] crystallographic direction. and (c) Bilayer in the [111] crystallographic direction showing a buckled honeycomb structure. Sr-atoms are omitted and the O-atom should be understood to be at the corner of each Ru-octahedron.

A summary of our results is presented in Fig. 4.23. In general, very similar electronic and magnetic properties are observed. There exists a thickness dependent metal insulator transition around 4 t_{eff} unit cells thickness. The conduction in the 3 t_{eff} u.c. insulating samples, in both [001] and [111] directions, is driven by ES variable range hopping conduction. ES VRH conduction is a signature of stronger coulomb interaction that leads to a suppression of the density of states near the Fermi level. This signifies the importance of electron correlation in ultrathin SRO films. For thicker samples, we saw the samples become metallic with low temperature insulating behavior which was found to be driven by two dimensional weak localization driven by disorder. The Fermi liquid regime in the metallic samples at lower temperatures is a universal feature and is present in all the metallic samples above $t_{eff} = 5$ u.c. There is a temperature regime ($\sim$ 35K - 80K) where the resistivity follows fractional power dependence on temperature ($\rho \sim T^{\alpha}$) in the metallic samples. We found that the exponent α scales linearly with T_{min}. T_{min} is an indicator of disorder in the sample. Larger T_{min} indicates larger disorder in the film. Since disorder increases with decreasing thickness, we found that α scales linearly with disorder. We have observed that α approaches to 1 in our thickest samples $t_{eff} \sim 25$ u.c. an indication of minimal disorder in our thicker samples.

A thickness dependent ferromagnet to paramagnetic transition is observed around t_{eff} of 3 u.c. The t_{eff} $\sim$3 u.c. are the insulating yet ferromagnetic samples. The loss of ferromagnetism in the two direction with decreasing thickness show slight differences in the T_C variation with thickness. In SRO(001), the T_C variation with thickness is minimal with an abrupt loss of ferromagnetism at 3 u.c., however, in SRO(111), the T_C gradually decreases until it vanishes below 3 t_{eff} u.c.

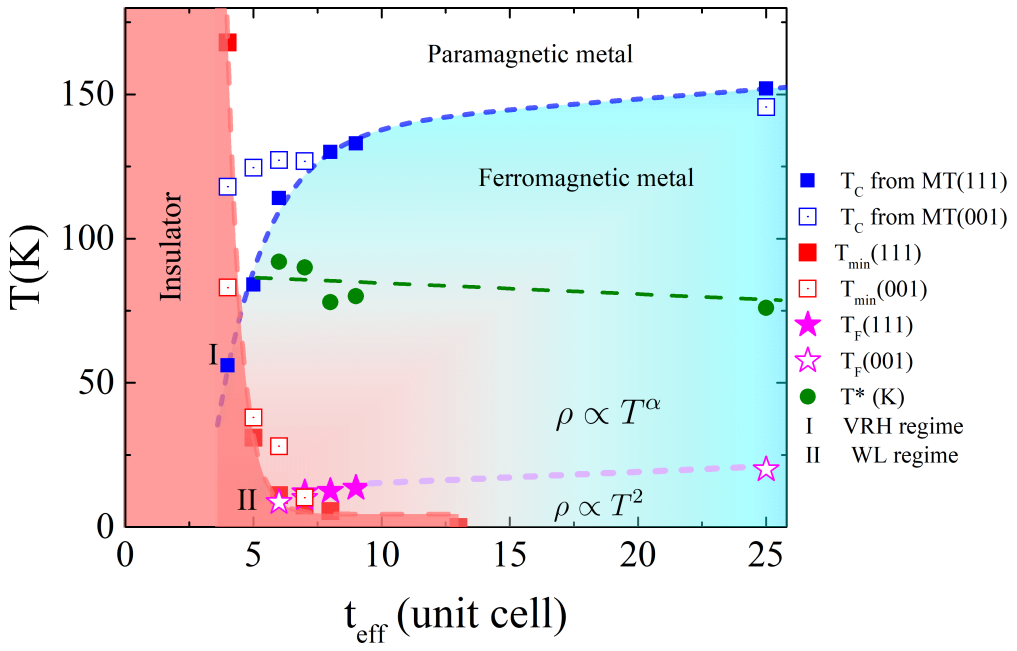

Figure 4.23. Thickness and temperature dependent scaling behavior for electronic and magnetic phases in SRO(001) and SRO(111) films. The SRO(111) data are shown in solid data markers while the SRO(001) data are shown with hollow markers. T^* marks the position of the maximum temperature wherein $\rho \sim T^{\alpha}$, $\alpha \neq 1$, behavior is observed.

Chapter 5. Structure of Transition Metal Oxide Thin Films on Cleaved Single Crystal Substrates of Layered Ruthenate

5.1. Introduction

Materials in thin films are usually grown on a crystal substrate that is cleaved along a certain crystallographic direction and mechanically polished to obtain a smoother surface with terraces. Vicinal substrates are commercially prepared to aid the process of nucleation. The choice of substrates with atomically defined surfaces are limited. However, there are a class of materials that possess a natural cleaving plane. Ruddlesen Popper (RP) series of ruthenates are one such class of materials and are described by the general formula $A_{n+1}Ru_nO_{3n+1}$. This formula can be rewritten as $AO(ABO_3)_n$, where n perovskite layers are stacked between rock-salt AO layers along the crystallographic c-axis [123, 124]. As n increases, the materials demonstrate more three-dimensional character due to larger number of ABO_3 slabs between the rock-salt layers, as shown schematically in Fig. 5.1. The double rock salt layer (AO-AO), indicated by red arrows provides a weak cleaving plane for RP with n$\neq \infty$. These layered materials provide an opportunity to expand upon the limited choice of substrates available for oxide film growth. By cleaving the single crystals inside high vacuum, we can obtain extremely clean, singly terminated surfaces for film growth.

Our choice of the RP ruthenate substrate is the n=2 member of the RP ruthenate Sr_2RuO_4 (SRO214), the most quasi-2D crystal of RP ruthenate series. SRO214 in bulk

Section 5.3 of this chapter have been previously published as Prahald Siwakoti, Hangwen Guo, Zhen Wang, Yimei Zhu, Rosalba Fittipaldi, Antonio Vecchione, Y. Wang, Zhiqiang Mao, and Jiandi Zhang "Coherent growth of oxide films on a cleaved layered metal oxide substrate." *Physical Review Materials* 2.10 (2018): 104407 and Zhen Wang, Hangwen Guo, Shuai Shao, Mohammad Saghayezhian, Jun Li, Rosalba Fittipaldi, Antonio Vecchione, Prahald Siwakoti, Yimei Zhu, Jiandi Zhang, and E. W. Plummer "Designing antiphase boundaries by atomic control of heterointerfaces." *Proceedings of the National Academy of Sciences* 115.38 (2018): 9485-9490.

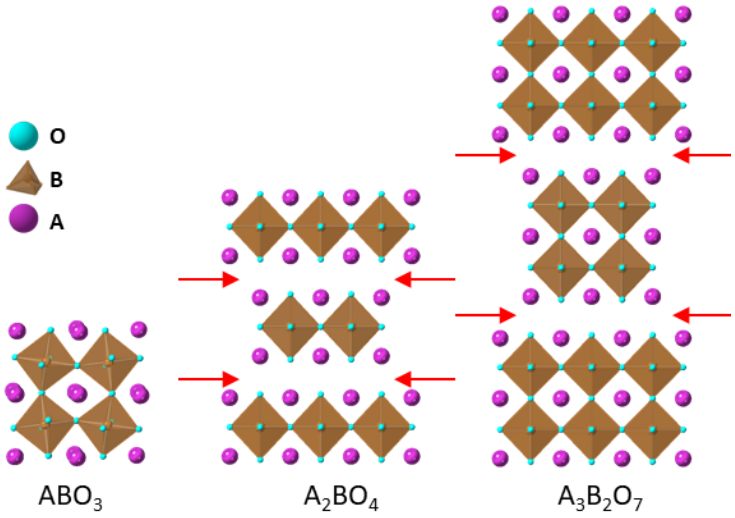

Figure 5.1. Three example members of the RP family. ABO_3(n=∞) perovskites, A_2BO_4 (n=1) and $A_3B_2O_7$ (n=2.)

exhibits a body-centered tetragonal space-group (I4/mmm) symmetry with lattice parameters a = 3.873 Å and c = 12.74 Å. While the (001) unreconstructed surface of SRO214 has the same 4-fold symmetry as that of the (001) surface of the widely used commercial substrate $SrTiO_3$(STO), the surface has a well known $(\sqrt{2} \times \sqrt{2})$R45° reconstruction through an in-plane RuO_6 rotational distortion in the surface layer[85]. Furthermore, the c-lattice parameter (along the [001] crystallographic direction) is almost three times as large. This gives rise to steps with larger step height than the unit-cell height of most perovskite oxides which will in turn create shear strain at the phase boundary near the step edge. We will discuss the formation of these 2-dimensional defects with reference to two perovskite oxides: $SrRuO_3$ (written hereafter as SRO113 to distinguish it from SRO214) and $La_{2/3}Sr_{1/3}MnO_3$ (LSMO). LSMO has excellent in-plane lattice matching with the substrate SRO214, SRO113 on the other hand is under large compressive strain.

On the functional properties aspect, a ferromagnetic material (LSMO or SRO113) interfaced with a superconductor (SRO214) can be a model system to study spin trans-

port behavior. SRO214 is suspected to be a triplet spin superconductor (TSC). Proximity effect, which is defined as the penetration of cooper pair into the metal, occur in Ferromagnetic metal/Superconductor interfaces as well. The coherence length, ζ_F, however, is considerably smaller (no more than a few nanometers) [125]. But spin-triplet cooper pairs can be insensitive to the ferromagnetic exchange interaction, thus obtaining longer coherence length. Therefore, FM/TSC heterostructures are suggested to be a possible route to achieve long-range spin supercurrent [126]. Our focus is on the structural characterization of these films and the interfaces and not on the experimental realization of spin-transport devices. We show that a high quality heterostructure with minimal chemical intermixture and sharp interface can be obtained in both instances. We use various tools to investigate the quality of the interface.

SRO113/SRO214 also provides a unique opportunity to study the effect of lattice strain and symmetry mismatch. Since both the A-site and B-site elements of the substrate and the film are the same, the complications due to elemental intermixture at the is essentially eliminated. This will enable us to study the structural changes near the interface that happen for the accommodation of $\sim 1.5\%$ compressive strain as well as octahedral symmetry mismatch.

5.2. Preparation and Characterization of Substrate Surface

An Al rod was glued onto a SRO214 single crystal substrate using silver epoxy. The substrate with the Al rod was then transferred into the cleaving chamber, with a base pressure of 10^{-9} Torr and cooled down to the liquid nitrogen temperature (77 K). The crystal was cleaved by knocking off the Al rod to obtain the SRO214 (001) surface and

then transferred to the main characterization chamber with the base pressure of 2×10^{-10} Torr. The cleaved surfaces obtained were characterized using low energy electron diffraction (LEED) and scanning tunneling microscopy (STM). STM topography images of a freshly cleaved surface, as shown in Fig. 5.2 (a), reveal that cleaving at low temperature and high vacuum exposes large flat terraces. The step heights are integral multiples of half the unit-cell length in the c-direction (6.4 Å) as can be seen in the line profile graph in 5.2 (b). This shows that the cleaving occurs between two weakly bonded SrO layers. Fig. 5.2 (c) shows the LEED diffraction image of the surface of a freshly cleaved SRO214. The diffraction pattern consists of both integer spots and fractional spots with two orthogonal glide lines, showing a ($\sqrt{2} \times \sqrt{2}$ R45° reconstructed unit cell, indicating a surface reconstruction. At the surface, the Σ_3 zone boundary soft-phonon mode in the bulk freezes into a static lattice distortion associated with an in-plane rotation of the RuO_6 in the top octahedral layer, in agreement with previous studies [85].

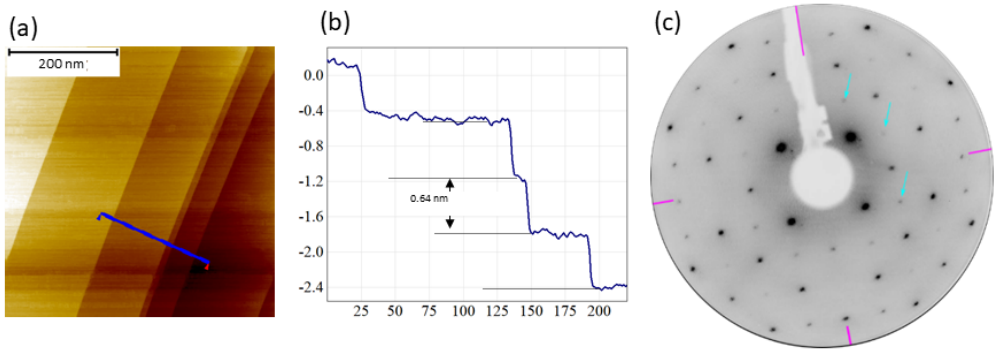

Figure 5.2. Surface characterization. a) STM image of a cleaved surface of SRO214 showing steps and edges b) Line profile across the steps to monitor step height and terrace width and c) LEED diffraction pattern of the surface showing $\sqrt{2} \times \sqrt{2}$ R45° reconstruction. The fractional spots are indicated cyan arrows while two glide lines are indicated by solid lines.

5.3. $La_{2/3}Sr_{1/3}MnO_3/Sr_2RuO_4(001)$ Thin Film Interfaces

LSMO has a rhombohedral space-group symmetry with lattice constant a = 3.878 Å, whereas. The lattice mismatch between these systems is ≈ -0.1%. Because of this near-perfect lattice match we do not expect any strain induced structural modifications. However, there is an octahedral symmetry mismatch. LSMO has a rhombohedral symmetry with robust oxygen octahedral tilts and rotations whereas SRO214 bulk does not have any tilts and rotations.

5.3.1. Growth and Surface characterization

SRO214 single crystals of dimensions 5 mm × 3 mm × 0.5 mm were used as substrates to grow LSMO thin films using Pulsed Laser Deposition (PLD). A stoichiometric $La_{2/3}Sr_{1/3}MnO_3$(LSMO) target was illuminated with a KrF excimer laser (λ = 248 nm) at a repetition rate of 10 Hz and a laser energy of 120 mJ. The oxygen partial pressure of 80 mTorr, was obtained with a mixture of 99% O_2 and 1% O_3 and maintained during growth while the substrate temperature was fixed at 700°C.

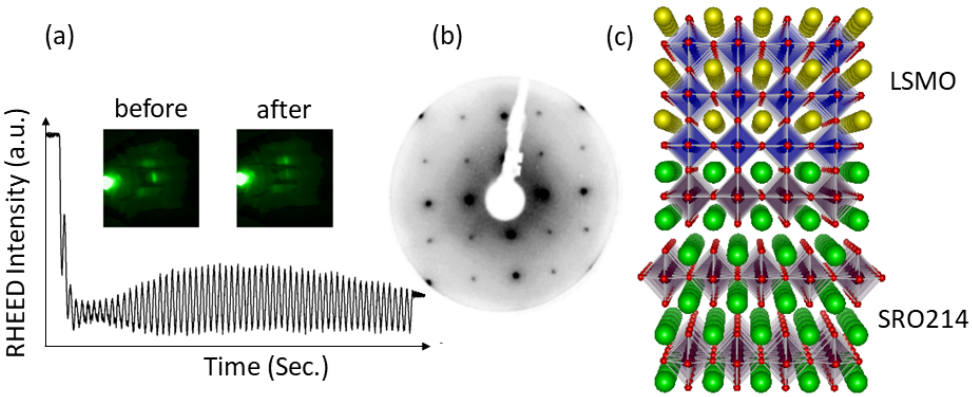

Figure 5.3. (a) RHEED pattern is sharp both before and after growth. The RHEED intensity oscillations are used to monitor thickness while growth. b) LEED diffraction pattern of a 10 u.c. LSMO thin film on a SRO214 substrate measured at a beam energy of 107 eV. c) A ball model of LSMO thin film on SRO214 substrate.

Thin film growth was monitored using reflection high energy electron diffraction (RHEED) oscillations. As shown in Fig.5.3 (a), layer by layer growth was achieved. Sharp diffraction spots for both before and after growth from the surfaces indicate a good quality thin film growth. In our surface sensitive LEED measurements, we observed that the surface of the LSMO films is always unreconstructed for the films grown at optimum oxygen environment. The $(\sqrt{2} \times \sqrt{2})$R45° surface reconstruction goes away even for a single layer of LSMO. And the bulk truncated (1×1) structure is persistent for larger thicknesses as evident by the LEED pattern on a 10 u.c. LSMO film shown in Fig. 5.3 (b). This indicates that the rotational distortion of the RuO_6 octahedra at the substrate surface is diminished as the film growth begins. Therefore, we believe the surface layer of SRO214 restores itself back to a non-distorted tetragonal structure when the interface is formed.

5.3.2. Chemical characterization with X-ray photoemission spectroscopy

The chemical composition of LSMO films was studied using angle resolved X-ray photoelectron spectroscopy (ARXPS). A monochromatic Al Kα x-ray source and a PHOIBOS 150 energy analyzer, both from SPECS, were used to measure the core level spectra of Sr 3d and Mn 2p.

The spectra taken at larger emission angle (θ) are more sensitive to the surface, because the probe depth is smaller than the normal emission. The shape of Sr 3d spectra undergo obvious change with different θ as shown in Fig. 5.4. To quantify the changes, we take intensity ratio of Sr 3d to Mn 2p at two emission angles (θ =0° and 60°). There is obvious Sr segregation on the surface. We did not observe any signs of change in Mn valence in surface as compared to the bulk. Mn 2p peaks in XPS are not very sensitive to

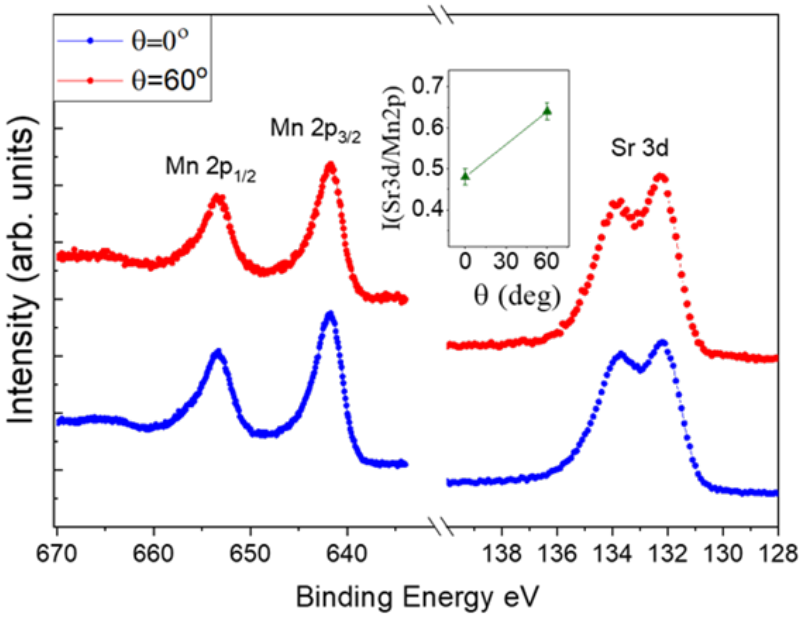

Figure 5.4. Core level XPS spectra of LSMO film is taken at two different emission angles. Mn 2p and Sr 3d core levels are probed. The inset shows the ratio of intensity of Sr 3d to the Mn 2p peak as the collection angle is varied.

the change in Mn valence. However, Mn 3s doublet splitting is known to show indications of change in Mn valency. We did not observe any such changes in Mn 3s doublet splitting as well.

5.3.3. Anti-phase boundary using crystal symmetry.

We have examined the detailed structure of the LSMO thin film along and the interface by employing atomic- resolved STEM. As discussed in Section 5.2, the steps of the SRO214 substrate have heights that are integral multiple of half the unit cell height along 001 (= 6.37 Å). However, the pseudo-cubic lattice parameter of LSMO is 3.878Å. Therefore, the smallest step height is almost equal to 3/2 of the LSMO unit cell. This is shown schematically in Fig. 5.5 (a-b). This creates an interesting boundary, right at a step edge, where we have an anti-phase stacking. This two dimensional defect is defined

as anti-phase boundary (APB). The height difference (δ), between the step height and 3/2

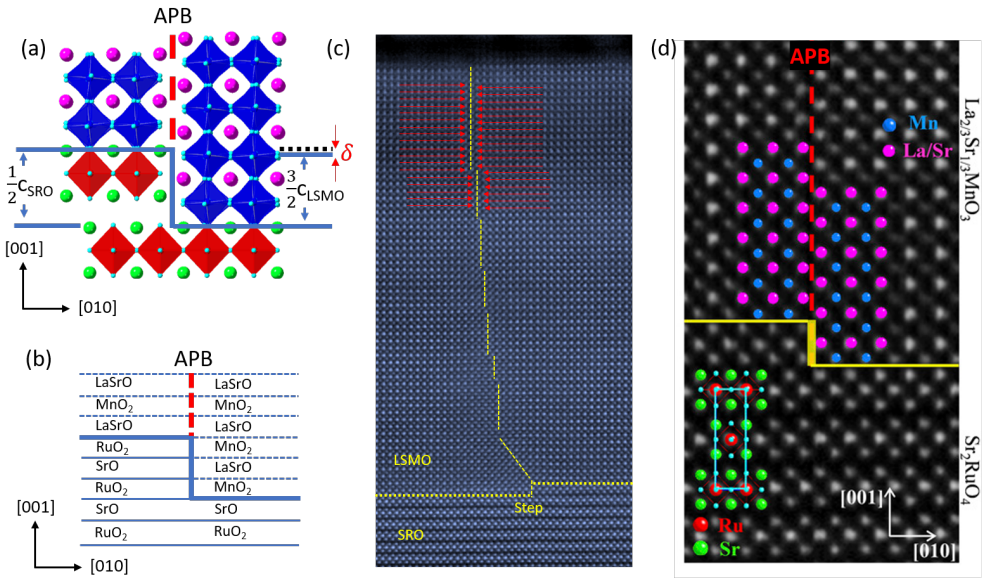

Figure 5.5. (a – b) Schematics showing the various possible stackings near the step edge. The cyan line marks the interface which also includes a step of half the c-axis parameter of SRO214 along the [001] direction. The position of the anti-phase boundary is shown in red dashed line. δ marks the difference between the half the c-axis parameter of SRO214 and 3/2 of the c-axis parameter of LSMO. (c) a large scale HAADF STEM image of a 60 u.c. LSMO thin film showing the formation of a 2D defect boundary originating at a step edge. These defects are extended all the way to the surface as shown. (d) a smaller scale region near the step edge showing the atomic stacking.

of LSMO unit cell, creates an additional shear strain along the growth direction near the phase boundary which becomes important to understand the dynamics and distribution of such two-dimensional defects. Fig. 5.5 (c) shows the HAADF stem image of a 60 u.c. LSMO thin film grown on a SRO214 (001) surface. The column intensity in a HAADF-STEM image is proportional to the atomic number. Hence, the step and interface, as well as the various elements can be identified by a Z-contrast image. We can clearly identify the interfaces and the steps as indicated with yellow dashed lines. We also observed the ABPs originating at a single step. This kind of boundary is seen to travel all the way to the surface of the film as shown in Fig. 5.5 (c). The APB are also indicated with orange

dashed lines. Fig. 5.5 (d) shows a zoomed in region near the interface. The atomic positions of La/Sr and Mn atoms are shown validating our stacking sequence sketched in Fig. 5.5 (a-b). Generally, the APB are straight with occasional stair like steps, and they travel all the way to the surface. Fig. 5.6 (A) shows an APB that originates at a single step and travels towards the surface almost perpendicularly. Fig. 5.6 (B) however, shows a region where there are two APBs generated close to each other. In the latter case, we observe them travelling towards each other laterally as well until they finally coalesce. Once two APBs merge, the boundary no longer exists. By employing a combination of atomically resolved STEM, first principles and defect theory, the latter two of which are not discussed here, we have shown a method of generating a well-defined 2D defect structure (APBs)[127].

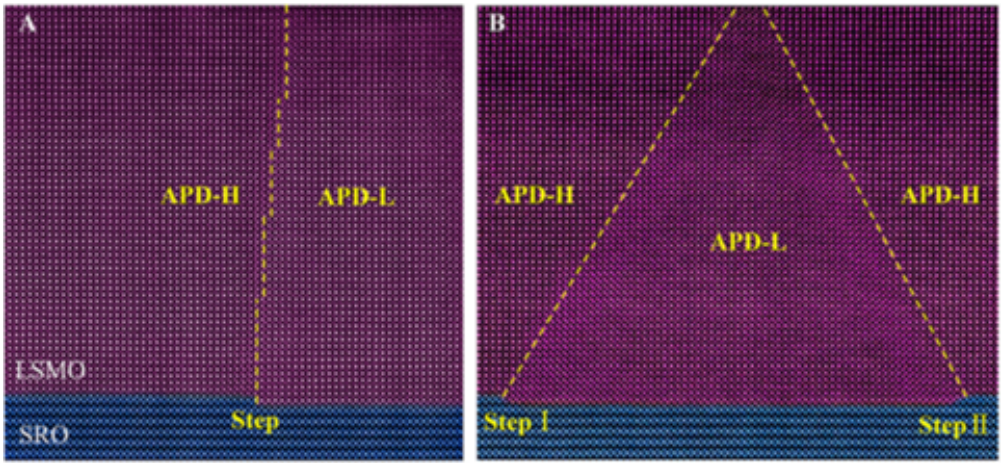

Figure 5.6. (A) HAADF image of an APB originated on a single step and travels almost perpendicularly to the surface. (B) A case with two APBs, where they move towards each other and form a triangular structure.

5.3.4. Microscopic structural characterization of region away from defects.

In Fig. 5.7 (a) large-scale HAADF-STEM image for an LSMO/SRO214 film taken along the [100] direction shows an atomically well-defined and coherent interface without

obvious dislocations. High-magnification HAADF- and ABF-STEM images at the interface are presented in Fig. 5.7 (b). The position of the interface in these images, as indicated by a yellow dotted line, can be determined based on the intensity profile of the HAADF image plotted at the bottom of Fig. 5.7 (b). The column intensities are uniform throughout the sample except for the one layer on both sides of the interface. This indi-

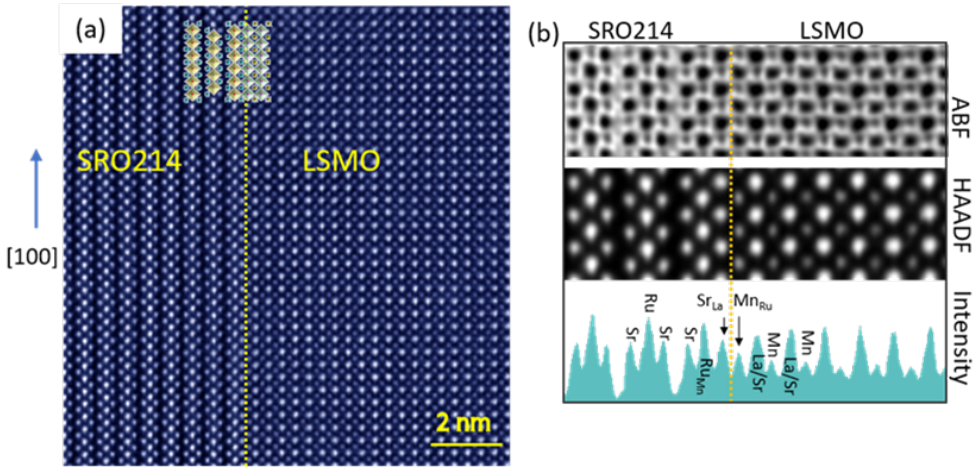

Figure 5.7. (a) A HAADF-TEM image near the interface of 60 u.c. LSMO thin film grown on SRO214 (001) substrate. (b) The comparison of HAADF- and ABF-STEM images as well as the intensity profile for the HAADF image taken along [100] direction.

cates intermixture with heavier elements on both sides. To evaluate the possible variation in lattice structure across the interface, we extract the c-axis lattice parameters in the atomic layer-by-layer steps near the interface of the substrate and film as shown in Fig. 5.8 (b). On the SRO214 side, the measured c-axis lattice parameter is identical to that in the bulk of SRO214, except for the interface layer where RuO_6 is elongated by $\approx$ 0.1 Å along the [001] direction. The c-axis lattice spacing of the film, however, is slightly larger than the bulk value. Notably, the first MnO_6 octahedron layer has an out-of-the-plane lattice expansion by more than 0.1 Å. The observation of this tetragonal distortion of the film in the absence of lattice mismatch with the substrate is surprising and needs

further exploration. One possibility is that LSMO in this epitaxial film becomes tetragonal by diminishing the rhombohedral distortion existing in bulk LSMO. So, it becomes possible to study the effect of octahedral symmetry mismatch alone. To characterize the nature of intermixing at the interface, we performed a detailed EELS study. Chemical intermixing is commonly observed in oxide thin films and tends to be unavoidable. Fig. 5.8 (a) shows the layer-by-layer averaged elemental profiles, extracted from the EELS spectra by integrating the signal of La-M, Ru-M, Sr-L, and Mn-L edges, superimposed onto the corresponding atomic sites in the HAADF images. Since the intensity of Mn in the first layer is significantly smaller and Ru does not drop down to zero in the first layer of MnO_2 at the interface, Ru-Mn intermixing may occur in the first unit-cell at the interface. The intensity of Sr in the first La/Sr-O layer in the film is larger than the bulk stoichiometric value of 33% and is accompanied by a decrease in La intensity in the same layer. This suggests that La/Sr intermixture also happens in the first unit cell at the interface.

The fine structure of O K and Mn L edge excitations in EELS spectra, as displayed in Fig. 5.9 (a), provides some insight into the electronic properties at the interface. The first peak labelled 'a', commonly referred as a pre-peak, has a strong contribution from the Mn 3d e_g band. This peak is sensitive to bonding features of the octahedron [128].

The second peak labelled 'b', however, is commonly attributed to the hybridization of the O 2p with La 5d and/or Sr 3d bands [96]. The energy separation between the peaks 'a' and 'b' in the O-K edges is an accurate method to quantify the Mn oxidation states [96]. Fig. 5.9 (b) shows that, in the LSMO film, the peak energy separation does not change, suggesting a uniform oxidation state in the film throughout the thickness of the film. Mn L edges are the results of excitations of Mn 2p electrons to the unoccupied

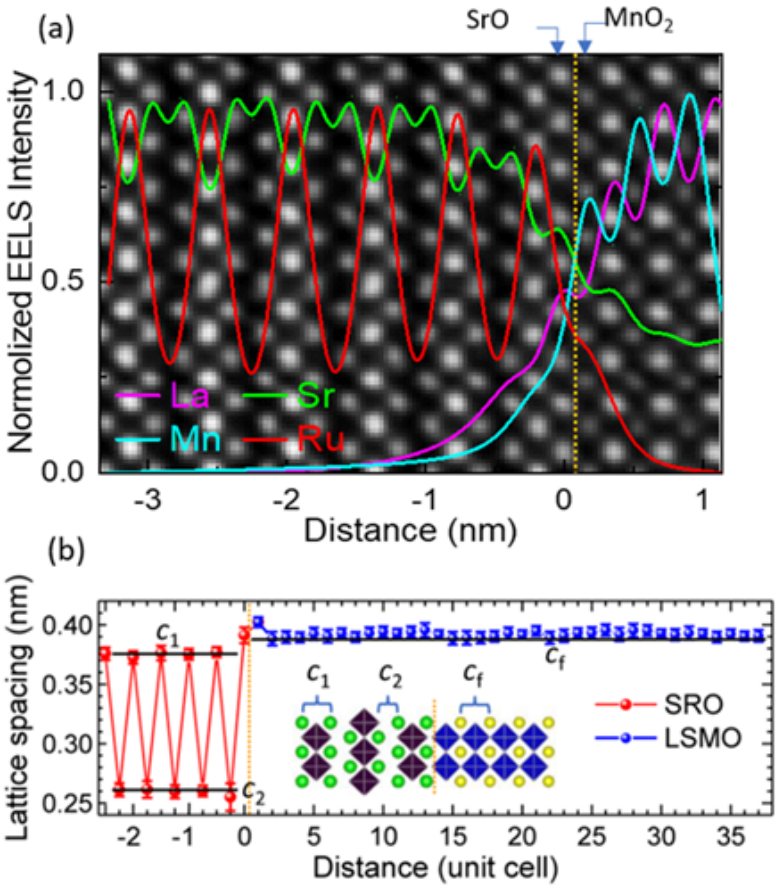

Figure 5.8. (a) Composition profile extracted from EELS spectrum for La, Sr, Mn, and Ru across the LSMO/SRO214 interface, illustrating the Mn-Ru and La-Sr diffusion at the interface (b) Lattice spacing variation across the interface (the inset shows the model heterostructure).

d states above the Fermi energy. Mn L edges consist of two white lines L_3 and L_2 arising due to transitions from $2p_{3/2}$ and $2p_{1/2}$ core states to 3d unoccupied states. The ratio of the intensities of the L_3 and L_2 lines is also characteristic of the manganese oxidation states. Using EELS spectra collected from bulk LSMO samples as reference, the oxidation states of Mn ions can be determined from the Mn $L_{2,3}$ ratio and is shown in Fig. 5.9 (c). The value of $\approx (3.31 \pm 0.08)$ measured for the LSMO film is very close to bulk LSMO. However, for the Mn doped into the top RuO_2 layer on the substrate side, the Mn $L_{2,3}$

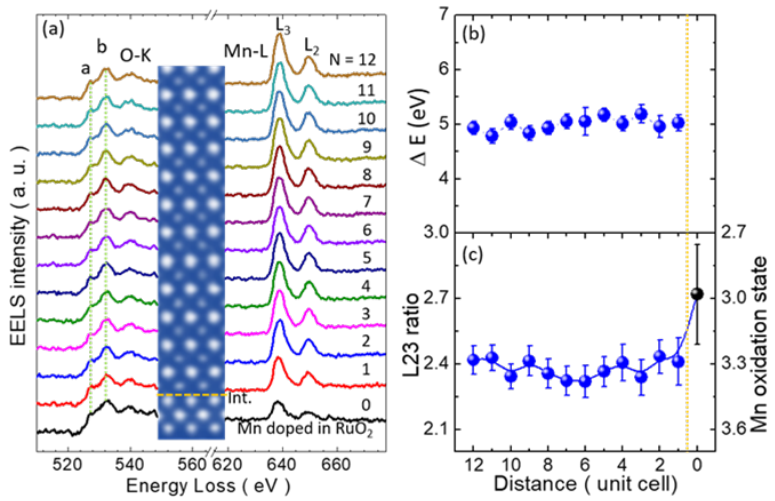

Figure 5.9. (a) Background subtracted EELS spectra of layer-by-layer O K edge and Mn L edge across the LSMO/SRO214 interface. The inset is the corresponding HAADF-STEM image. Evolution of Mn oxidation states determined by (b) energy separation (E) between pre-peak (marked as a) and main peak (marked as b) in O-K edges and (c) $L_{2,3}$ ratios (i.e., the intensity ratio of L_2 to L_3 peak) as a function of distance from interface. The dotted yellow line indicates the position of interface.

ratio does increase, suggesting a lower chemical valence of Mn. This is unusual since Mn would be expected to increase its valence when it replaces Ru^{4+} ion in SRO214. The possible existence of high density of oxygen vacancies at the interface is a feasible explanation for this behavior.

5.4. $SrRuO_3/Sr_2RuO_4$(001) Thin Film Interfaces

SRO113, in its bulk, form has an orthorhombic crystal structure with the pseudo-cubic lattice constant of 3.93 Å. SRO214 in bulk exhibits a body-centered tetragonal space-group (I4/mmm) symmetry with lattice parameters a = 3.873 Å and c = 12.74 Å. Large in-plane compressive strain of about -1.5% exists between these two materials. A model shown in Fig. 5.10(a) also shows that in addition to the lattice mismatch, there is also a symmetry mismatch. SRO113 has robust octahedral tilts and rotations while

SRO214 has no rotations and tilts, except for a small rotation in the pristine surface as discussed in Section 5.2.

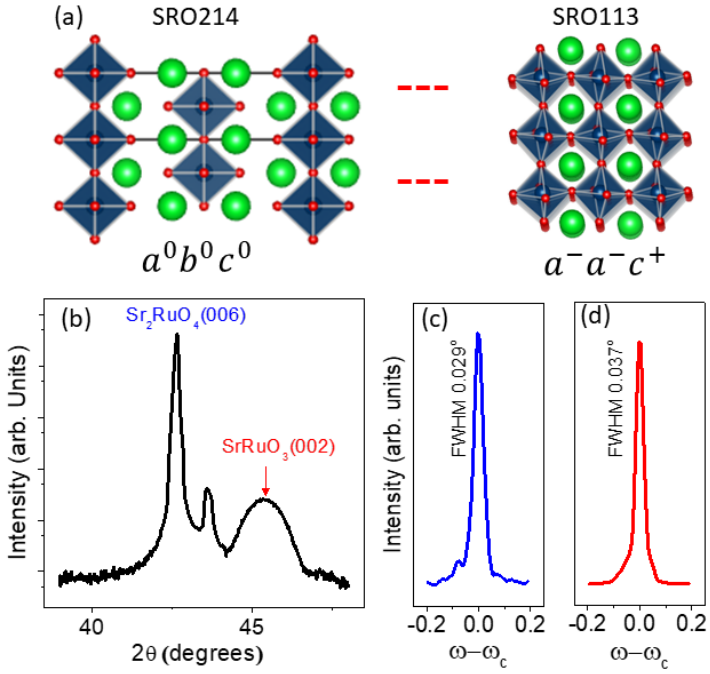

Figure 5.10. a) Model structure showing the crystal structure of tetragonal SRO214 and orthorhombic $SrRuO_3$ b) Coupled scan about the 006 SRO214 peak. The position of the film peak is labelled. No interference fringes are observed. c) Rocking curve on the substrate and d) Rocking curve on the film peak

5.4.1. Thin film growth and characterization

A stoichiometric $SrRuO_3$ ceramic target was illuminated with a KrF excimer laser ($\lambda = 248$ nm) at a repetition rate of 10 Hz and a laser fluence of 1 J/cm^2. The oxygen partial pressure of 80 mTorr, was obtained with a mixture of 99% O_2 and 1% O_3 and maintained during growth while the substrate temperature was fixed at 700 °C. High resolution X-ray diffraction experiments were performed on a 12 nm thick SRO113 film. Coupled scan about the (002) Bragg peak of the SRO, shown in Fig. 5.10 (b), reveals a clear peak with one discernible interference fringe. Since the substrate surface is cleaved inside

the vacuum, the area of the flat surface was not large enough to get good scans at least for the laboratory XRD setup. Nevertheless, we can gain valuable information. A simple calculation of the Bragg peak tells us that the c-axis of SRO film is extended to 3.99Å. The rocking curve on the substrate and the film peak are shown in Fig. 5.10 (b-c). The crystallinity of the film is almost as good as the substrate.

5.4.2. Structural and Elemental characterization with STEM/EELS

To examine the microscopic structure, we performed high resolution STEM/EELS measurements. The detail of the experiment is very similar to what we did for LSMO/SRO214. In the following Section, we will present some major findings.

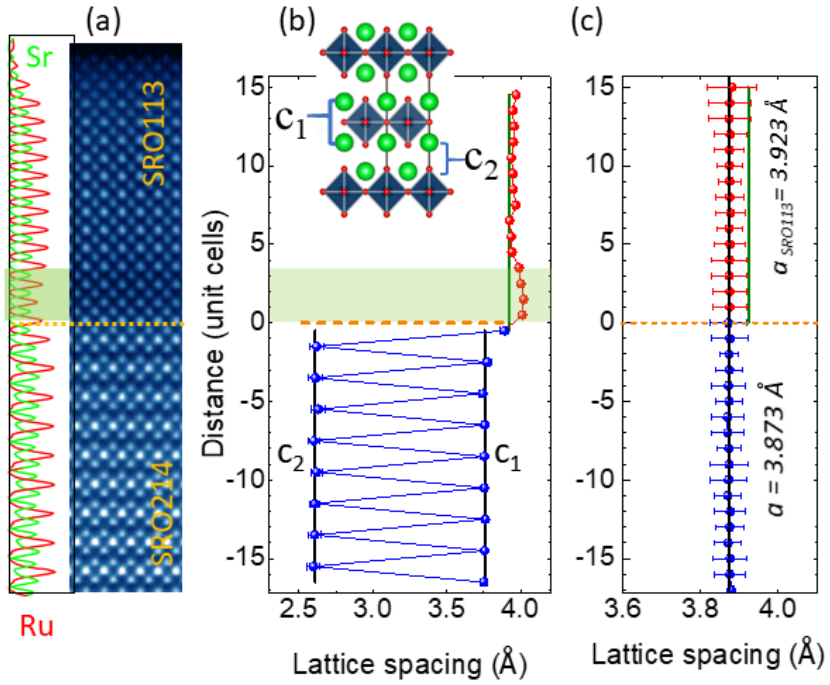

Figure 5.11. a) A HAADF image of SRO113/214. The layer-by-layer elemental profile of Ru and Sr from EELS are also shown. b) out of plane lattice parameters. The inset shows the sketch of SRO214 with definition of c_1 and c_2 parameters, and c) in-plane lattice parameters extracted from HAADF image are presented. The model on the side shows the definition of c_1 and c_2.

Fig. 5.11 (a) shows a HAADF image of SRO113/SRO214 taken along [100] direc-

tion. The interface is denoted by yellow dashed line. Elemental map of Ru and Sr obtained from EELS are also superimposed to the HAADF image. Well defined structure with 113/214 stacking is observed with a sharp interface. The substrate terminates with SrO layer, and the film growth begins with a RuO_2 layer. On the far side of both the SRO113 film and the SRO214 substrate, the elemental intensity profile is uniform. However, close to the interface, we see that the Ru intensity drops for (2-3) unit cells. Fig. 5.11 (b-c) show the evolution of the in-plane and out-of-plane lattice parameters across the thickness of the film. The in-plane lattice is the same as that of the SRO214 substrate which is what we expect for epitaxial films. The out-of-plane lattice are expanded from the bulk value for SRO113 in accordance with the compressive strain from the substrate. We also observe a rather larger expansion of the c-axis parameter right near the interface as compared to the rest of the film.

This expansion coincides with the region where we saw drop in Ru intensity in Fig. 5.11 (a). This seems contradictory at first. Ru-vacancies should lead to a rise in the formal valence of Ru atoms. An increase in the Ru formal valence should lead to a smaller ionic size of Ru and thus to smaller Ru-O interatomic distances. However, in their study of bulk polycrystalline SRO, Dabrowski *et al* found an expansion of lattice in the Ru-deficient samples[129]. It was suggested that the Sr atoms relax towards the vacant sites. In doing so, oxygen atom sublattice adjusts through oxygen octahedral rotation [i.e. (Ru-O-Ru) bond angle increases].

An expansion of c-axis accompanied by Ru-vacancy that is local near the interface paints a similar picture. It also suggests that suppression of oxygen octahedral tilts near the interface, facilitated by Ru-vacancies, lead to an enlarged c-axis parameter near the

interface. One unique aspect this study, is that both SRO113 and SRO214 have the same A - and B - site elements. Therefore, there are no complications associated with elemental intermixture during the growth. We observe that the Ru vacancies is not a global nature of PLD grown films as suggested by Siemons et al [45], rather a much local effect of oxygen octahedral matching near the interface.

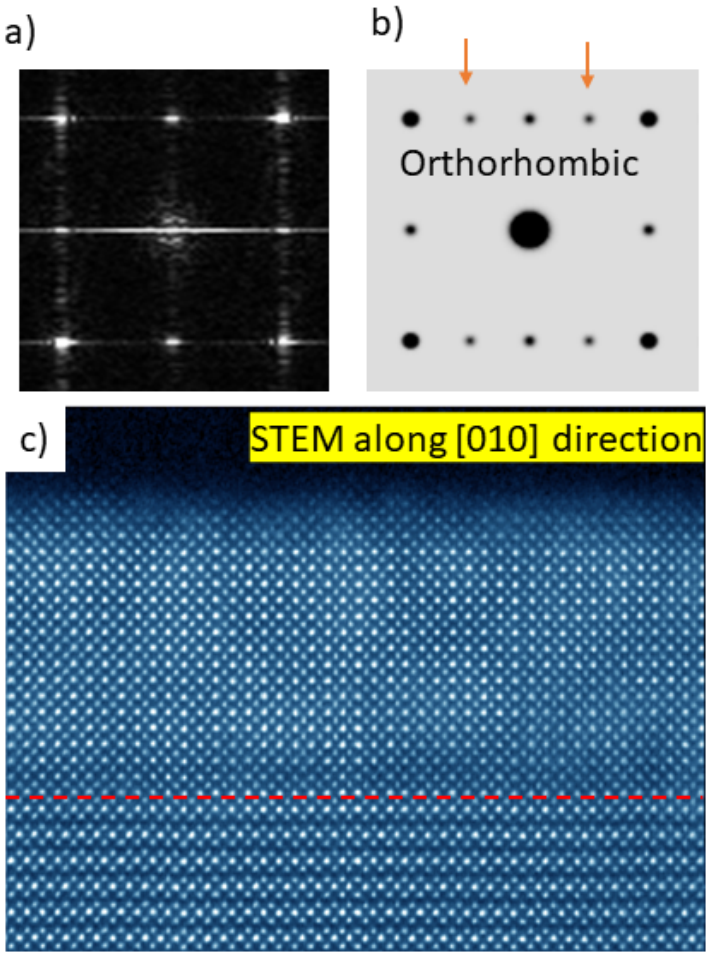

Figure 5.12. a) FFT pattern of ABF along [010] beam direction as shown in c). b) Simulated FFT for orthorhombic SRO.

Fig. 5.12 (a) shows the FFT pattern of an ABF image of the 15 u.c. SRO (c). For comparison, we have a simulated FFT pattern of an orthorhombic structure in Fig. 5.12 (b). The FFT of the STEM-ABF image does not have the half integer spots like the ones

indicated by red arrows in the simulation. This shows that the film has a tetragonal symmetry with suppressed oxygen octahedral tilts.

5.4.3. Anti-phase boundary using crystal symmetry

The symmetry mismatch at the step edge induces anti-phase boundary in SRO113/SRO214 thin films as well. The phenomenon is similar to our discussion in Section 5.3.3 for LSMO/SRO214. SRO113 has higher unit cell volume as compared to LSMO. Therefore, the substrate induced strain is larger in SRO113 on SRO214. Fig. 5.13 (a) shows the possible stacking near the step edge (step edge with the smallest height possible). The step height, (c/2) is slightly larger than (3/2 a) of the unit cell of SRO113. The difference, $\delta \approx$(0.38 Å-0.43 Å), however is smaller than that of LSMO/SRO214 films. The value of δ varies throughout the thickness of the film in the same manner as the c-lattice constant does. A locally reduced δ, due to lattice expansion observed in Fig. 5.13 (b) near the interface, could be significant in releasing some strain of the APBs. Further systematic study is required in this front. For a single APB, the boundary travels almost perpendicular to the interface and extends all the way to the surface as shown in Fig. 5.13 (b). We have shown that, while a perpendicular orientation of APB is favorable for a single boundary, this could change if we have two boundaries close enough to each other. A local minima in APB energy could occur, as the two boundaries travel towards each other and merge below the surface of the film [127]. A very similar situation of triangular APBs is observed in SRO113/SRO214 as shown in Fig. 5.13 (c).

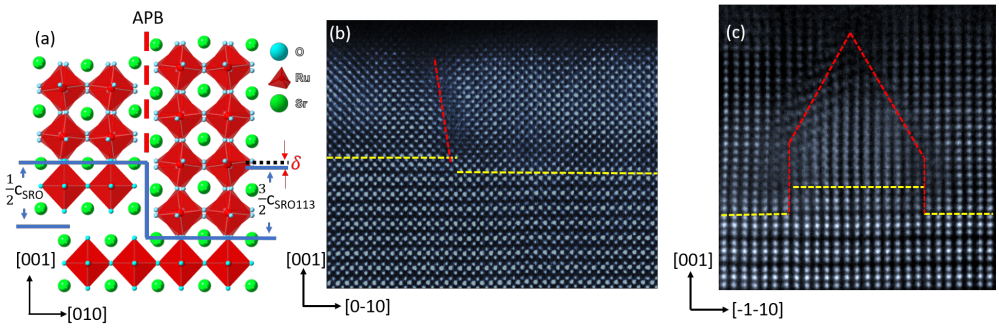

Figure 5.13. a) Schematics of various possible SRO113/SRO214 stackings near the step edge. The cyan line marks the interface which also includes a step of half the lattice constant along [001] direction of SRO214. The position of the anti-phase boundary is shown in red dashed line. δ marks the difference between the half the c-axis parameter of SRO214 and 3/2 of the c-axis parameter of SRO113. (b) HAADF image taken with beam along [100] direction. The interface is shown as yellow dashed line. Anti-phase boundary, red dashed line, is created originating at the step edge. (c) HAADF image of a region with two such step edges close to each other taken along [1-10]. Two APBs travel towards each other and merge below the surface.

5.5. Summary

We have successfully grown high quality LSMO thin films on SRO214 single crystal substrates with (113/214) stacking and a sharp interface. Comprehensive characterization with LEED, RHEED, STM and ARXPS confirms the successful growth with correct stoichiometry and ordered film surface. The surface reconstruction of the SRO214 substrate associated with the top layer RuO_6 rotational distortion disappears with the deposition of LSMO and results in a cubic-like perovskite film structure with (La/Sr) O layer termination. STEM results reveal a high quality, atomically sharp interface with single-layer minimal chemical intermixing and minimal lattice spacing deviation. We have also demonstrated an approach to create well defined 2D defects by the method of fabrication of heterointerfaces. By exploiting the natural differences in crystal symmetry between the substrate and the thin film material, we explored some properties of the defect boundaries. Being able to engineer 2D defects like these provide immense opportunities to explore fur-

ther research in 2D devices.

We have observed that the 15 u.c. SRO113/SRO214 film is strained in tetragonal structure. Our STEM/EELS analysis showed that the first 3-4 layers of film are found to be Ruthenium deficient, and the same Ru-deficient layers have larger out-of-plane lattice. Since, the atoms that make up the individual crystals are the same, the only difference is the symmetry of the structure and thus a setup like this provides an opportunity to study the effect of the lattice mismatch and the octahedral symmetry mismatch without the complications of the intermixture of ions near the interface. We observe that at the few layers near the interface, the presence of Ru vacancies facilitates the oxygen octahedral tilt suppression, leading to a larger out-of-plane lattice expansion. The oxygen octahedral tilt suppression is apparent from the tetragonal symmetry revealed by the FFT of ABF image taken from the film. This out-of-plane lattice expansion is in addition to the usual epitaxial strain mismatch induced lattice expansion of the film and is mostly limited to a few layers near the interface.

PLD grown SRO films are expected to be Ru deficient. We find that the Ru deficiency has a more local nature in PLD grown films. Since the growth of films happen at a rather large temperature of 700 °C and a high oxygen environment, the volatility of Ru to such extreme conditions should also be considered. Ru-vacancies and the structural anomaly near the interface is particularly important to consider when exploring the properties of ultrathin SRO films grown with PLD.

Chapter 6. Summary and Outlook

In this thesis, we focused on the structural characterization and the magnetic as well as transport properties of $SrRuO_3$ thin films. By varying the crystallographic orientation of growth and film thickness, we made a systematic effort to understand the changes in magnetic and electronic behavior due to the changing symmetry of the crystal field and reduced dimensionality in SRO films.

By combining surface-sensitive *in-situ* LEED measurements with *ex-situ* STEM techniques, we observed signatures of crystallographic domains of orthorhombic distorted structure in extremely thin (upto 1 u.c.) SRO(001) films. As revealed by STEM in thicker films, these structural domains are in-fact 90° rotated $a^+a^-c^-$ structure of SRO. From magneto-transport study of a thicker $\sim$ 21 u.c. SRO(001), we observed indications of a second phase, with varying coercivity, suggesting multiple spin-conduction channels. Temperature evolution of anomalous Hall resistivity was properly described with a two channel model.

We optimized the growth of SRO(111) films. The thermodynamics of growth of SRO film on STO(111) polar surface is found to be different from the SRO film growth on STO(001) surface. A growth mode that changes with the change in electrostatics of the surface was observed. After a few layers of growth in 2D layer-by-layer mode, the surface roughened and the growth mode changed to 3D island mode in response to the increasing electrostatic potential. As the growth proceeded the SRO turns metallic and the 2D layer-by-layer growth mode resumes. We observed that there is a rather narrow window to obtain a good growth.

SRO(111) films consists of significantly less structural domains, as compared to the

SRO(001) films as observed in STEM study. This apparent single domain landscape has consequences on the properties measured. The better transport properties as evidenced by lower residual resistivity and enhanced Curie temperature is observed in SRO(111) films. We also observed a reduction of spin-dimensionality and the suppression of low temperature spin-wave excitations (magnons) in SRO(111) films. The magnetization vs temperature is found to vary more like T^2 rather than $T^{3/2}$ expected for spin waves.

Atomically resolved structural studies reveal a high quality crystal thin film with a sharp interface. We observed the presence of Ru vacancies near the surface, accompanied by a reduced out-of-plane lattice parameter. We believe the vacancies aid in the surface energy minimization of the polar surface. This localized Ru-vacancy at the surface needs further examination. Core level Ru peaks can be studied by X-ray photoelectron spectroscopy at a larger emission angle to verify the enhanced Ru formal valence near the surface.

Thickness dependent study in both (001) and (111) crystallographic orientations showed very similar transport behavior. The lowest thickness insulating yet ferromagnetic samples show variable range hopping type conduction modified by strong coulomb correlations. With increasing thickness, they become metallic with low temperature corrections due to weak localization. We observed the non-linearity of $\rho(T)$ in the temperature range 30K - 80K increases with decreasing thickness, possibly due to increasing disorder.

Magnetoresistance in SRO ultrathin films show contributions from both the ferromagnetic fluctations near T_C and from weak localization at lower temperatures. The contribution from weak localization becomes larger with decreasing thickness. For thicker films, in [111] crystallographic orientation of the substrate, we observed an additional pos-

itive contribution to the magnetoresistance at temperatures lower than the Fermi temperature, that did not seem to saturate. We believe, the apparent single domain nature of structure, along with the low residual resistivity in SRO(111) samples enhances the quantum effects on the magnetoresistance behavior. Since, we observed the residual resistivity decreases with increasing sample thickness, magneto-transport behavior of larger thickness SRO(111) samples should be studied in order to gain further insight into the rich physics of SRO.

We observed deviations in the thickness dependent changes to the ferromagnetic transition temperature, T_C in SRO(001) as compared with SRO(111) films. We need insight from theoretical studies to understand the effect of changing local symmetry in reduced thickness to understand it's effect on magnetism in SRO films.

Our study of structure on the 15 u.c. $SrRuO_3/Sr_2RuO_4$ revealed a tetragonal structure owing to a large compressive biaxial strain ($\sim 1.5\%$). We observed Ru-vacancies localized in the interface region, in absence of any intermixture, possibly to account for the changing oxygen octahedral geometry. Further information about the oxygen displacement near the interface are required to verify this behavior.

Appendix. Permissions

American Physical Society Reuse and Permissions License

13-Aug-2021

This license agreement between the American Physical Society ("APS") and Prahald Siwakoti ("You") consists of your license details and the terms and conditions provided by the American Physical Society and SciPris.

Licensed Content Information

License Number:	**RNP/21/AUG/043356**
License date:	13-Aug-2021
DOI:	10.1103/PhysRevMaterials.2.104407
Title:	Coherent growth of oxide films on a cleaved layered metal oxide substrate
Author:	Prahald Siwakoti et al.
Publication:	Physical Review Materials
Publisher:	American Physical Society
Cost:	USD $ 0.00

Request Details

Does your reuse require significant modifications: No

Specify intended distribution locations:	United States
Reuse Category:	Reuse in a thesis/dissertation
Requestor Type:	Student
Items for Reuse:	Whole Article
Format for Reuse:	Electronic

Information about New Publication:

University/Publisher:	Louisiana State University
Title of dissertation/thesis:	Effects of structure, crystallographic orientation, and dimensionality on emergent properties of transition metal oxide thin films
Author(s):	Prahald Siwakoti
Expected completion date:	Aug. 2021

License Requestor Information

Name:	Prahald Siwakoti
Affiliation:	Individual
Email Id:	prasiwakoti@gmail.com
Country:	United States

American Physical Society
Reuse and Permissions License

TERMS AND CONDITIONS

The American Physical Society (APS) is pleased to grant the Requestor of this license a non-exclusive, non-transferable permission, limited to Electronic format, provided all criteria outlined below are followed.

1. You must also obtain permission from at least one of the lead authors for each separate work, if you haven't done so already. The author's name and affiliation can be found on the first page of the published Article.
2. For electronic format permissions, Requestor agrees to provide a hyperlink from the reprinted APS material using the source material's DOI on the web page where the work appears. The hyperlink should use the standard DOI resolution URL, http://dx.doi.org/{DOI}. The hyperlink may be embedded in the copyright credit line.
3. For print format permissions, Requestor agrees to print the required copyright credit line on the first page where the material appears: "Reprinted (abstract/excerpt/figure) with permission from [(FULL REFERENCE CITAT ION) as follows: Author's Names, APS Journal Title, Volume Number, Page Number and Year of Publication.] Copyright (YEAR) by the American Physical Society."
4. Permission granted in this license is for a one-time use and does not include permission for any future editions, updates, databases, formats or other matters. Permission must be sought for any additional use.
5. Use of the material does not and must not imply any endorsement by APS.
6. APS does not imply, purport or intend to grant permission to reuse materials to which it does not hold copyright. It is the requestor's sole responsibility to ensure the licensed material is original to APS and does not contain the copyright of another entity, and that the copyright notice of the figure, photograph, cover or table does not indicate it was reprinted by APS with permission from another source.
7. The permission granted herein is personal to the Requestor for the use specified and is not transferable or assignable without express written permission of APS. This license may not be amended except in writing by APS.
8. You may not alter, edit or modify the material in any manner.
9. You may translate the materials only when translation rights have been granted.
10. APS is not responsible for any errors or omissions due to translation.
11. You may not use the material for promotional, sales, advertising or marketing purposes.
12. The foregoing license shall not take effect unless and until APS or its agent, Aptara, receives payment in full in accordance with Aptara Billing and Payment Terms and Conditions, which are incorporated herein by reference.
13. Should the terms of this license be violated at any time, APS or Aptara may revoke the license with no refund to you and seek relief to the fullest extent of the laws of the USA. Official written notice will be made using the contact information provided with the permission request. Failure to receive such notice will not nullify revocation of the permission.
14. APS reserves all rights not specifically granted herein.
15. This document, including the Aptara Billing and Payment Terms and Conditions, shall be the entire agreement between the parties relating to the subject matter hereof.

Designing antiphase boundaries by atomic control of heterointerfaces

Zhen Wang[a,b], Hangwen Guo[a,1], Shuai Shao[c], Mohammad Saghayezhian[a], Jun Li[b], Rosalba Fittipaldi[d], Antonio Vecchione[d], Prahald Siwakoti[a], Yimei Zhu[b], Jiandi Zhang[a], and E. W. Plummer[a,1]

[a]Department of Physics & Astronomy, Louisiana State University, Baton Rouge, LA 70803; [b]Condensed Matter Physics & Materials Science Department, Brookhaven National Laboratory, Upton, NY 11973; [c]Department of Mechanical & Industrial Engineering, Louisiana State University, Baton Rouge, LA 70803; and [d]Consiglio Nazionale Delle Ricerche-Superconducting and Other Innovative Materials and Devices Institute (SPIN), Dipartimento di Fisica, Università di Salerno, 132 - 84084 Fisciano, Italy

Contributed by E. W. Plummer, July 10, 2018 (sent for review May 22, 2018; reviewed by Ramamoorthy Ramesh and Frans Spaepen)

Extended defects are known to have critical influences in achieving desired material performance. However, the nature of extended defect generation is highly elusive due to the presence of multiple nucleation mechanisms with close energetics. A strategy to design extended defects in a simple and clean way is thus highly desirable to advance the understanding of their role, improve material quality, and serve as a unique playground to discover new phenomena. In this work, we report an approach to create planar extended defects—antiphase boundaries (APB)—with well-defined origins via the combination of advanced growth, atomic-resolved electron microscopy, first-principals calculations, and defect theory. In $La_{2/3}Sr_{1/3}MnO_3$ thin film grown on Sr_2RuO_4 substrate, APBs in the film naturally nucleate at the step on the substrate/film interface. For a single step, the generated APBs tend to be nearly perpendicular to the interface and propragate toward the film surface. Interestingly, when two steps are close to each other, two corresponding APBs communicate and merge together, forming a unique triangle-shaped defect domain boundary. Such behavior has been ascribed, in general, to the minimization of the surface energy of the APB. Atomic-resolved electron microscopy shows that these APBs have an intriguing antipolar structure phase, thus having the potential as a general recipe to achieve ferroelectric-like domain walls for high-density nonvolatile memory.

antiphase boundary | extended defect nucleation | interfaces | electron microscopy | theory

Defects often hold the key to discovering numerous emergent functionalities in thin-film technology (1–3). While the existence of point defects such as impurities and vacancies is mainly governed by the second law of thermodynamics (4, 5), extended defects are more complicated to understand due to their higher dimensionality (line, surface, and volumetric) and nonequilibrium characteristics (6, 7). Among the extended defects, antiphase boundary (APB), a planar defect featuring a half-unit-cell shift of registry with respect to adjacent regions (8), receives special attention. For example, in group III–V semiconductors, the formation of APBs hinders the growth of high-quality wafers in achieving high-performance solar cells and nonlinear optical integrations (9, 10). APB is also known to be responsible for the anomalous magnetoresistive behavior in Fe_3O_4 and magnetic Heusler alloys, serving as a critical factor for spintronics and memory device applications (11–14). Thus, it is desirable to design and control the formation and nucleation process of APBs to explore new functionalities and achieve high performance in devices.

The formation and nucleation process of APBs remains highly elusive, largely because APB can be induced by multiple mechanisms and each has its own characteristics. In bulk compounds, the APB is extremely sensitive to growth condition, crystal symmetry, and lattice transformation in which a general tuning knob to control APB generation is impossible (15–17). Alternatively, thin-film heterostructures provide a platform to manipulate APB formation and nucleation. Large in-plane lattice mismatch between films and substrates is one of the most common mechanisms to nucleate APBs (18–21). To relieve the large strain energy from substrate, APBs are formed with random locations and morphology, and thus it is difficult to predict their locations and growth direction. Another mechanism to generate APBs is by off-stoichiometry growth to create stacking faults and different phases (8, 22, 23), but the poor controllability of local stoichiometry often leads to irregular and random intergrowth of various types of APBs. In contrast, vicinal substrate surface plays an intriguing role in APB nucleation. The difference in crystallographic symmetry between the film and substrate can allow the APB to nucleate at the step between neighboring substrate terraces (8, 9). Unfortunately, such a nucleation process is often intertwined with the aforementioned mechanisms due to their close energetics, thus leading to the coexistence of a wide variety of irregular and multidirectional APB morphology (8, 10, 13). These complexities make it extremely difficult to understand the nature and further control the exact location and nucleation process of APBs, clouding their impact on material's functional properties. A clean strategy that can design APB with well-defined origin, location, and nucleation mechanism is of great interest. It can further facilitate the defect engineering toward high-performance functional materials.

Significance

The mechanical and transport properties of every material are intimately coupled to the generation and formation of defects. In many systems, the nucleation process of defects is highly unpredictable due to the multiple coexisting nucleation mechanisms. A strategy to design and manipulate defect nucleation and formation can improve our understanding and in principle lead to the ability to control performance. Here we present a simple approach of designing 2D defects—named antiphase boundaries—using an atomic-controlled high-quality interface. These defects have a well-defined origin, location, and nucleation mechanism. Via advanced synthesis technology, atomically resolved electron microscopy, and theory, we reveal that these defects display distinctive properties such as physical merging and antipolar structural phases to potentially achieve memory devices.

Author contributions: Z.W., H.G., J.Z., and E.W.P. designed research; Z.W., H.G., S.S., M.S., J.L., R.F., A.V., P.S., Y.Z., and J.Z. performed research; R.F. and A.V. contributed new reagents/analytic tools; Z.W., H.G., S.S., M.S., J.L., Y.Z., J.Z., and E.W.P. analyzed data; and Z.W., H.G., S.S., M.S., Y.Z., J.Z., and E.W.P. wrote the paper.

Reviewers: R.R., University of California, Berkeley; and F.S., Harvard University.

The authors declare no conflict of interest.

See Commentary on page 9344.

[1]To whom correspondence may be addressed. Email: hangwenguo@fudan.edu.cn or wplummer@phys.lsu.edu.

This article contains supporting information online at www.pnas.org/lookup/suppl/doi:10.1073/pnas.1808812115/-/DCSupplemental.

Published online August 13, 2018.

Abrupt orthorhombic relaxation in compressively strained ultra-thin $SrRuO_3$ films

Prahald Siwakoti[1], Zhen Wang[1,2], Mohammad Saghayezhian[1], David Howe[1], Zeeshan Ali[1], Yimei Zhu[2], Jiandi Zhang[1]

[1]*Department of Physics and Astronomy, Louisiana State University, Baton Rouge, LA 70803, USA*

[2]*Department of Energy Science and Technology, Brookhaven National Laboratory, Upton, NY 11973, USA*

Abstract

Lattice structure can dictate electronic and magnetic properties of a material. Especially, reconstruction at a surface or heterointerface can create properties that are fundamentally different from those of the corresponding bulk material. We have investigated the lattice structure on the surface and in the thin films of epitaxial $SrRuO_3$ with the film thickness up to 22 pseudo-cubic unit cells (u.c.), using the combination of surface sensitive low energy electron diffraction and bulk sensitive scanning transmission electron microscopy. Our analysis indicates that, in contrast to many perovskite oxides, the RuO_6 tilt and rotational distortions appear even in single unit cell $SrRuO_3$ thin films on cubic $SrTiO_3$, while the full relaxation to the bulk-like orthorhombic structure takes 3-4 u.c. from the interface for thicker films. Yet the TiO_6 octahedra of the substrate near the interface with $SrRuO_3$ films show no sign of distortion, unlike those near the interface with $CaRuO_3$ films. Two orthogonal in-plane rotated structural domains are identified. These structural distortions are essential for the nature of the thickness dependent transport and magnetism in ultrathin films.

Tailoring the lattice mismatch strain in epitaxial films and heterostructures has been used as a tool to stabilize novel phases otherwise non-existent in the bulk [1], to enhance the physical properties such as superconductivity [2,3], ferroelectricity [4], and ferromagnetism [5,6], as well as to manipulate magnetic anisotropy [7], and metal-insulator transitions [8–11]. The effect of strain mismatch on the electronic and magnetic properties of $SrRuO_3$ (SRO) thin films has been extensively studied for decades [12–14]. Bulk SRO at room temperature crystallizes in orthorhombic structure with *Pbnm* (No. 62) symmetry with lattice parameters a = 5.5670 Å, b = 5.5304 Å and c = 7.8446 Å. An orthorhombic unit cell is produced by rotations of RuO_6 octahedra from the ideal cubic structure. Such rotations in SRO produce a distorted pseudo-cubic perovskite structure with a pseudo-cubic lattice constant of 3.93 Å [15,16]. In Glazer notation [17], it can be described with $a^+b^-b^-$ tilt system (#10) which is defined by in-phase rotation of the neighboring octahedra about the $[100]_p$ pseudo-cubic axis (hereafter denoted with a subscript "p") and mutually equivalent out-of-phase rotation about $[010]_p$ and $[001]_p$ axes, respectively. When grown as thin films, the interfacial octahedral mismatch between substrate and film creates a coupling effect. The accommodation of the octahedral symmetry mismatch is achieved through rigid rotations

Bibliography

[1] A. M. Glazer, Acta Crystallographica Section B: Structural Crystallography and Crystal Chemistry **28**, 3384 (1972).

[2] A. Glazer, Acta Crystallographica Section A: Crystal Physics, Diffraction, Theoretical and General Crystallography **31**, 756 (1975).

[3] A. Vailionis, H. Boschker, W. Siemons, E. P. Houwman, D. H. Blank, G. Rijnders, and G. Koster, Physical Review B **83**, 064101 (2011).

[4] K. Ahadi, L. Galletti, Y. Li, S. Salmani-Rezaie, W. Wu, and S. Stemmer, Science advances **5**, eaaw0120 (2019).

[5] K. J. Choi, M. Biegalski, Y. Li, A. Sharan, J. Schubert, R. Uecker, P. Reiche, Y. Chen, X. Pan, V. Gopalan, et al., Science **306**, 1005 (2004).

[6] H. Guo, Z. Wang, S. Dong, S. Ghosh, M. Saghayezhian, L. Chen, Y. Weng, A. Herklotz, T. Z. Ward, R. Jin, et al., Proceedings of the National Academy of Sciences **114**, E5062 (2017).

[7] D. Kan, R. Aso, R. Sato, M. Haruta, H. Kurata, and Y. Shimakawa, Nature materials **15**, 432 (2016).

[8] J. Cao and J. Wu, Materials Science and Engineering: R: Reports **71**, 35 (2011).

[9] J. P. Ruf, H. Paik, N. J. Schreiber, H. P. Nair, L. Miao, J. K. Kawasaki, J. N. Nelson, B. D. Faeth, Y. Lee, B. H. Goodge, et al., Nature Communications **12**, 1 (2021).

[10] D. Meng, H. Guo, Z. Cui, C. Ma, J. Zhao, J. Lu, H. Xu, Z. Wang, X. Hu, Z. Fu, et al., Proceedings of the National Academy of Sciences **115**, 2873 (2018).

[11] J. B. Goodenough, Physical Review **100**, 564 (1955).

[12] P. Anderson, Physical Review **79**, 350 (1950).

[13] A. Boris, Y. Matiks, E. Benckiser, A. Frano, P. Popovich, V. Hinkov, P. Wochner, M. Castro-Colin, E. Detemple, V. K. Malik, et al., Science **332**, 937 (2011).

[14] A. Ohtomo and H. Hwang, Nature **427**, 423 (2004).

[15] A. Brinkman, M. Huijben, M. Van Zalk, J. Huijben, U. Zeitler, J. Maan, W. G. van der Wiel, G. Rijnders, D. H. Blank, and H. Hilgenkamp, Nature materials **6**, 493 (2007).

[16] N. Reyren, S. Thiel, A. Caviglia, L. F. Kourkoutis, G. Hammerl, C. Richter, C. W. Schneider, T. Kopp, A.-S. Rüetschi, D. Jaccard, et al., Science **317**, 1196 (2007).

[17] A. Caviglia, M. Gabay, S. Gariglio, N. Reyren, C. Cancellieri, and J.-M. Triscone, Physical review letters **104**, 126803 (2010).

[18] J. Chakhalian, A. Millis, and J. Rondinelli, Nature materials **11**, 92 (2012).

[19] N. Nakagawa, H. Y. Hwang, and D. A. Muller, Nature materials **5**, 204 (2006).

[20] D. Xiao, W. Zhu, Y. Ran, N. Nagaosa, and S. Okamoto, Nature communications **2**, 1 (2011).

[21] L. Si, O. Janson, G. Li, Z. Zhong, Z. Liao, G. Koster, and K. Held, Physical review letters **119**, 026402 (2017).

[22] G. A. Fiete and A. Rüegg, Journal of Applied Physics **117**, 172602 (2015).

[23] M. Moreau, A. Marthinsen, S. M. Selbach, and T. Tybell, Physical Review B **95**, 064109 (2017).

[24] T. Kim, D. Puggioni, Y. Yuan, L. Xie, H. Zhou, N. Campbell, P. Ryan, Y. Choi, J.-

W. Kim, J. Patzner, et al., Nature **533**, 68 (2016).

[25] I. Hallsteinsen, M. Moreau, A. Grutter, M. Nord, P.-E. Vullum, D. A. Gilbert, T. Bolstad, J. Grepstad, R. Holmestad, S. Selbach, et al., Physical Review B **94**, 201115 (2016).

[26] M. Moreau, S. M. Selbach, and T. Tybell, Journal of Applied Physics **124**, 185301 (2018).

[27] J. Seidel, L. W. Martin, Q. He, Q. Zhan, Y.-H. Chu, A. Rother, M. Hawkridge, P. Maksymovych, P. Yu, M. e. Gajek, et al., Nature materials **8**, 229 (2009).

[28] P. Maksymovych, J. Seidel, Y. H. Chu, P. Wu, A. P. Baddorf, L.-Q. Chen, S. V. Kalinin, and R. Ramesh, Nano letters **11**, 1906 (2011).

[29] T. Matsumoto, R. Ishikawa, T. Tohei, H. Kimura, Q. Yao, H. Zhao, X. Wang, D. Chen, Z. Cheng, N. Shibata, et al., Nano letters **13**, 4594 (2013).

[30] R. J. Tilley, *Defects in solids*, vol. 4 (John Wiley & Sons, 2008).

[31] M. Saghayezhian, Z. Wang, D. Howe, P. Siwakoti, E. Plummer, Y. Zhu, and J. Zhang, Journal of Physics: Condensed Matter **33**, 275003 (2021).

[32] C. Jones, P. Battle, P. Lightfoot, and W. Harrison, Acta Crystallographica Section C: Crystal Structure Communications **45**, 365 (1989).

[33] S. Pang, Applied Microscopy **47**, 187 (2017).

[34] G. Koster, L. Klein, W. Siemons, G. Rijnders, J. S. Dodge, C.-B. Eom, D. H. Blank, and M. R. Beasley, Reviews of Modern Physics **84**, 253 (2012).

[35] P. Allen, H. Berger, O. Chauvet, L. Forro, T. Jarlborg, A. Junod, B. Revaz, and G. Santi, Physical Review B **53**, 4393 (1996).

[36] D. J. Singh, Journal of applied physics **79**, 4818 (1996).

[37] S. Bushmeleva, V. Y. Pomjakushin, E. Pomjakushina, D. Sheptyakov, and A. Balagurov, Journal of magnetism and magnetic materials **305**, 491 (2006).

[38] D. Shai, C. Adamo, D. Shen, C. M. Brooks, J. Harter, E. J. Monkman, B. Burganov, D. G. Schlom, and K. M. Shen, Physical review letters **110**, 087004 (2013).

[39] J. Dodge, E. Kulatov, L. Klein, C. H. Ahn, J. Reiner, L. Mieville, T. Geballe, M. Beasley, A. Kapitulnik, H. Ohta, et al., Physical Review B **60**, R6987 (1999).

[40] J.-G. Cheng, J.-S. Zhou, J. Goodenough, and C.-Q. Jin, Physical Review B **85**, 184430 (2012).

[41] L. Klein, J. Dodge, C. Ahn, J. Reiner, L. Mieville, T. Geballe, M. Beasley, and A. Kapitulnik, Journal of Physics: Condensed Matter **8**, 10111 (1996).

[42] M. E. Fisher and J. Langer, Physical Review Letters **20**, 665 (1968).

[43] W. Lu, P. Yang, W. D. Song, G. M. Chow, and J. S. Chen, Physical Review B **88**, 214115 (2013).

[44] W. Lu, W. Dong Song, K. He, J. Chai, C.-J. Sun, G.-M. Chow, and J.-S. Chen, Journal of Applied Physics **113**, 063901 (2013).

[45] W. Siemons, G. Koster, A. Vailionis, H. Yamamoto, D. H. Blank, and M. R. Beasley, Physical Review B **76**, 075126 (2007).

[46] C.-B. Eom, R. Cava, R. Fleming, J. M. Phillips, J. Marshall, J. Hsu, J. Krajewski, W. Peck, et al., Science **258**, 1766 (1992).

[47] D. Toyota, I. Ohkubo, H. Kumigashira, M. Oshima, T. Ohnishi, M. Lippmaa, M. Takizawa, A. Fujimori, K. Ono, M. Kawasaki, et al., Applied Physics Letters **87**,

162508 (2005).

[48] Y. J. Chang, C. H. Kim, S.-H. Phark, Y. Kim, J. Yu, and T. Noh, Physical review letters **103**, 057201 (2009).

[49] J. Xia, W. Siemons, G. Koster, M. Beasley, and A. Kapitulnik, Physical Review B **79**, 140407 (2009).

[50] K. Kim, J. Lee, T. Noh, S. Lee, and K. Char, Physical Review B **71**, 125104 (2005).

[51] H. Yang, Z. Liu, C. Fan, Q. Yao, P. Xiang, K. Zhang, M. Li, H. Li, J. Liu, D. Shen, et al., Physical Review B **93**, 121102 (2016).

[52] X. Shen, X. Qiu, D. Su, S. Zhou, A. Li, and D. Wu, Journal of Applied Physics **117**, 015307 (2015).

[53] H. Ryu, Y. Ishida, B. Kim, J. R. Kim, W. J. Kim, Y. Kohama, S. Imajo, Z. Yang, W. Kyung, S. Hahn, et al., Physical Review B **102**, 041102 (2020).

[54] P. Mahadevan, F. Aryasetiawan, A. Janotti, and T. Sasaki, Physical Review B **80**, 035106 (2009).

[55] S. Kang, Y. Tseng, B. H. Kim, S. Yun, B. Sohn, B. Kim, D. McNally, E. Paris, C. H. Kim, C. Kim, et al., Physical Review B **99**, 045113 (2019).

[56] N. Nagaosa, J. Sinova, S. Onoda, A. H. MacDonald, and N. P. Ong, Reviews of modern physics **82**, 1539 (2010).

[57] R. Karplus and J. Luttinger, Physical Review **95**, 1154 (1954).

[58] T. Jungwirth, Q. Niu, and A. MacDonald, Physical review letters **88**, 207208 (2002).

[59] M. Onoda and N. Nagaosa, Journal of the Physical Society of Japan **71**, 19 (2002).

[60] M. Izumi, K. Nakazawa, Y. Bando, Y. Yoneda, and H. Terauchi, Journal of the Physical Society of Japan **66**, 3893 (1997).

[61] Z. Fang, N. Nagaosa, K. S. Takahashi, A. Asamitsu, R. Mathieu, T. Ogasawara, H. Yamada, M. Kawasaki, Y. Tokura, and K. Terakura, Science **302**, 92 (2003).

[62] J. Matsuno, N. Ogawa, K. Yasuda, F. Kagawa, W. Koshibae, N. Nagaosa, Y. Tokura, and M. Kawasaki, Science advances **2**, e1600304 (2016).

[63] L. Wang, Q. Feng, Y. Kim, R. Kim, K. H. Lee, S. D. Pollard, Y. J. Shin, H. Zhou, W. Peng, D. Lee, et al., Nature materials **17**, 1087 (2018).

[64] Y. Gu, Y.-W. Wei, K. Xu, H. Zhang, F. Wang, F. Li, M. S. Saleem, C.-Z. Chang, J. Sun, C. Song, et al., Journal of Physics D: Applied Physics **52**, 404001 (2019).

[65] Q. Qin, L. Liu, W. Lin, X. Shu, Q. Xie, Z. Lim, C. Li, S. He, G. M. Chow, and J. Chen, Advanced Materials **31**, 1807008 (2019).

[66] D. Kan, T. Moriyama, K. Kobayashi, and Y. Shimakawa, Physical Review B **98**, 180408 (2018).

[67] D. Kan and Y. Shimakawa, physica status solidi (b) **255**, 1800175 (2018).

[68] L. Wang, Q. Feng, H. G. Lee, E. K. Ko, Q. Lu, and T. W. Noh, Nano letters **20**, 2468 (2020).

[69] G. Charlton, S. Brennan, C. Muryn, R. McGrath, D. Norman, T. Turner, and G. Thornton, Surface Science **457**, L376 (2000).

[70] T. Hikita, T. Hanada, M. Kudo, and M. Kawai, Surface science **287**, 377 (1993).

[71] A. Ikeda, T. Nishimura, T. Morishita, and Y. Kido, Surface science **433**, 520 (1999).

[72] M. Saghayezhian, S. Rezaei Sani, J. Zhang, and E. Plummer, The Journal of Physical Chemistry C **123**, 8086 (2018).

[73] M. Kawasaki, K. Takahashi, T. Maeda, R. Tsuchiya, M. Shinohara, O. Ishiyama, T. Yonezawa, M. Yoshimoto, and H. Koinuma, Science **266**, 1540 (1994).

[74] A. Biswas, P. Rossen, C.-H. Yang, W. Siemons, M.-H. Jung, I. Yang, R. Ramesh, and Y. Jeong, Applied Physics Letters **98**, 051904 (2011).

[75] G. Koster, B. L. Kropman, G. J. Rijnders, D. H. Blank, and H. Rogalla, Applied Physics Letters **73**, 2920 (1998).

[76] M. Saghayezhian, Ph.D. thesis (2017).

[77] D. L. Smith and D. W. Hoffman, Physics Today **49**, 60 (1996).

[78] D. Chrisey and G. Hubler, *Pulsed Laser Deposition of Thin Films* (Wiley, 1994), ISBN 9780471592181, URL `https://books.google.com/books?id=0Oh_QgAACAAJ`.

[79] J. Choi, C.-B. Eom, G. Rijnders, H. Rogalla, and D. H. Blank, Applied physics letters **79**, 1447 (2001).

[80] G. Rijnders, D. H. Blank, J. Choi, and C.-B. Eom, Applied physics letters **84**, 505 (2004).

[81] C. Lichtensteiger, Journal of applied crystallography **51**, 1745 (2018).

[82] A. Tselev, P. Ganesh, L. Qiao, W. Siemons, Z. Gai, M. D. Biegalski, A. P. Baddorf, and S. V. Kalinin, ACS nano **7**, 4403 (2013).

[83] K. Fuchigami, Z. Gai, T. Z. Ward, L. Yin, P. C. Snijders, E. W. Plummer, and J. Shen, Physical review letters **102**, 066104 (2009).

[84] J. Shin, A. Y. Borisevich, V. Meunier, J. Zhou, E. W. Plummer, S. V. Kalinin, and A. P. Baddorf, ACS nano **4**, 4190 (2010).

[85] R. Matzdorf, Z. Fang, J. Zhang, T. Kimura, Y. Tokura, K. Terakura, E. Plummer, et al., Science **289**, 746 (2000).

[86] B. Hu, G. T. McCandless, M. Menard, V. Nascimento, J. Y. Chan, E. Plummer, and R. Jin, Physical Review B **81**, 184104 (2010).

[87] S. Thomas, B. Kuiper, J. Hu, J. Smit, Z. Liao, Z. Zhong, G. Rijnders, A. Vailionis, R. Wu, G. Koster, et al., Physical review letters **119**, 177203 (2017).

[88] L. Chen, Z. Wang, G. Wang, H. Guo, M. Saghayezhian, Z. Liao, Y. Zhu, E. Plummer, and J. Zhang, Physical Review Materials **3**, 044407 (2019).

[89] Z. Wang, J. Tao, L. Yu, H. Guo, L. Chen, M.-G. Han, L. Wu, H. Xin, K. Kisslinger, E. Plummer, et al., Physical Review B **94**, 155307 (2016).

[90] L. Klein, Y. Kats, A. Marshall, J. Reiner, T. Geballe, M. Beasley, and A. Kapitulnik, Physical review letters **84**, 6090 (2000).

[91] S. Zhang, Y. Liu, L. Collins-McIntyre, T. Hesjedal, J. Zhang, S. Wang, and G. Yu, Scientific reports **3**, 1 (2013).

[92] T. van Thiel, D. Groenendijk, and A. Caviglia, Journal of Physics: Materials **3**, 025005 (2020).

[93] A. Grutter, F. Wong, E. Arenholz, M. Liberati, A. Vailionis, and Y. Suzuki, Applied Physics Letters **96**, 082509 (2010).

[94] B. Lee, O.-U. Kwon, R. H. Shin, W. Jo, and C. U. Jung, Nanoscale research letters **9**, 1 (2014).

[95] A. Rastogi, M. Brahlek, J. M. Ok, Z. Liao, C. Sohn, S. Feldman, and H. N. Lee,

APL Materials **7**, 091106 (2019).

[96] H. I. Seo, S. Woo, J. Kim, S. G. Jeong, T. Park, and W. S. Choi, Physical Review B **103**, 045104 (2021).

[97] S. Okamoto and D. Xiao, Journal of the Physical Society of Japan **87**, 041006 (2018).

[98] S. Woo, H. Choi, S. Kang, J. Lee, A. David, W. Prellier, Y. Kim, H. Y. Kim, and W. S. Choi, Applied Surface Science **499**, 143924 (2020).

[99] C. Noguera, Journal of Physics: Condensed Matter **12**, R367 (2000).

[100] J. Goniakowski, C. Noguera, and L. Giordano, Physical review letters **98**, 205701 (2007).

[101] J. Chang, Y.-S. Park, J.-W. Lee, and S.-K. Kim, Journal of crystal growth **311**, 3771 (2009).

[102] D. Pesquera, X. Marti, V. Holy, R. Bachelet, G. Herranz, and J. Fontcuberta, Applied Physics Letters **99**, 221901 (2011).

[103] H.-T. Jeng, S.-H. Lin, and C.-S. Hsue, Physical review letters **97**, 067002 (2006).

[104] J. M. Rondinelli, N. M. Caffrey, S. Sanvito, and N. A. Spaldin, Physical Review B **78**, 155107 (2008).

[105] B. Kim and B. Min, Physical Review B **89**, 195411 (2014).

[106] J. Okamoto, T. Okane, Y. Saitoh, K. Terai, S.-I. Fujimori, Y. Muramatsu, K. Yoshii, K. Mamiya, T. Koide, A. Fujimori, et al., Physical Review B **76**, 184441 (2007).

[107] A. Grutter, F. Wong, E. Arenholz, A. Vailionis, and Y. Suzuki, Physical Review B

85, 134429 (2012).

[108] A. Zayak, X. Huang, J. Neaton, and K. M. Rabe, Physical Review B **77**, 214410 (2008).

[109] S. Agrestini, Z. Hu, C.-Y. Kuo, M. Haverkort, K.-T. Ko, N. Hollmann, Q. Liu, E. Pellegrin, M. Valvidares, J. Herrero-Martin, et al., Physical Review B **91**, 075127 (2015).

[110] L. Klein, J. Dodge, T. Geballe, A. Kapitulnik, A. Marshall, L. Antognazza, and K. Char, Applied physics letters **66**, 2427 (1995).

[111] G. J. Snyder, arXiv preprint arXiv:1904.12193 (2019).

[112] S. Blundell, *Magnetism in Condensed Matter* (Oxford University Press, 2001).

[113] J. Bass, W. P. Pratt Jr, and P. A. Schroeder, Reviews of modern physics **62**, 645 (1990).

[114] G. Herranz, V. Laukhin, F. Sánchez, P. Levy, C. Ferrater, M. García-Cuenca, M. Varela, and J. Fontcuberta, Physical Review B **77**, 165114 (2008).

[115] L. Wang, H.-E. Horng, and H.-C. Yang, Physical Review B **70**, 014433 (2004).

[116] W. Brenig, G. Döhler, and H. Heyszenau, Philosophical Magazine **27**, 1093 (1973).

[117] N. Mott, Journal of Non-Crystalline Solids **1**, 1 (1968).

[118] A. L. Éfros and B. I. Shklovskii, Journal of Physics C: Solid State Physics **8**, L49 (1975).

[119] D. Emin, Physical Review Letters **32**, 303 (1974).

[120] P. A. Lee and T. Ramakrishnan, Reviews of Modern Physics **57**, 287 (1985).

[121] K. Muttalib, P. Wölfle, R. Misra, and A. Hebard, Physica B: Condensed Matter **407**, 4023 (2012).

[122] R. Bachelet, F. Sánchez, J. Santiso, C. Munuera, C. Ocal, and J. Fontcuberta, Chemistry of materials **21**, 2494 (2009).

[123] S. Ruddlesden and P. Popper, Acta Crystallographica **10**, 538 (1957).

[124] S. Ruddlesden and P. Popper, Acta Crystallographica **11**, 54 (1958).

[125] A. I. Buzdin, Reviews of modern physics **77**, 935 (2005).

[126] M. Anwar, S. R. Lee, R. Ishiguro, Y. Sugimoto, Y. Tano, S. J. Kang, Y. J. Shin, S. Yonezawa, D. Manske, H. Takayanagi, et al., Nature communications **7**, 1 (2016).

[127] Z. Wang, H. Guo, S. Shao, M. Saghayezhian, J. Li, R. Fittipaldi, A. Vecchione, P. Siwakoti, Y. Zhu, J. Zhang, et al., Proceedings of the National Academy of Sciences **115**, 9485 (2018).

[128] H. Kurata and C. Colliex, Physical Review B **48**, 2102 (1993).

[129] B. Dabrowski, O. Chmaissem, P. Klamut, S. Kolesnik, M. Maxwell, J. Mais, Y. Ito, B. Armstrong, J. Jorgensen, and S. Short, Physical Review B **70**, 014423 (2004).

Vita

Prahald Siwakoti, born in Morang, Nepal, came to the United States in August 2015 to pursue doctorate studies in Louisiana State University following his Masters degree in Science from Tribhuvan University, Nepal. He will begin working as a post-doctoral researcher in the field of experimental condensed matter physics upon completion.